

TIMMU KREITSMANN

Application of carbon isotope and
rare earth elements as recorders of
environmental conditions in
the aftermath of the Paleoproterozoic
Lomagundi-Jatuli Event



TIMMU KREITSMANN

Application of carbon isotope and
rare earth elements as recorders of
environmental conditions in
the aftermath of the Paleoproterozoic
Lomagundi-Jatuli Event



Department of Geology, Institute of Ecology and Earth Sciences, Faculty of Science and Technology, University of Tartu, Estonia.

This dissertation is accepted for the commencement of the degree of Doctor of Philosophy in Geology at the University of Tartu on the 7th of October 2019 by the Scientific Council of the Institute of Ecology and Earth Sciences, University of Tartu.

Supervisors: Kalle Kirsimäe, Department of Geology, University of Tartu, Estonia
Aivo Lepland, Geological Survey of Norway, Norway

Opponent: Prof. Juha Karhu, Department of Geosciences and Geography, University of Helsinki, Finland

This thesis will be defended at the University of Tartu, Estonia, Chemicum, Ravila 14A, room 1019, on the 09.01.2020 at 12:15.

Publication of this thesis is granted by the Institute of Ecology and Earth Sciences, University of Tartu and by the Doctoral School of Earth Sciences and Ecology created under the auspices of the European Social Fund.



European Union
European Social Fund



Investing
in your future

ISSN 1406–2658
ISBN 978-9949-03-223-5 (print)
ISBN 978-9949-03-224-2 (pdf)

Copyright: Timmu Kreitsmann, 2020

University of Tartu Press
www.tyk.ee

CONTENTS

LIST OF ORIGINAL PUBLICATIONS	6
1. INTRODUCTION.....	7
1.1. The stable carbon isotope system	10
1.2. Rare earth elements and Yttrium (REY)	12
2. GEOLOGICAL SETTING	15
3. MATERIAL AND METHODS	17
4. RESULTS	20
4.1. Petrography and mineralogy.....	20
4.2. Carbon, O, and Sr isotope composition	26
4.3. Rare earth elements + yttrium systematics	27
5. DISCUSSION	31
5.1. Secondary alteration in the Upper Zaonega Formation	31
5.2. Preservation of the $\delta^{13}\text{C}_{\text{carb}}$ signal	35
5.3. Screening for the carbonate REY _{SN} signal	37
5.4. Bed scale variation and stratigraphic $\delta^{13}\text{C}_{\text{carb}}$ trends in the Upper Zaonega carbonates	38
5.5. The secular $\delta^{13}\text{C}_{\text{carb}}$ curve of the Zaonega Formation.....	40
5.6. Marine REY _{SN} signal in the Zaonega Formation and the Pilgijärvi Sedimentary Formation	42
5.6.1. Eu _{SN} anomalies in the Zaonega and Pilgijärvi Sedimentary Formations	43
5.6.1. Ce _{SN} anomalies in the Zaonega and Pilgijärvi Sedimentary Formations	44
6. CONCLUSIONS.....	47
REFERENCES.....	49
SUMMARY IN ESTONIAN	62
ACKNOWLEDGEMENTS	65
PUBLICATIONS	67
CURRICULUM VITAE	157
ELULOOKIRJELDUS.....	159

LIST OF ORIGINAL PUBLICATIONS

This thesis is based on the following published papers, which are referred to in the text by Roman numerals. The papers are reprinted with the kind permission of the publishers.

- I **Kreitsmann, T;** Külaviir, M; Lepland, A; Paiste, K; Paiste, P; Prave, A.R; Sepp, H; Romashkin, A.E; Rychanchik, D.V; Kirsimäe, K (2019). Hydrothermal dedolomitisation of carbonate rocks of the Paleoproterozoic Zaonega Formation, NW Russia – Implications for the preservation of primary C isotope signals. *Chemical Geology*, 512, 43–57. 10.1016/j.chemgeo.2019.03.002.
- II Paiste, K.; Lepland, A.; Zerkle, A.L.; Kirsimäe, K.; Izon, G.; Patel, N.K.; McLean, F.; **Kreitsmann, T.**; Mänd, K.; Bui, T.H.; Romashkin, A.E.; Rychanchik, D.V.; Prave, A.R.; (2018). Multiple sulphur isotope records tracking basinal and global processes in the 1.98 Ga Zaonega Formation, NW Russia. *Chemical Geology*, 499, 151–164. 10.1016/j.chemgeo. 2018.09.025.
- III Joosu, L.; Lepland, A.; **Kreitsmann, T.**; Üpraus, K.; Roberts, N.M.W.; Paiste, P.; Martin, A.P.; Kirsimäe, K. (2016). Petrography and the REE-composition of apatite in the Paleoproterozoic Pilgijärvi Sedimentary Formation, Pechenga Greenstone Belt, Russia. *Geochimica et Cosmochimica Acta*, 186, 135–153. 10.1016/j.gca. 2016.04.043.
- IV **Kreitsmann, T;** Lepland, A; Bau, M.; Prave, A.R; Paiste, K; Mänd, K.; Sepp, H; Martma, T.; Romashkin, A.E; Kirsimäe, K. Oxygenated conditions in the aftermath of the Lomagundi-Jatuli Event: the carbon isotope and rare earth element signatures of the Paleoproterozoic Zaonega Formation, Russia. Submitted manuscript.

Author's contribution:

Paper I: The author was responsible for the planning of original research and data collection. He participated in the analysis of mineralogical-geochemical data, the interpretation of analytical results, the synthesis of analytical data and the writing of the manuscript.

Paper II: The author was responsible for the sampling, doing the scanning electron microscope analyses and interpretation. He contributed to the writing of the manuscript.

Paper III: The author was responsible for the planning of research, participated in REE analysis, petrographical and mineralogical characterization and the interpretation of analytical results. He contributed to the writing of the manuscript.

Paper IV: The author was responsible for the planning of original research. He participated in data collection and the interpretation of analytical results. He coordinated and contributed to the writing of the manuscript.

1. INTRODUCTION

The establishment of modern aerobic Earth during the transition from Archean to Proterozoic was accompanied by fundamental changes in the atmosphere-ocean system and the biogeochemical elemental cycles. The global rise of free oxygen started at ca. 2.45 Ga and lasted until 2.06 Ga, a time period called the Great Oxidation Event (GOE; Holland, 2002). However, the first whiffs of oxygenation predating the GOE have been suggested to take place as early as 2.9 Ga (Kato et al., 2002) and 2.5 Ga (Anbar et al., 2007). The rise in oxygen levels is best pinpointed by the loss of MIF (mass-independent fractionation) signal in sulphur isotopes (Bekker et al., 2004; Farquhar et al., 2000; Guo et al., 2009; Luo et al., 2016). In addition, GOE has been inferred from the disappearance of detrital uranite, pyrite and siderite grains (Holland, 2006; Rasmussen and Buick, 1999), the first appearance of red beds (Bekker et al., 2005) and the oxidation state of paleosols (Rye and Holland, 1998).

Interrelated to GOE, Paleoproterozoic also experienced the largest perturbation in the global carbon cycle, called the Lomagundi-Jatuli Event (LJE; Karhu and Holland, 1996; Schidlowski et al., 1976). This was followed by an unprecedented accumulation of organic matter during the Shunga Event (SE; Melezhik et al., 1999; Strauss et al., 2013). Connected to the rise in oxygen levels Earth also experienced global Huronian glaciations (Evans et al., 1997), an expanding seawater sulphate pool (Blättler et al., 2018; Melezhik et al., 2005) and the appearance of first globally significant phosphorites (Lepland et al., 2014; Papineau, 2010; Soares et al., 2019). Most of these global phenomena constitute the most evidently interrelated consequences of the dramatic changes in the atmosphere-ocean chemistry following the GOE (Bekker and Holland, 2012; Holland, 2006; Kasting, 2001; Lyons et al., 2014). However, the relationship between these individual events as well as their causes and consequences are still unclear. During the LJE (2.22 – 2.06 Ga; Karhu and Holland, 1996; Martin et al., 2013a; Melezhik et al., 2007) marine carbonates worldwide were enriched in ^{13}C with $\delta^{13}\text{C}_{\text{carb}}$ values, typically up to 10 – 15‰ (Bekker and Holland, 2012; Karhu and Holland, 1996). The LJE possibly took place in response to the boost in primary productivity and ^{13}C -depleted organic carbon burial, driven by the onset of oxygenic weathering and the increased levels of nutrients in the inflow to the oceans (Holland, 2002).

In several Paleoproterozoic greenschist belts, such as the Onega and Pechenga Basins in Fennoscandia and the Franceville Basin in Gabon, the LJE-bearing carbonate rocks are overlain by rocks highly enriched in organic matter (commonly $\text{TOC} > 10\%$) of the SE (Asael et al., 2013; Kump et al., 2011; Melezhik et al., 1999; Pr at et al., 2011; Strauss et al., 2013). The carbonate units in these successions show the transition from ^{13}C -rich carbonates to isotopically normal carbonates with $\delta^{13}\text{C}_{\text{carb}}$ values near 0‰, denoting the end of the LJE (Melezhik et al., 2015). However, values as low as -25% have been reported in SE age rocks ( rne et al., 2014; Krupenik et al., 2011; Kump et al., 2011; Melezhik et al., 1999,

2015; Pr at et al., 2011), interpreted by some authors as reflecting the global scale oxidation of organic matter, following the LJE (Kump et al., 2011). In addition, based on iron speciation, trace element abundances, sulphur and molybdenum isotopes in these organic-rich sediments it has been suggested that oxygen levels crashed after the LJE and that the atmosphere-ocean system returned to anoxia (Asael et al., 2013, 2018; Bekker and Holland, 2012; Canfield et al., 2013; Partin et al., 2013; Ossa Ossa et al., 2018; Planavsky et al., 2012; Scott et al., 2014). The canonical view of the GOE describes the oxygen levels increasing to ca. 50‰ of the present atmospheric levels (PAL; Pavlov and Kasting, 2002). They dropped to no more than 0.1% PAL at the end of Paleoproterozoic (Planavsky et al., 2014), only to rise again nearly up to modern levels at the end of Neoproterozoic (Lyons et al., 2014; Och and Shields-Zhou, 2012). However, other researchers have pointed out that the high concentration of redox-sensitive elements in post-LJE organic-rich rocks of the Zaonega Formation in the Onega Basin is indicative of prolonged elevated O₂ levels (Sheen et al., 2018, M nd et al., submitted). This is also supported by Large et al. (2019), arguing against the drop in oxygen levels during Mesoproterozoic. In addition, there is growing evidence of variable O₂ concentrations from the end of Paleoproterozoic (Planavsky et al., 2018) and during Mesoproterozoic (Diamond et al., 2018), suggesting a complicated spatiotemporal trend in the oxygen levels during Proterozoic. Moreover, several authors have suggested that the isotope perturbations observed in the post-LJE organic-rich sediments of the Upper Zaonega Formation are due to basin-specific non-global conditions, including diagenetic and hydrothermal overprinting and methanotrophy (Kreitsmann et al., 2019 – PAPER I; Paiste et al., 2018 – PAPER II;  rne et al., 2014; Qu et al., 2012, 2018).

Hence, datasets describing the turbulent post-LJE time period, often derived from the same carbonate and organic-rich rock successions, have arrived at varying to contradictory interpretations of the mechanisms that generated such dramatic perturbations in the carbon cycle.

In general, atmospheric oxygen levels are connected to the global carbon cycle as oxygen release is intimately connected to organic carbon production (oxygenic photosynthesis) and burial. The stable carbon isotope ratios of marine carbonates reflect the balance between buried and residual carbon pools. The changes in the carbon isotope composition of marine carbonates, especially the globally recognized isotopic excursions of $\delta^{13}\text{C}_{\text{carb}}$ values, are interpreted to reflect global changes in the carbon cycle and other related environmental conditions, going back as far as the sedimentary rock record itself (Schidlowski, 2001; Kaufman and Knoll, 1995; Karhu and Holland, 1996; Holland, 2002). The isotopic composition of carbonate sediments, however, constitutes a valuable environmental tracer only if it was recorded in equilibrium with seawater and if the signal has not changed during geological time. It is therefore of utmost importance that the nature of the isotopic values of marine carbonates, original syndepositional and/or altered secondary, is established. Different geochemical characteristics (e.g., $\delta^{18}\text{O}$, $\text{Sr}^{87}/\text{Sr}^{86}$ and Mn/Sr ratio; Banner, 1995; Kaufman and Knoll, 1995) have been used for screening primary carbonates, but a thorough sedimentological and

petrographical framework is crucial while using the geochemical proxies (Hood et al., 2018). Paleoenvironmental conditions and the extent of secondary alteration can also be inferred from the behavior of rare earth elements (including yttrium; REY) in hydrogenous precipitates, such as carbonate and phosphate minerals. Predictable REY distribution patterns make it possible to distinguish between different environmental settings and postdepositional alteration (Bolhar and Van Kranendonk, 2007; Kamber et al., 2014). In addition, redox-sensitive Ce can be used to assess the redox status of the atmosphere-ocean system (Bellefroid et al., 2018; Li et al., 2019).

This thesis focuses on the atmosphere-ocean system after the termination of the LJE. Numerous studies on this much-debated time period have concentrated on the rocks in the Fennoscandian Paleoproterozoic greenschist belts, including the Onega and Pechenga Basins. In particular they discuss the metasedimentary successions of the Zaonega Formation and the underlying Tulomozero Formation in the Onega Basin, which record the transition from the LJE to the SE (Melezhik et al., 2015). Previous studies have fuelled the contradictory discussion on the redox evolution during and after the LJE. The estimations of the redox state in the atmosphere-ocean system have varied from a global contraction of oxygen levels (Asael et al., 2013; 2018; Ossa Ossa et al., 2018; Scott et al., 2014) and the potential fluctuation of basinal redox conditions (Paiste et al., 2018 – PAPER II; Kipp et al., 2017) to the prolonged elevated O₂ levels (Mänd et al., submitted; Sheen et al., 2018).

The overall goal of this thesis is to assess the level of preservation of the paleoenvironmental signatures in the Zaonega Formation in the Onega Basin as well as to evaluate their global and basinal inferences. These signatures will be compared to the Pilgujärvi Formation in the Pechenga Basin by using REY proxies. The specific objectives of the thesis are:

- 1) to study the petrography, mineralogy and the stable carbon isotope signal in the carbonates of the Zaonega Formation and to assess the secondary alteration in these carbonates potentially disturbing the original paleoenvironmental signal;
- 2) to use the best preserved samples of the Zaonega Formation to assess the effects of basin-specific and global marine processes on the recorded paleoenvironmental proxies, and construct the secular carbon isotope curve in the time period immediately following the Lomagundi-Jatuli Event time in the Onega Basin;
- 3) to study the rare earth element signatures in the carbonates of the Zaonega Formation (the Onega Basin) and in the apatite of the Pilgujärvi Sedimentary Formation (the Pechenga Basin), in order to describe the paleoenvironment and oxygen levels in the atmosphere-ocean system in the aftermath of the LJE.

We put forward a central hypothesis that the paleoenvironmental information contained in the sedimentary succession of the Zaonega Formation is influenced by local basinal processes and that most of the sediments have been altered by secondary processes, which would mean that they require careful evaluation before any meaningful environmental interpretation could be offered.

1.1. The stable carbon isotope system

Carbon has two stable isotopes, ^{12}C (98.9%) and ^{13}C (1.1%) (Schidlowski, 2001). The isotopic composition of carbon is expressed as the δ -notation, used to represent the per mil deviation in the $^{13}\text{C}/^{12}\text{C}$ ratio of the sample (sa), in relation to that of a standard (st). In carbonate geochemistry the Vienna Pee Dee Belemnite standard (VPDB) is used and $\delta^{13}\text{C}$ is defined as follows:

$$\delta^{13}\text{C} = \left[\frac{(^{13}\text{C}/^{12}\text{C})_{sa}}{(^{13}\text{C}/^{12}\text{C})_{st}} - 1 \right] \times 1000 \text{ (‰, VPDB)}$$

Carbon isotope composition can naturally vary by more than 120‰ (Hoefs, 2008). Terrestrial carbon isotope fractionation is mainly influenced by two different processes: the equilibrium exchange reactions and the kinetic isotope effects. The former is due to differences in the vibrational energies of different species and the latter is associated with incomplete and unidirectional processes (e.g., diffusion and biologically mediated processes; Hoefs, 2008). The terrestrial carbon pool is split into two parts, a reduced organic carbon pool and an oxidized inorganic carbon pool. Isotope fractionation in inorganic carbon is controlled by the isotope equilibrium exchange reactions between the atmospheric CO_2 – dissolved bicarbonate – solid carbonate (Hoefs, 2008). Dissolved inorganic carbon (DIC) comprises three chemical species: $\text{CO}_2(\text{aq})$, HCO_3^- and CO_3^{2-} . Abundance of species is controlled by the pH, thus ocean water with the average pH of ~ 8.1 consists of $> 90\%$ HCO_3^- (Mackensen and Schmiedl, 2019). Isotope fractionation between species is also dependent on temperature, but carbon isotopes are less temperature sensitive than oxygen isotopes.

In organic matter the $^{13}\text{C}/^{12}\text{C}$ ratio reflects the biological carbon fixation process (i.e., the kinetic isotope effect during carbon fixation), which discriminates against ^{13}C and has the largest carbon isotope effects (Schidlowski, 2001). While most terrestrial organic matter has $\delta^{13}\text{C}_{\text{org}}$ values of about $-26 \pm 7\%$ (Schidlowski et al., 1983), methanotrophic archaea can produce organic matter with $\delta^{13}\text{C}_{\text{org}}$ values as low as -80% (Freeman et al., 1990).

In the global carbon cycle balance exists between the organic carbon pool with low $\delta^{13}\text{C}$ values and the inorganic carbon pool with higher $\delta^{13}\text{C}$ values. The combined isotopic composition of these two pools must be equal with the initial input of carbon (i.e., weathering products with average mantle $\delta^{13}\text{C}$ values around -5%). Hence, if more organic carbon is buried, the isotopic composition of the remaining inorganic carbon becomes increasingly heavier, and *vice versa*. The

burial rate of organic carbon is important, because it is connected to the oxygen released and kept in the atmosphere (i.e., one mole of buried organic carbon allows a mole of oxygen to be kept in the atmosphere). Long-term secular variations in the global carbon cycle are related to tectonic activity and the changes in primary productivity. Thus, establishing global carbon excursions in marine carbonates through geological time also provides us with information about the changes in atmospheric oxygen levels.

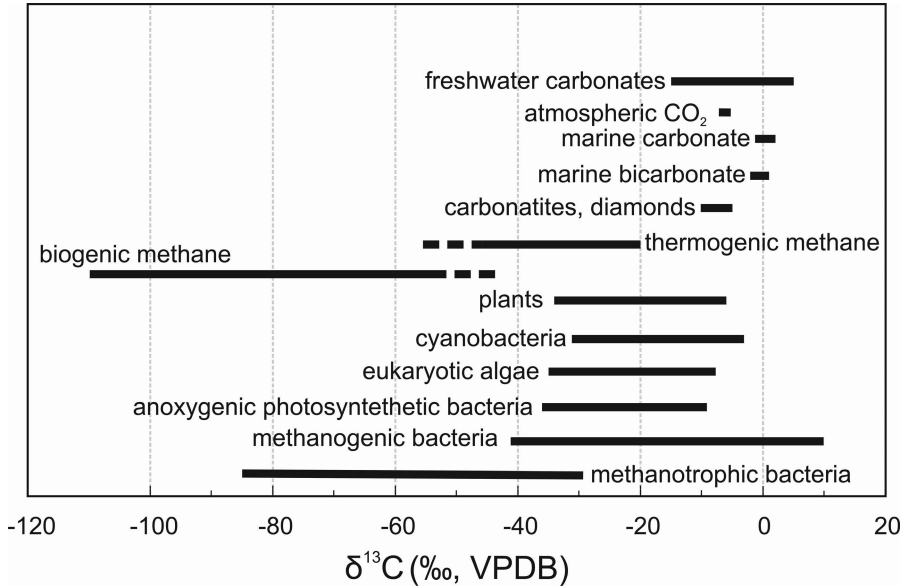


Figure 1. The $\delta^{13}\text{C}$ values of different organisms and inorganic carbon species (modified after Hoefs, 2008; Shidlowski, 2001, Whiticar, 1999).

The $\delta^{13}\text{C}$ values of carbonates are controlled by the $\delta^{13}\text{C}$ of ambient DIC, mineralogy, temperature, pH and the rate of precipitation (Swart, 2015). In marine settings carbonates are precipitating near equilibrium with DIC. In general, the $\delta^{13}\text{C}$ values of DIC are relatively stable around 0‰ in the surface ocean waters – that is ~6 to 7‰ heavier than the $\delta^{13}\text{C}$ of atmospheric CO_2 (modern $\delta^{13}\text{C}_{\text{atm}} \sim -8.3\text{‰}$ and preindustrial $\delta^{13}\text{C}_{\text{atm}} \sim -6.5\text{‰}$; Sharp, 2007; Swart, 2015). The DIC in near-surface waters is enriched by 1 to 2‰ in ^{13}C compared to deep waters, due to the biological pump (Sharp, 2007). Carbon isotopes are relatively insensitive to temperature, the minor effect decreasing even further with increasing temperature. pH controls the carbon isotope ratio due to pH dependence on isotope fractionation between carbon species. At a lower pH, carbonates have higher $\delta^{13}\text{C}$ values than carbonates which formed in higher pH environments. However, above the pH value of 10 the $\delta^{13}\text{C}$ value of carbon species stops varying (Swart, 2015). Carbonate mineralogy also plays a role in C isotope fractionation. For instance, the $\delta^{13}\text{C}$ of dolomite can be ~1‰ heavier than that of the co-occurring low-Mg calcite, while the $\delta^{13}\text{C}$ of aragonite can be 1–2‰ heavier than

that of high- and low-Mg calcite (Romanek et al., 1992; Swart, 2015). In biogenic carbonates vital effect plays an important role as well, i.e., various organisms fractionate carbon isotopes to different extent. The shells of some Ca-carbonate secreting organisms have been shown to have 14‰ lower $\delta^{13}\text{C}$ values than what is predicted from equilibrium (Sharp, 2007).

Carbonates in different environments also have a distinct bulk carbon isotopic signal, depending on how or where the carbonate minerals form (Fig. 1). Marine carbonates have an average $\delta^{13}\text{C}$ and $\delta^{18}\text{O}$ value of almost zero, which can decrease due to the vital effects and diagenesis. Authigenic sediments of carbonate platforms dominated by non-skeletal grains have higher $\delta^{13}\text{C}$ values, compared to deep-water environments dominated by skeletal grains (Swart, 2015). Fresh-water carbonates commonly have more negative $\delta^{13}\text{C}$ values due to the relative abundance of organic matter and its effects on the DIC pool in meteoric waters. During diagenesis $\delta^{13}\text{C}$ values usually decrease, but the effect is not as prominent as on $\delta^{18}\text{O}$ values. In anaerobic sediments where Mn^{4+} , NO_3^- and Fe^{3+} have been consumed, sulphate is used for oxidizing organic matter. The HCO_3^- which is produced from oxidized organic matter during the sulphate reduction does not experience significant fractionation in carbon isotopes and its $\delta^{13}\text{C}$ values are similar to those of source organic matter (Whiticar, 1999). Methanogens start to produce methane *via* CO_2 reduction and acetate fermentation when most of the sulphate has been consumed in the diagenetic realm. During the methanogenesis ^{12}C is preferentially used for producing CH_4 , leaving the residual carbon pool enriched in ^{13}C and triggering the precipitation of diagenetic carbonates with higher $\delta^{13}\text{C}$ values than those of unaltered carbonates. In a closed-system $\delta^{13}\text{C}$ values up to +34‰ have been measured in ^{13}C -enriched carbonates (Budai et al., 2002). Methane, however, diffuses upwards and it can be anaerobically oxidized by a consortia of methanotrophic archaea and sulphate reducing bacteria in a process termed as anaerobic oxidation of methane (AOM). The AOM increases the alkalinity and the precipitating-methane-derived carbonates can have $\delta^{13}\text{C}$ values as low as $\sim -75\text{‰}$ (Campbell, 2006). The influence of diagenetic carbonates produced through the oxidation of organic matter and/or the methanogenesis on the bulk rock depends on their relative contribution. In carbonate-rich systems, the signal from diagenetic phases is effectively masked by the dominating signal from the parent carbonate sediment. However, in carbonate-poor sediments, diagenetic phases can make significant contribution to the entire carbonate pool, both decreasing and increasing the $\delta^{13}\text{C}$ value of the bulk carbonate (Swart, 2015).

1.2. Rare earth elements and Yttrium (REY)

Rare earth elements are a coherent series of elements from La to Lu that also include Y, the geochemical twin of Ho. The behavior of rare Earth Elements and Y (hereafter referred to as REY) is strongly influenced by the lanthanide contraction (i.e., their ionic radii decrease more than expected with an increasing

atomic number), causing a different complexation and adsorption activity in light rare earth elements (LREE – from La to Nd), when compared to middle (MREE – from Sm to Dy) and heavy rare earth elements (HREE – from Ho to Lu; Elderfield et al., 1988). The oxidation state of REY is typically +3, however, in oxic conditions Ce^{3+} can be oxidized to Ce^{4+} (Bau and Koschinsky, 2009) and Eu^{3+} is reduced to Eu^{2+} in high-temperature hydrothermal fluids ($>250\text{ }^{\circ}C$) (Bau, 1991; Douville et al., 1999) causing anomalous behavior of Ce and Eu. Small and predictable differences in their physicochemical properties make REY a powerful tool for studying the modern and ancient atmosphere-ocean systems as well as the paleoenvironments of hydrogenous sediments (e.g., banded iron formations, carbonates, phosphates). In the studies of sedimentary carbonates, the measured REY concentrations are commonly normalized against a known standard (e.g., North American shale composite, NASC or Post-Archean Australian shale, PAAS; Gromet et al., 1984; Taylor and McLennan, 1985, respectively). This enables to remove the natural variance in absolute concentrations (i.e., Oddo-Harkins effect) and to assess the partitioning of elements compared to REY sources. REY substitute Ca^{2+} and/or Mg^{2+} in the crystal lattice of carbonate minerals due to similar ionic radii. To a lesser extent REY can also occupy structural defects, be adsorbed on the crystal surface due to their ionic charge and be part of fluid inclusions (Bau and Möller, 1992; Kučera et al., 2009; Zhong and Mucci, 1995). The incorporation of REY into carbonate mineral crystal lattice makes the primary REY pattern relatively resistant to secondary alteration and even dolomitization (Banner et al., 1988; Bau and Alexander, 2006).

REY systematics have been used to discriminate between open marine, restricted and lacustrine settings, to study the influence of hydrothermal fluids and in rare cases even relative to water depth (Alexander et al., 2008; Allwood et al., 2010; Bau and Alexander, 2006; Frimmel, 2009; Kamber et al., 2014; Kamber and Webb, 2001; Webb and Kamber, 2000). REY speciation in aqueous environments is influenced by a stronger complexation between the dissolved ligands (e.g., $[CO_3^{2-}]$) and HREE, the preferential adsorption of LREE on the settling particles and the distinct electron configuration of 4f electron shell through the lanthanide series (Bau and Dulski, 1999; Elderfield, 1988). The abundance of REY and their pattern in seawater reflects the relative input of different REY sources (hydrothermal and continental) and the following particle-solution reactions (Bolhar et al., 2004).

Modern oxic seawater (Fig. 2) is characterized with: (a) LREE depletion compared to HREE (Elderfield, 1988), (b) the positive PAAS-normalized La, Gd and Lu anomaly (Bau and Dulski, 1999; Bolhar et al., 2004; Tostevin et al., 2016), (c) super-chondritic Y/Ho ratios (>44 ; Bau et al., 1996; Nozaki et al., 1997), (d) the variable but mostly negative PAAS-normalized Ce anomaly (Elderfield, 1988). REY concentrations are depleted in surface waters and become increasingly more enriched in deep waters, similarly to nutrients' behavior in water column (Elderfield et al., 1988). In the oxic water column the concentration of redox-sensitive Ce decreases with depth, due to the oxidative removal. However, in a stratified basin Ce concentration increases just below the redoxcline and reaches

unity with increasing depth (de Baar et al., 1988). A typical PAAS-normalized REY (REY_{SN}) pattern in seawater develops in river deltas and estuaries where riverine REY load is removed by the colloidal particles and the salinity-induced coagulation (Sholkovitz et al., 1994), followed by the adsorptive scavenging in the ocean water column (De Baar et al., 1985). A similar REY_{SN} pattern has also been described in terrestrial waters (Johannesson et al., 2006), although the features there are usually not as pronounced. River waters are characterized by a relatively flat, shale-like REY_{SN} pattern (Fig. 2; Lawrence et al., 2006). The REY_{SN} pattern of hydrothermal fluids can slightly vary, depending on the temperature of the fluid, but generally they are enriched in LREE compared to MREE and HREE as well as showing a distinct positive Eu_{SN} anomaly (Fig. 2; Bau and Dulski, 1999; Douville et al., 1999).

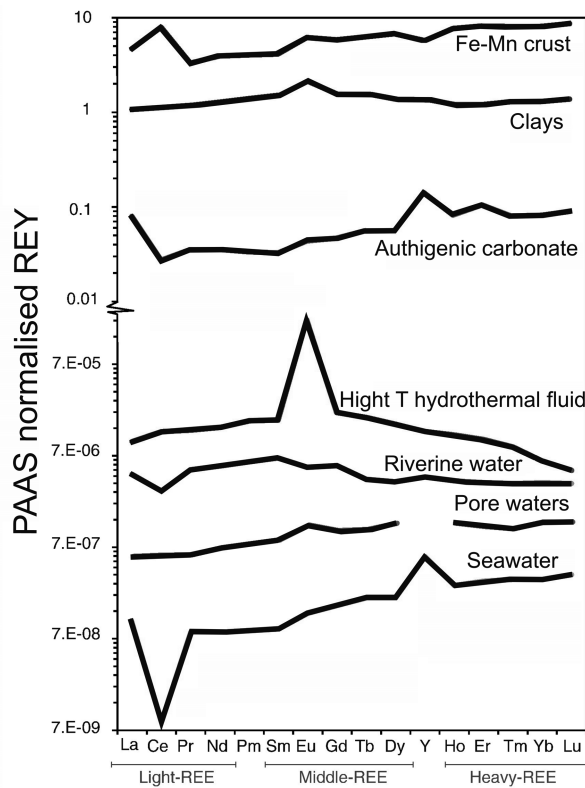


Figure 2. The PAAS-normalized REY pattern in various natural environments and minerals (taken from Tostevin et al., 2016).

2. GEOLOGICAL SETTING

The Zaonega Formation in the Onega Basin is located in Northwestern Russia and it is part of the Archean Karelian craton (Fig. 3). The Onega Basin formed in a rift basin, representing a volcanic-sedimentary succession with several episodes of erosion and non-depositional breaks covering the time span between c. 2440–1890 Ma (Melezhik et al., 2015). The Zaonega Formation is lying on the dolostones of the Tulomozero Formation, which were deposited in a restricted marine embayment, recording the LJE positive $\delta^{13}\text{C}_{\text{carb}}$ excursion (Blättler et al., 2018; Brasier et al., 2011; Karhu, 1993). The Zaonega Formation is overlain by the mafic and ultramafic lavas of the Suisari Formation, which is covered by greywackes and siltstones of the Kondopoga Formation, deposited from turbidity currents in a nearshore lacustrine setting (Melezhik et al., 2013). During the Svecofennian orogeny (1890–1790 Ma) the whole succession experienced greenschist facies metamorphism (Melezhik et al., 1999).

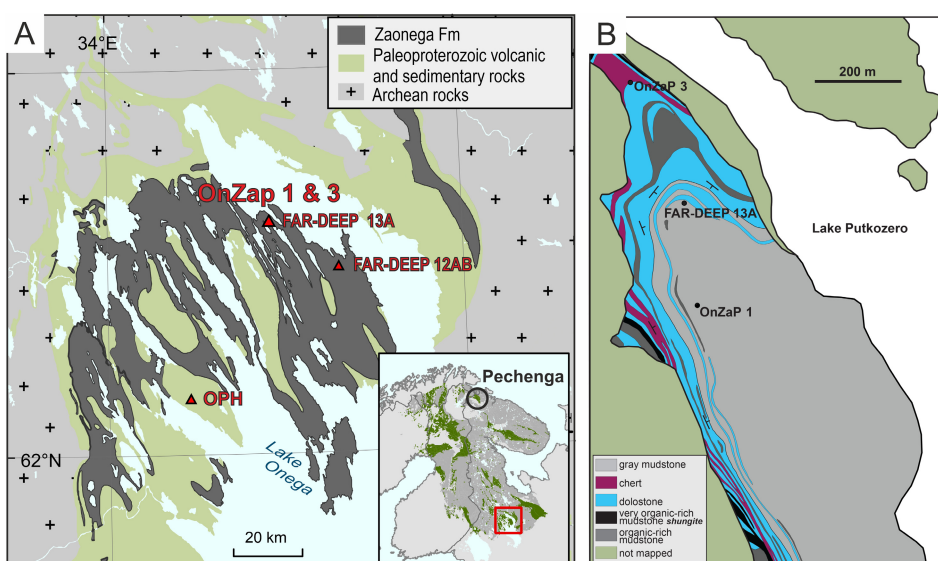


Figure 3. (A) A simplified geological map of the Onega Basin (modified after Koistinen et al., 2001) with the drill hole locations. (B) A higher resolution geological map on the Upper Zaonega Formation showing the locations of OnZap 1 and 3 and FAR-DEEP 13A drill holes (after Melezhik et al. 2013).

The age constraints for the Zaonega Formation are poorly established. A positive $\delta^{13}\text{C}_{\text{carb}}$ excursion extends to the lowermost part of the Zaonega Formation (Melezhik et al., 2015). The LJE terminated in the Fennoscandia at 2.06 Ga (Karhu and Holland, 1996; Martin et al., 2013a; Melezhik et al., 2007), giving us the maximum age. In the Upper Zaonega Formation the best preserved carbonate $\delta^{13}\text{C}$ values are at c. 0‰ (Kreitsmann et al., 2019 – PAPER I; Kreitsmann et al., submitted – PAPER IV; Črne et al., 2014), suggesting that the Upper Zaonega Formation post-dates the LJE. The lower age limit comes from an overlying

gabbro sill from the Suisari Formation, yielding an age of 1988 ± 34 Ma (Puchtel et al., 1999). Dykes intersecting the Zaonega Formation yield the ages of 1919 ± 18 Ma (Priyatkina et al., 2014), 1956 ± 5 Ma (Stepanova et al., 2014) and 1961.6 ± 5.1 Ma (Martin et al., 2015). The most recent age was established by Martin et al. (2015), who dated tuffs in the Lower Zaonega Formation defining a depositional age of 1982 ± 4.5 Ma. The present thesis adopts the conservative estimate of 1980 Ma.

The Zaonega Formation was deposited in a rift-bound basin dominated by turbidity currents and background hemipelagic sedimentation, which shallowed into a lagoonal environment towards the upper part of the Formation (Melezhik et al., 1999, 2015). The lower part of the Formation comprises rhythmically interbedded fine-grained greywackes and mudstones (interpreted as turbidites; Črne et al., 2013), whereas the upper part of the Formation is composed of organic-rich mudstones, siltstones, calcareous mudstones and dolostones intersected by mafic lavas and sills (Črne et al., 2014). Magmatic activity, as evidenced by peperites, was contemporaneous with the sedimentation, and triggered also secondary silicification and generation and migration of hydrocarbons (Črne et al., 2014; Qu et al., 2012). The Zaonega Formation contains extremely organic-rich rocks (shungites) with an average organic content of c. 25%, reaching 98% in pyrobitumen veins (Melezhik et al., 1999). The $\delta^{13}\text{C}_{\text{org}}$ data define a profile in which values of c. -25‰ sandwich the excursion to as low as c. -40‰ in the middle and upper part of the Formation (Kreitsmann et al., 2019 – PAPER I; Paiste et al., 2018 – PAPER II; Melezhik et al., 1999; Qu et al., 2012). Whether this accumulation of organic matter and the associated $\delta^{13}\text{C}_{\text{org}}$ excursion was synchronous and global (Kump et al., 2011; Ossa Ossa et al., 2018; Scott et al., 2014), or a consequence of temporally discrete basin-specific depositional episodes (Paiste et al., 2018 – PAPER II; Kreitsmann et al., PAPER – IV; Lepland et al., 2014; Martin et al., 2015; Qu et al., 2018, 2012), remains subject to debate.

In order to place the Zaonega Formation into a broader context, the Zaonega REY_{SN} results are compared with the REY_{SN} data from the slightly younger Pilgijärvi Sedimentary Formation (SF) in the Pechenga Basin (Fig. 3). The Pilgijärvi SF is part of the Pechenga Greenstone Belt, which underwent regional greenschist facies metamorphism during the Svecofennian Orogeny (Melezhik and Hanski, 2013). The Pilgijärvi SF is lying on the Kolosjoki Sedimentary and Volcanic Formations, the former carrying the post-LJE normal marine carbonate $\delta^{13}\text{C}$ signal (Salminen et al., 2013). The Pilgijärvi SF is dominated by rhythmically interbedded C_{org}-rich and sulphide-rich turbiditic greywackes as well as shales and tuffs deposited in the continental slope environment (Melezhik and Hanski, 2013). Phosphorus-rich intervals occur as lenses, i.e., a series of gritstone and coarse-grained sandstone beds within a 50–250 m thick succession. Phosphates that have been analyzed for their REY_{SN} typically occur as clasts in the most coarse-grained part of the sequence (Joosu et al., 2016 – PAPER III), but also as cementing the rhythmically bedded fine-grained sediments (Kreitsmann et al., 2016). The age of the Pilgijärvi SF is constrained between 1.98 and 1.92 Ga (Hanski et al., 2014; Martin et al., 2013b).

3. MATERIAL AND METHODS

The material analyzed in this thesis is taken from the intervals representing the Upper Zaonega Formation in the Onega Parametric Hole (OPH; 62.5870 N, 34.9310 E), the OnZap1 (62.5870 N, 34.9310 E) and OnZap3 (62.5920 N, 34.9280 E) drill cores in the Onega Basin. The two OnZap drill cores form a 102 m long composite OnZap section. The OPH and OnZap cores are correlated with a prominent basinwide massive dolostone horizon associated with very organic-rich mudstone with the highest concentration of phosphorus and trace elements in the entire Zaonega Formation (Paiste et al., 2018 – PAPER II). This marker lithological contact is at 1112 m in the OPH, at 10.8 m in OnZap1 and at 53 m in OnZap3. The internal parts of carbonate beds were sampled at 10 cm spacings. Sampling density increased to 2–5 cm when approaching the bed contacts with the enclosing siliciclastic strata and cross-cutting silica veins. Thin sections and polished slabs were obtained for petrographical characterization. The phosphorite samples of the Pilgijärvi Formation in the Pechenga Basin were collected from the excavated material in an open-pit mine (69.2435 N, 30.3815 E) as well as from rhythmically bedded mudstones and sandstones outcropping on the quarry wall (69.2437 N, 30.4197 E).

The thin sections and polished slabs of selected samples were analyzed by a ZEISS EVO MA15 scanning electron microscope (SEM). Chemical characterization (point analyses and elemental mapping) was carried out with an Oxford AZTEC-MAX energy dispersive spectroscopy detector (EDS) attached to the SEM at the University of Tartu.

A total of 113 samples were taken from the OPH core and 500 samples were obtained from the OnZap section. The samples were analyzed for the stable isotope ratios of O and C by using a Thermo Scientific Delta V Advantage continuous flow isotope ratio mass spectrometer and GasBench II preparation line connected to a Delta V Advantage IRMS (Thermo Fisher Scientific) at the University of Tartu and the Tallinn University of Technology. The long-term reproducibility was better than $\pm 0.2\%$ (2σ) for $\delta^{18}\text{O}$ and $\delta^{13}\text{C}$. The results of carbonate mineral analyses are given in per mil deviation relative to Vienna PeeDee Belemnite (VPDB) for oxygen and carbon. The $\delta^{18}\text{O}$ values were corrected for phosphoric acid fractionation factor for calcite and dolomite (Rosenbaum and Sheppard, 1986), in accordance with sample mineralogy.

Splits of microdrilled samples were used for studying the mineralogical composition by means of X-ray diffractometry (XRD) at the University of Tartu. Unoriented preparations were scanned on a Bruker D8 Advance diffractometer using Cu $K\alpha$ radiation and a LynxEye positive sensitive detector in 2–70° 2 θ range. Quantitative mineralogical composition was modelled by using the Rietveld algorithm-based software Topaz. The relative error of quantification is better than 10% for major phases (>5 wt.%) and better than 20% for minor phases (<5 wt.%).

Six OPH samples with their calcite and dolomite contents varying between 1.2–69 wt.% and 0.4–93.6 wt.%, respectively, were selected for the sequential dissolution experiments to assess the isotopic composition of calcite and dolomite end-members (*sensu* Al-Aasm et al., 1990). The sequential dissolution protocol of Al-Aasm et al. (1990) used a reaction time of 2 hours at 25 °C in 99% phosphoric acid for calcite and 4 hours for dolomite at 50°C. However, our XRD analysis on residues showed that if the reaction time in the first step was longer than 30 minutes, a significant amount of dolomite (> 10%) was dissolved along with the complete removal of calcite. Reducing the reaction time to c. 20 minutes at 25 °C resulted in the complete removal of calcite and only minor dissolution of dolomite (< 10%). Hence, we adopted the shorter reaction time for the first step. After the CO₂ from the first step was retracted, the reaction vials were purged with He and the samples were left to react overnight (8 hours) at 70 °C. Isotope values obtained from the first and second steps were assigned to calcite and dolomite, respectively.

In the 51 OPH samples, the carbon isotope composition of bulk organic carbon was measured. Samples were left to react overnight with 10% HCl to remove carbonate phases. The retained material was rinsed multiple times with deionized water, dried and weighed for analysis with a Delta V Plus mass-spectrometer with Flash HT Plus interface. The C_{org} isotope composition is reported in per mil relative to VPDB.

Nineteen OPH samples with varying dolomite and calcite mineralogy were chosen for the strontium isotope and trace element analyses. The homogenized samples were leached in ultrapure 1M HCl for 1 hour at room temperature. Trace element concentrations were determined by using Agilent 8800 ICP-MS/MS with indium as the internal standard and NIST 1643f as the quality control standard. The Sr-isotope composition was measured on an Agilent 8800 ICP-MS/MS in double mass selection (MS/MS) mode using 10% of SF₆ in 90% He as the reaction gas in the Collision Reaction Cell at the University of Tartu. Signals were collected using 5 replicate measurements with 100 sweeps per replicate and 100 ms dwell times for ^{86,87,88}SrF⁺. The use of SF₆ reaction gas removes the spectral overlap from Rb as the latter does not react with the gas (Cheng et al., 2008; Hogmalm et al., 2017). The Sr isotopic ratios were then measured at mass-to-charge ratios corresponding to SrF⁺ ions, enabling accurate determination of the ⁸⁷Sr/⁸⁶Sr isotope ratio without prior Rb/Sr separation (Bolea-Fernandez et al., 2015). External correction was applied by using NIST SRM 987 in a sample-standard bracketing protocol. USGS MACS-3, which had been digested alongside the samples, was used as a quality control standard for ⁸⁷Sr/⁸⁶Sr ratio measurements (average ⁸⁷Sr/⁸⁶Sr 0.7077 ± 0.0006). Initial ⁸⁷Sr/⁸⁶Sr values were calculated and corrected for Rb by means of an equation by Banner (1995) with the decay constant $\lambda_{87} = 1.3972 \pm 0.0045 \cdot 10^{-11} \text{ a}^{-1}$ (Villa et al., 2015), given the geological age of 1.98 Ga. The corrected ⁸⁷Sr/⁸⁶Sr ratios were 0.01%–1.31% lower than the measured values.

Twenty-nine of the micro-drilled OnZap samples were chosen for the major and trace element analyses at Jacobs University Bremen. The samples were

selected to span the entire OnZap section and different carbonate mineralogy. For the analyses, 0.1 g of the sample was measured and left to dry overnight at 105 °C. The dried samples were dissolved at a high pressure and temperature (165 °C) in an acid mixture of suprapure concentrated 3 ml HCl, 1 ml HNO₃ and 1 ml HF for 16 hours, by using a Picotracer digestion system. The acid-sample-mixture was then evaporated twice by adding 5 ml suprapure concentrated HCl, followed by redissolving in 0.5 M HNO₃. Major elements were measured with inductively coupled plasma optical emission spectrometry (ICP-OES) and trace elements with inductively coupled plasma mass spectrometry (ICP-MS). A dolomite standard reference material JDo-1 was used to monitor analytical precision.

Rare earth elements in apatite were measured at the University of Tartu by using laser ablation inductively coupled plasma mass spectrometry (LA-ICP-MS). Ablation parameters were set at 40 µm spot size at 5 Hz and ~2.5 j/cm² fluence with a 40 s dwell time. Helium mixed with argon from a desolvating nebulizer was used as a carrier gas. The measured elements were normalized to ⁴⁴Ca assuming 39.7% Ca in the apatite mineral. NIST612 was used as a standard and the reproducibility within each analytical session was better than 10% for each mass measured. The REY concentrations were normalized against Post Archean Australian Shale (PAAS; Taylor and McLennan, 1985; except Dy from McLennan, 1989). The subscript “SN” denotes the shale normalized values. Elemental anomalies were calculated with a linear method, after Bau and Dulski, (1996; Eq. 3, 4, 5) and Bolhar et al., (2004; Eq. 1, 2) and the bell-shape index (BSI), after Tostevin et al., (2016; Eq. 6), by using the following equations:

$$(La/La^*)_{SN} = \frac{La_{SN}}{(3Pr_{SN} - 2Nd_{SN})} \quad (\text{Eq. 1})$$

$$(Gd/Gd^*)_{SN} = \frac{Gd_{SN}}{(2Tb_{SN} + Dy_{SN})} \quad (\text{Eq. 2})$$

$$(Ce/Ce^*)_{SN} = \frac{Ce_{SN}}{(0.5La_{SN} + 0.5Pr_{SN})} \quad (\text{Eq. 3})$$

$$(Eu/Eu^*)_{SN} = \frac{Eu_{SN}}{(0.67Sm_{SN} + 0.33Tb_{SN})} \quad (\text{Eq. 4})$$

$$(Pr/Pr^*)_{SN} = \frac{Pr_{SN}}{(0.5Ce_{SN} + 0.5Nd_{SN})} \quad (\text{Eq. 5})$$

$$BSI = \frac{2*(Sm_{SN} + Gd_{SN} + Dy_{SN})/3}{(La_{SN} + Pr_{SN} + Nd_{SN})/3 + (Ho_{SN} + Er_{SN} + Tm_{SN} + Yb_{SN} + Lu_{SN})/5} \quad (\text{Eq. 6})$$

The Eu_{SN} anomaly in the Pilgūjärvi samples was calculated by using Gd instead of Tb. Tm was interpolated from Er and Yb for BSI calculation.

4. RESULTS

Most of the results of this thesis are derived from the Upper Zaonega Formation. The studied OPH section focusses on the basin-wide prominent dolomite horizon, whereas the OnZap section covers the dolomite horizon, but also an additional ~40 m above and ~50 m below the dolomite horizon. Four carbonate beds in the OPH section were named A, B, C, and D, starting from top to bottom (Fig. 4, Kreitsmann et al., 2019 – PAPER I). Based on the lithological and geochemical characteristics Paiste et al. (2018 – PAPER II) divided the OnZap section into three units. The lowermost unit (Unit A) at a depth of 102–53 m is composed of rhythmic black organic-rich mudstones as well as calcareous mudstones and dolostones (corresponding to the carbonate beds C and D from the OPH section). Unit B at a depth of 53–33 m consists of dolostone beds, interlayered with organic-rich mudstones, corresponding to the carbonate beds A and B in the OPH section. Unit C at a depth of 33–1.7 m is characterized by grey organic-poor mudstones and marly carbonate beds (Paiste et al., 2018 – PAPER II; Kreitsmann et al., submitted – PAPER IV). The OnZap section contains 11 carbonate bed intervals with distinct geochemical patterns, carbonate mineralogy and petrography (Table 1 in Kreitsmann et al., submitted – PAPER IV; Fig. 6).

4.1. Petrography and mineralogy

In this thesis focus is on the carbonate beds from the OPH and OnZap drill cores. The mineral composition of the carbonate rocks from the OPH core (Supplementary table 1 in Kreitsmann et al., 2019 – PAPER I) is dominated by dolomite and calcite, varying from < 0.5 wt.% (hereafter noted as trace amounts) to 93.6 wt.% of crystalline phases and from 1.1 to 83.0 wt.%, respectively. Calcite is the dominant carbonate phase on the margins of the beds, whereas dolomite content is the highest in the interiors. A clear negative covariance exists between dolomite and calcite (Fig. 4). In addition, the margins of carbonate beds have a higher concentration of quartz, mica and talc. Their pyrite concentration varies from trace amounts in the upper part to 10.8% in the lower part of the OPH section. Additional mineralogical and petrographical information of mudstones inter-layering the carbonate beds are given in Paiste et al. (2018 – Paper II).

The dolomite in the OPH samples exhibits planar-e (euhedral) (Fig. 5A and B) or intergrown planar-s (subhedral) rhombohedral crystals, mostly less than 150 µm in diameter. Intra-crystalline calcite is common in dolomite crystals and it can vary from a few µm in size (Fig. 5A) to much larger (> 100 µm) patches of either equicrystalline anhedral calcite filling the pore space between dolomite rhombohedral crystals (Fig. 5B and C) or as a pseudomorphic replacement of dolomite (Fig. 5D). The pore space between dolomite crystals is mostly filled by anhedral calcite and talc near the bed margins (Fig. 5C), and organic matter (Fig. 5A and B) and mica in the interiors.

In the OnZap section the carbonate mineralogy (Supplementary table 1 in Kreitsmann et al., submitted – PAPER IV) is more heterogeneous than in the OPH section. Unit A contains 5 carbonate intervals (Fig. 6). A5 is mostly dolomitic (up to 89.5 wt.%), A2 and A3 are calcitic (up to 75.7 wt.%). A1 and A4 have mixed carbonate mineralogy. Most of the dolomite is characterized by uniformly fine-grained dolomite aggregates (10–20 μm in size) of planar-s crystals with minor Fe (Fig. 7B and D). The dolospar in A5 is an exception as it has larger, 200–300 μm planar-s to nonplanar locally-zoned dolomite crystals, which have experienced dedolomitization. Calcite occurs in three forms: (I) fine-grained (< 100 μm in diameter) euhedral calcite crystals (Fig. 7A), (II) macroscopically visible large poikilitic calcite crystal aggregates with many inclusions of host-rock minerals, (III) large masses of anhedral calcite replacing dolomite (Fig. 3 in Kreitsmann et al., submitted – PAPER IV). Calcareous mudstones of Unit A contain a significant amount of siliciclastic material in carbonate cement, such as micas, quartz, feldspar and talc.

There are 3 carbonate intervals in Unit B. B1 is marked by massive dolospar beds interlayered with organic-rich mudstones and it is associated with secondary hydrothermal silicification. The internal parts of beds consist of relatively pure dolomite (up to 94.8 wt.%), but towards the bed margins the calcite content increases up to 83.5 wt.% (Fig. 6). B2 is made up of calcareous mudstone with calcite occurring in three forms: small subhedral crystals (20–40 μm) with mica rims and sometimes with quartz grain cores; large calcite crystals (>1 mm) as early-formed aggregates (laminae are compacted around the aggregates); or calcite aggregates cross-cutting laminae and containing mica. Interestingly, some of the calcite is well-rounded, suggesting that it was reworked and transported as a sedimentary particle. Dolomite textures in B1 and B2 vary from planar-e and planar-s (Fig. 7C) to nonplanar crystals, which, in rare cases, include void-filling dolomite crystals (Fig. 7D). Dolomite crystals are between 200–400 μm in size, zoning is rare and their Fe content does not vary as much as in the other units (Supplementary table 2 in Kreitsmann et al., submitted – PAPER IV). The calcite in B1 and B3 intervals forms large anhedral aggregates which replace and/or surround dolomite.

Three carbonate intervals occur in Unit C (C1–C3). They contain abundant Fe-rich ankerite-dolomite solid-solution minerals (Fig. 6 in Kreitsmann et al., submitted – PAPER IV). Calcite is rare and its content does not exceed 12 wt.%. The dolomite-ankerite series is characterized by planar-e to planar-s zoned rhombohedral crystals (Fig. 7E). Dolomite crystals are smaller than those in the other units, varying between 20–40 μm . The C1 interval has secondary Fe-rich dolomite aggregates, which are rare in C2 and C3. The carbonate cement in Unit C is a Fe-rich dolomite, whereas it is mostly calcite in the other units. The concentration of iron in carbonates increases from the bottom part of Unit C towards the top. According to the XRD and SEM studies, siderite can be found in the C3 interval, where its concentration reaches 7.6 wt.% (Supplementary table 1 in Kreitsmann et al., submitted – PAPER IV). Siderite forms large, ~0.5 mm sized anhedral aggregates, often surrounded by pyrite. The texture of siderite

appears to indicate that it was formed later than the surrounding quartz and mica as there are inclusions in the poikilitic siderite aggregates which have gone through partial dissolution. In addition, rhombic marks in the siderite aggregates, probably caused by dolomite dissolution, are also common (Fig. 7F).

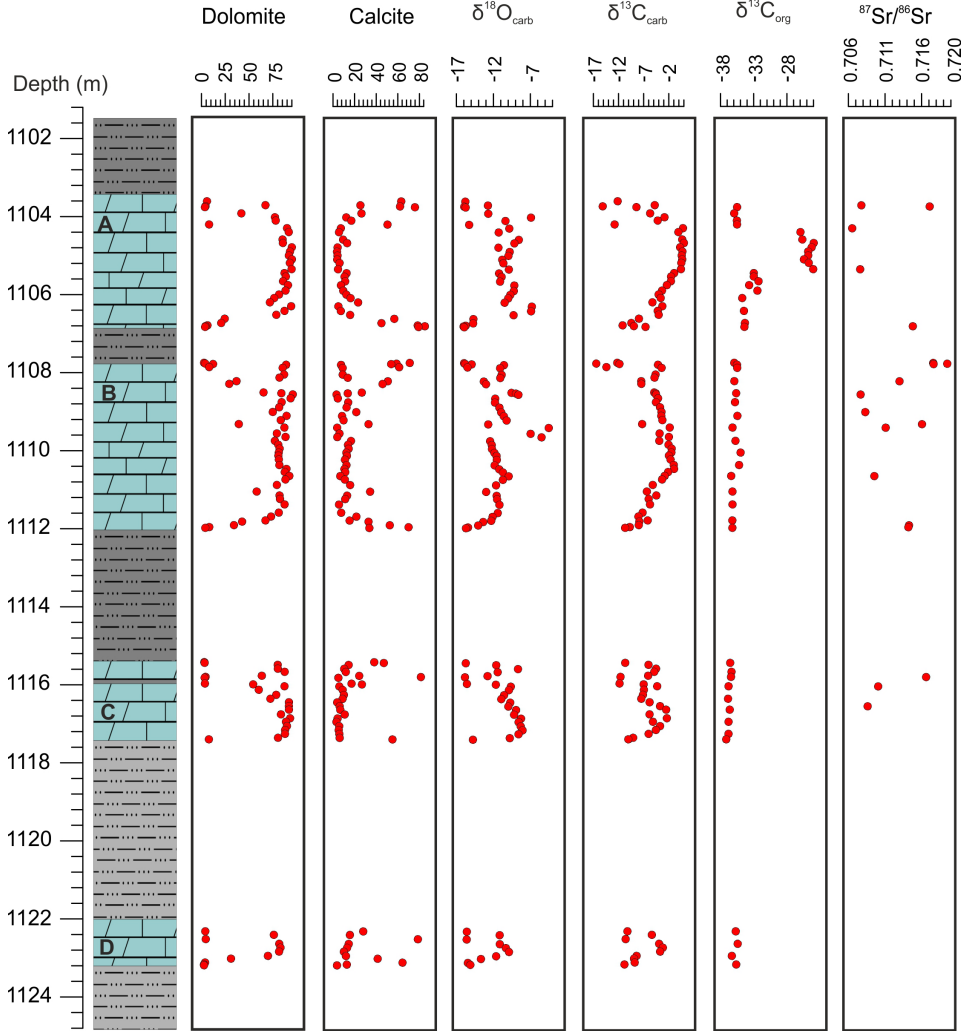


Figure 4. Dolomite and calcite abundance (wt.%) along with $\delta^{13}\text{C}_{\text{carb}}$, $\delta^{18}\text{O}_{\text{carb}}$, $\delta^{13}\text{C}_{\text{org}}$ (‰, VPDB), and $^{87}\text{Sr}/^{86}\text{Sr}$ ratio values in the OPH section (Kreitsmann et al., 2019 – PAPER I). Blue marks dolostone, dark grey marks very organic-rich mudstone and light-grey marks organic-rich mudstone.

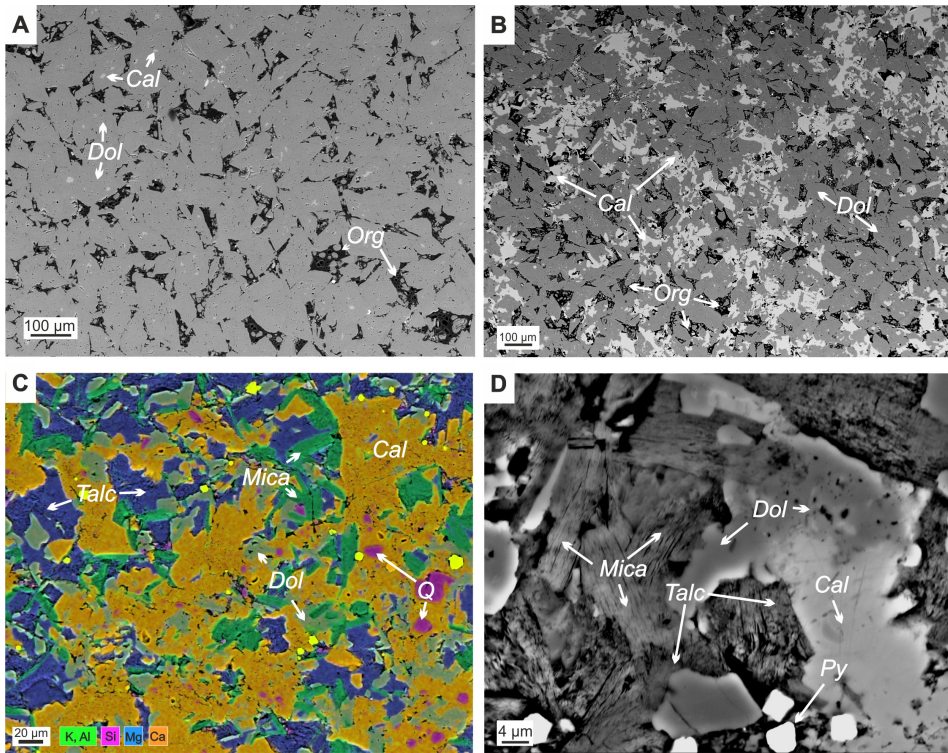


Figure 5. SEM images taken in back-scattered detector mode (BSD) and energy dispersive spectroscopy (EDS) elemental map from the OPH section (Kreitsmann et al., 2019 – PAPER I). (A) A sample from a depth of 1111.4 m, depicting massive unimodal planar-e dolomite crystals in organic matrix. (B) A sample from a depth of 1111.8 m, planar-e dolomite (marked with darkgrey) with secondary calcite (dedolomite, marked with light grey) in an organic matrix. (C) A sample from a depth of 1106.82 m, illustrating lower contact between carbonate bed A and mudstone. Note the anhedral calcite, remnant dolomite cores and abundant talc. (D) A sample from a depth of 1106.82 m, depicting the paragenesis of dedolomitization. Note the remnant dolomite core with secondary calcite and talc filling the pore space between dolomite and mica flakes.

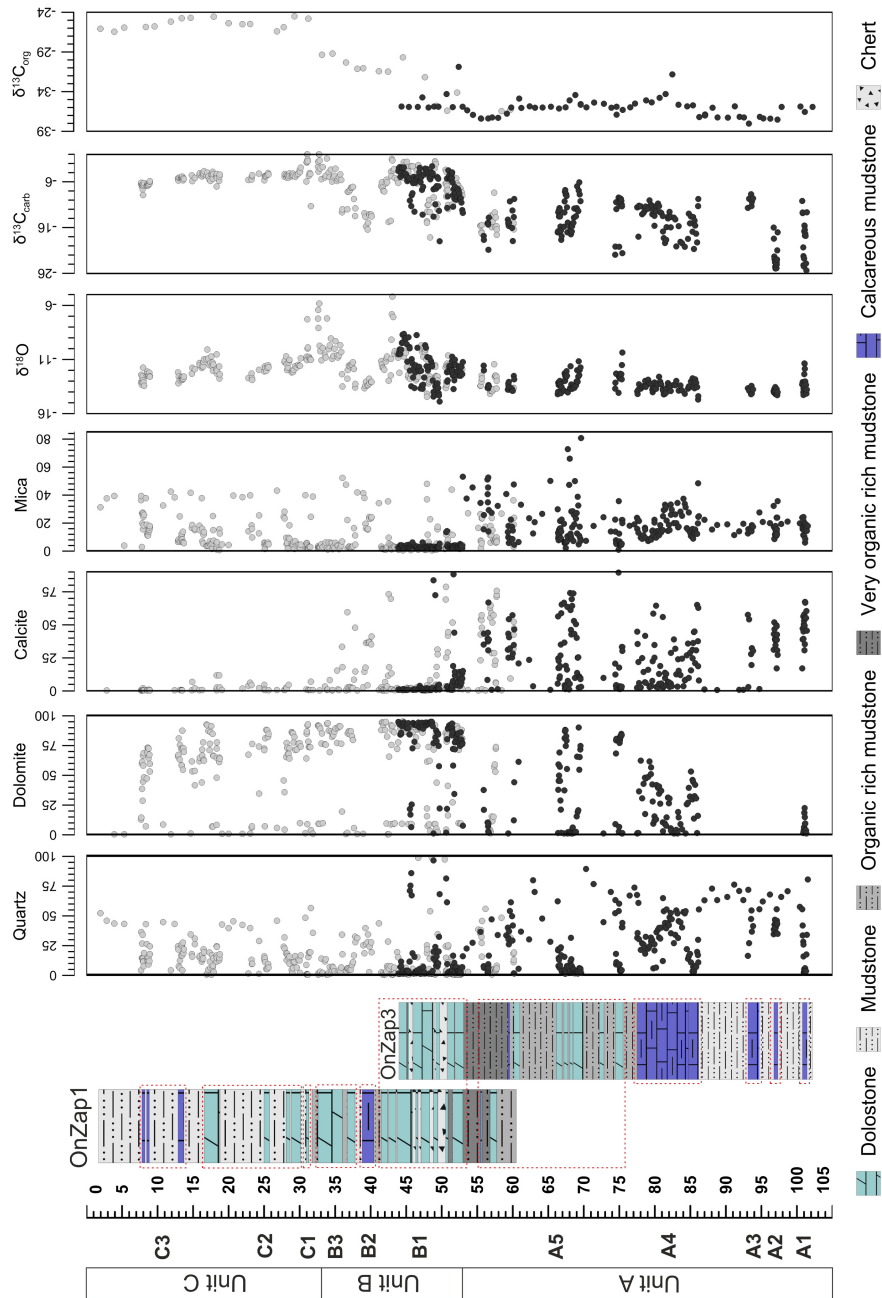


Figure 6. A lithostratigraphic column of the OnZap section (depth in meters) with an abundance of quartz, dolomite, calcite and mica in wt.% as well as isotopic values carbonate $\delta^{18}O$ and $\delta^{13}C$ (‰, VPDB). $\delta^{13}C_{org}$ (‰, VPDB). The dashed red boxes define carbonate bed intervals (from A1 to C3; Paiste et al., 2018 – PAPER II; Kreitsmann et al., submitted – PAPER IV).

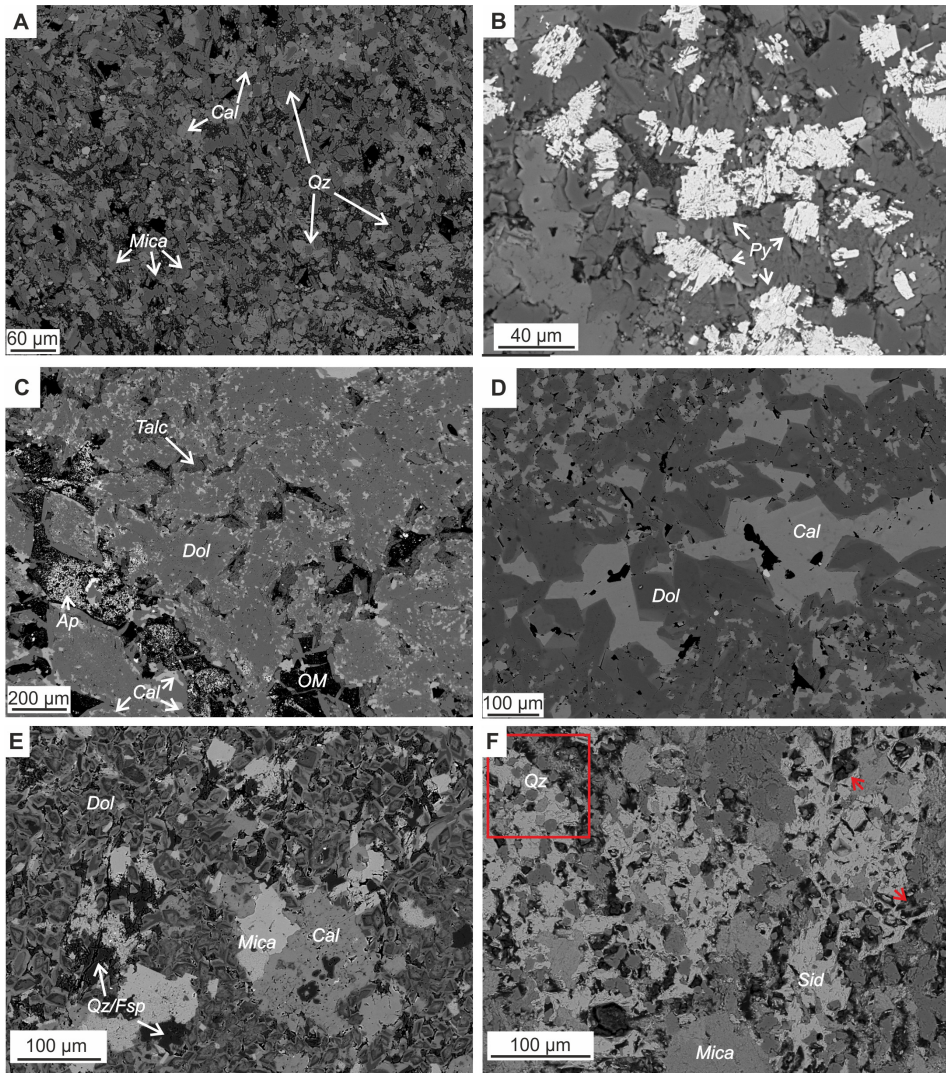


Figure 7. SEM BSE images from the OnZap section (Kreitsmann et al., submitted – PAPER IV). (A) Calcite cement with small primary methane-derived calcite crystals. Note the abundance of mica and quartz grains as well as the absence of talc and dolomite; A2, from a depth of 97.19 m. (B) Skeletal pyrite pseudomorphs, possibly after barite; A2, from a depth of 96.95 m. (C) Large planar-s dolomite crystals with abundant small calcite inclusions; B1, from a depth of 50.77 m. (D) Secondary calcite and dolomite filling the cavity. The dolomite in the slightly lighter areas is more enriched in Fe than that in the darker areas; B1, from a depth of 52.92 m. (E) Small planar-e strongly zoned dolomite/ankerite crystals and larger poikilitic calcite aggregate; C2, from a depth of 18.72 m. (F) Poikilitic siderite aggregates with abundant dissolution marks (marked with a red arrow). Note the well-rounded silt-sized quartz grains in the red square; C3, from a depth of 6.5m.

4.2. Carbon, O, and Sr isotope composition

The carbon and oxygen stable isotope composition of the carbonate beds from the OPH section is shown in Supplementary table 2 in Kreitsmann et al. (2019 – PAPER I). The first order trends are similar in all four beds: on the margins they all show lower $\delta^{13}\text{C}_{\text{carb}}$ and $\delta^{18}\text{O}_{\text{carb}}$ (hereafter $\delta^{18}\text{O}$) values than in the bed interiors (Fig. 4). Values of $\delta^{13}\text{C}_{\text{carb}}$ vary between -16.9 to 0.6‰ . The highest values within the interiors can vary by as much as 5‰ between individual carbonate beds. However, the $\delta^{13}\text{C}_{\text{carb}}$ values become consistently lower towards the margins, with the minimum values reaching -16.9‰ . The $\delta^{18}\text{O}$ values range from -15.1 to -6.0‰ . The $\delta^{13}\text{C}_{\text{org}}$ values of the organic matter in most of the carbonate beds are relatively stable around $-35.0\text{‰} \pm 2.5\text{‰}$, with the lowest value yielding -37.5‰ . However, a 1 meter thick interval in the carbonate bed A at a depth of about 1105 m shows a gradual increase in $\delta^{13}\text{C}_{\text{org}}$ to as high as -24.3‰ . This interval is the one with the highest $\delta^{13}\text{C}_{\text{org}}$ values (from -26.3 to -24.3‰), overlapping with the highest $\delta^{13}\text{C}_{\text{carb}}$ values (from -0.5 to 0.6‰ ; Fig. 4). Strontium isotope ratios are highly variable, with $^{87}\text{Sr}/^{86}\text{Sr}$ values remaining between 0.7139 and 0.7192 in the calcite-rich samples and between 0.7062 and 0.7108 in the dolomite-rich samples (Fig. 10 in Kreitsmann et al., 2019 – PAPER I).

Sequential dissolution experiments carried out with six OPH samples show that the CO_2 extracted during the first step (20 min and 25 °C) was depleted in ^{13}C and ^{18}O up to 5‰ and 3‰ , respectively, compared to the CO_2 extracted during the second step (8 h and 70 °C ; Fig. 9 and Supplementary table 3 in Kreitsmann et al., 2019 – PAPER I). The $\delta^{18}\text{O}$ values of dolomite exhibit a systematic decreasing trend with an increasing abundance of calcite, whereas the difference with the calcite end-member in the same sample is in the range of $0.3\text{--}2.8\text{‰}$. The $\delta^{13}\text{C}_{\text{carb}}$ values of dolomite, however, remain relatively stable and presumably unchanged until calcite abundance reaches c. 50% of total carbonate. A decreasing trend of dolomite $\delta^{13}\text{C}_{\text{carb}}$ values has only developed in the samples with $>50\%$ calcite. Such isotope trends of dolomite indicate the O isotope resetting of all samples, regardless of the extent of dedolomitization and the calcite/dolomite ratio, whereas C isotope to do not reset until calcite/dolomite ratio reaches c. 50%.

The carbonate $\delta^{13}\text{C}$ and $\delta^{18}\text{O}$ values from the OnZap section is shown in Fig. 6 and in Supplementary table 1 in Kreitsmann et al. (submitted – PAPER IV). Two distinct calcareous mudstone in the A1 ad A2 intervals in the lower part of Unit A are characterized by the lowest $\delta^{13}\text{C}_{\text{carb}}$ values (min. -25.3‰). Unlike other carbonate beds in the OnZap section, their $\delta^{13}\text{C}_{\text{carb}}$ values increase towards the bed margins (Fig. 8). A3 has relatively uniform $\delta^{13}\text{C}_{\text{carb}}$ values (around -10.2 ± 1.0), whereas heterogeneous calcareous mudstones (A4) and dolostones (A5) exhibit a variable isotope signal. The dolospar in B1 shows a large intrabed variation of $\delta^{13}\text{C}_{\text{carb}}$ and $\delta^{18}\text{O}$ values, which reduce towards the upper part of the interval. This variation is associated with calcite-rich contacts between mudstone and/or silica veins with dolostone. In general, Unit B shows a $\delta^{13}\text{C}_{\text{carb}}$ trend from -12.8‰ to -1.0‰ in B1, a decrease back to -16.4‰ in the calcareous mudstones of B2 and an increase to values near zero in B3 (Fig. 6). The C1 interval exhibits

variable $\delta^{13}\text{C}_{\text{carb}}$ and $\delta^{18}\text{O}$ values, ranging from -11.3 to $+0.8\%$ and from -11.1 to -5.8% , respectively. In C2 $\delta^{13}\text{C}_{\text{carb}}$ values decrease from -2.9% to -6.2% and $\delta^{18}\text{O}$ values from -10.9% to -13.4% towards the top of the C3 interval (Fig. 6).

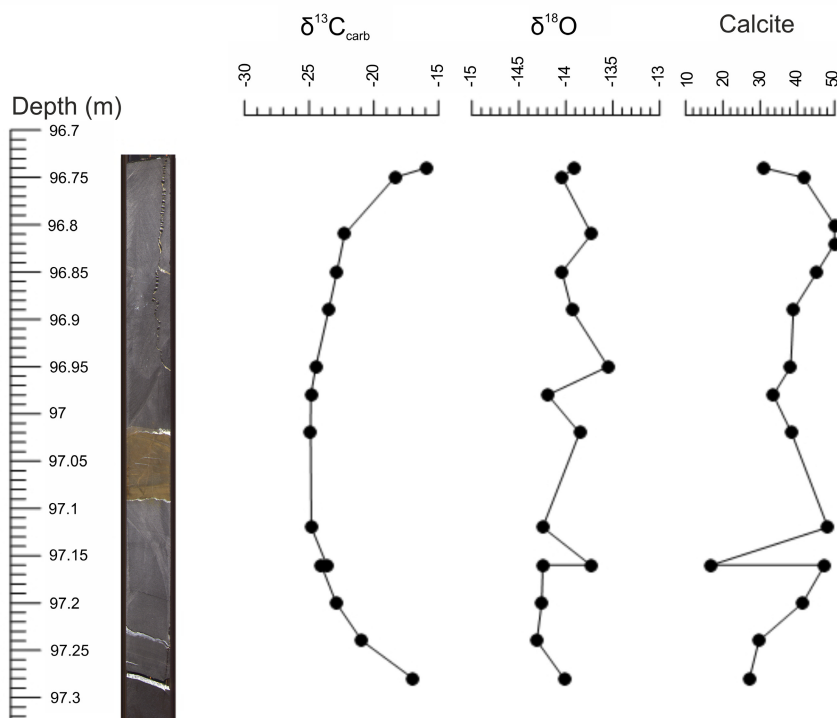


Figure 8. The carbonate $\delta^{18}\text{O}$ and $\delta^{13}\text{C}$ (‰, VPDB) values and calcite abundance (wt.%) in the methane-derived carbonate interval A2 with primary calcite. The $\delta^{13}\text{C}_{\text{carb}}$ values of the interior of the calcareous mudstone bed are lower than those of the margin.

4.3 Rare earth elements + yttrium systematics

PAAS-normalized rare earth element patterns in the studied carbonate samples show distinct characteristics in the different units of the OnZap section (Fig. 9; Supplementary table 3 in Kreitsmann et al., submitted – PAPER IV). In Unit A ($n = 13$), the total REE (ΣREE) concentrations range between 19.19–159.16 ppm (mean = 46.79 ± 40.05 ppm). The Y/Ho ratios are slightly above the chondritic ratio of 27 and range from 29.09 to 37.32 (mean = 33.46 ± 2.63). Unit A shows positive La_{SN} anomalies [$(\text{La}/\text{La}^*)_{\text{SN}}$] ranging from 0.92 to 1.73 (mean = 1.42 ± 0.29 , excluding two outliers, -13.62 and 12.15) and positive Gd_{SN} anomalies [$(\text{Gd}/\text{Gd}^*)_{\text{SN}}$] ranging from 1.08 to 1.31 (mean = 1.20 ± 0.07). In addition, LREE are depleted compared to HREE, as shown by the $\text{Pr}_{\text{SN}}/\text{Yb}_{\text{SN}}$ ratios between 0.09 and 1.15, mean = 0.45 ± 0.31 . The samples in Unit A are enriched in MREE compared to LREE and HREE, with BSI varying from 0.97

to 1.69 (mean = 1.41 ± 0.22). There are strong positive Eu_{SN} anomalies $[(\text{Eu}/\text{Eu}^*)_{\text{SN}}]$ in Unit A with values between 1.17 and 3.21 (mean = 1.79 ± 0.5). The Ce_{SN} anomaly $[(\text{Ce}/\text{Ce}^*)_{\text{SN}}]$ values vary from 0.58 to 0.89 (mean = 0.75 ± 0.1) in Unit A.

In the carbonate samples of Unit B ($n = 12$), the ΣREE values range from 4.44 to 41.17 ppm (mean = 16.27 ± 11.51 ppm). The Y/Ho ratios range from 32.98 to 49.63 (mean = 39.01 ± 4.28), constituting the highest among all units. Unit B has positive La_{SN} and Gd_{SN} anomalies, ranging between 1.16 and 1.70 (mean = 1.41 ± 0.15), and between 1.20 and 1.37 (mean = 1.27 ± 0.05), respectively. LREE are depleted compared to HREE with $(\text{Pr}/\text{Yb})_{\text{SN}}$ ratios ranging from 0.09 to 0.60 (mean = 0.32 ± 0.14). Unit B does not show any significant MREE enrichment and BSI values range between 0.92 and 1.22 (mean = 1.04 ± 0.10 ; Fig. 7). Compared to other units, its Eu_{SN} anomalies are smaller, but still positive, varying from 0.82 to 2.40 (mean = 1.65 ± 0.52). The $(\text{Ce}/\text{Ce}^*)_{\text{SN}}$ values have the largest negative anomalies, varying between 0.40 and 0.91 (mean = 0.68 ± 0.13).

Unit C is dominated by shales, thus only four carbonate samples were chosen for trace elements analyses, most of which show a strong contribution from siliciclastic fraction. This is indicated by the high Sc, Zr and Th concentrations, in some samples reaching as high as 12.45, 110.97, and 3.51 ppm, respectively (Supplementary table 2 in Kreitsmann et al., submitted – PAPER IV). The ΣREE ranges from 11.74 to 69.14 ppm (mean = 33.35 ± 22.13 ppm). The Y/Ho ratios are similar to the chondritic values between 23.92 and 33.73 (mean = 28.86 ± 3.53). In Unit C, the $(\text{La}/\text{La}^*)_{\text{SN}}$ varies between 0.88 and 1.38 (mean = 1.07 ± 0.20) and $(\text{Gd}/\text{Gd}^*)_{\text{SN}}$ varies from 1.09 to 1.18 (mean = 1.13 ± 0.03). It has slight LREE depletion with $(\text{Pr}/\text{Yb})_{\text{SN}}$ varying between 0.41 and 0.88 (mean = 0.69 ± 0.18). Unit C shows the highest MREE enrichment (BSI varies from 1.18 to 2.03, mean = 1.57 ± 0.33) and positive Eu_{SN} anomalies, with $(\text{Eu}/\text{Eu}^*)_{\text{SN}}$ ranging from 1.30 to 2.66 (mean = 1.95 ± 0.50). Cerium does not show any anomalous behaviour, with $(\text{Ce}/\text{Ce}^*)_{\text{SN}}$ ranging from 0.93 to 1.02 (mean = 0.98 ± 0.03).

In the Pilgujärvi SF, REY were analyzed in phosphatic grains, which are subdivided into four petrographically defined groups (A, B, C and D; Joosu et al., 2016 – PAPER III). This thesis focuses on the best-preserved type D phosphatic grains that record conditions during apatite precipitation. In addition, REY were analyzed in the apatite from siltstone, where apatite occurs in the form of cement (hereafter, apatite cement). In type D phosphatic grains, the ΣREE ranges from 769 to 1716 ppm (mean = 1366 ± 380 ppm), while in apatite cement it ranges from 571 to 1535 ppm (mean = 906 ± 327 ppm). Y/Ho ratios vary between 40.1–49.9 (mean = 44.9 ± 2.9) in type D phosphatic grains and between 37.2–46.1 (mean = 42.8 ± 2.9) in apatite cement. Type D grains have a relatively flat REY_{SN} pattern, with BSI varying from 1.1 to 1.34 (mean = 1.18 ± 0.1 ; Fig. 10A). Apatite cement is slightly enriched in MREE, with BSI varying from 1.27 to 1.62 (mean = 1.45 ± 0.13 ; Fig. 10B). Type D grains show weak positive Eu_{SN} anomalies, ranging between 1.23 and 1.65 (mean = 1.44 ± 0.15), whereas apatite cement

shows strong Eu_{SN} anomalies, ranging between 2.01 and 3.98 (mean = 2.73 ± 0.63). Apatite cement does not exhibit anomalous Ce behavior (mean $(\text{Ce}/\text{Ce}^*)_{\text{SN}} = 1.02 \pm 0.03$), but the Ce_{SN} anomalies vary between 0.67–0.83 (mean = 0.76 ± 0.05) in type D grains, with some samples exhibiting a real negative Ce_{SN} anomaly (i.e., $(\text{Pr}/\text{Pr}^*)_{\text{SN}} > 1.05$; Fig. 14).

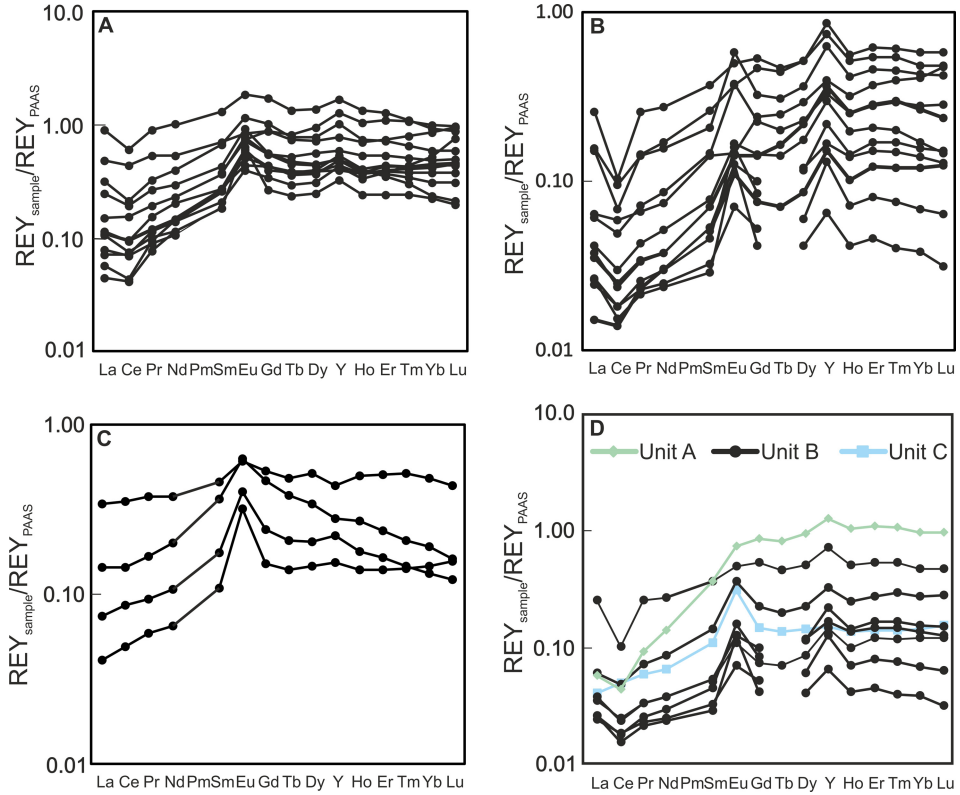


Figure 9. REY_{SN} patterns of (A) Unit A, (B) Unit B, (C) Unit C, and (D) samples from all units that passed screening (i.e., $\text{Zr} < 4$ ppm; Kreitsmann et al., submitted – PAPER IV). Unit A has a highest concentration of REY and shows MREE enrichment compared to LREE and HREE. Unit B has a coherent pattern, but it varies in REY concentration. Unit C is also enriched in MREE compared to other REE and does not show anomalous behavior other than a positive Eu_{SN} anomaly. The samples from Units A and C have a strong shale contamination and only one sample from each unit passed the screening.

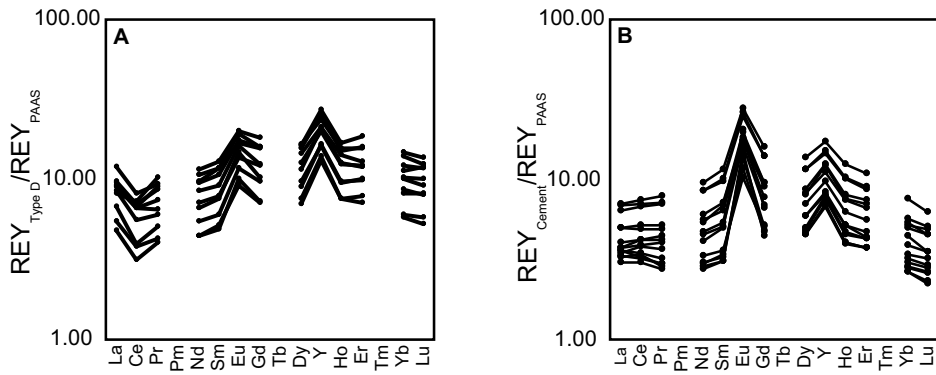


Figure 10. (A) REY_{SN} pattern of type D apatite grains and (B) apatite cement from the Pilgijärvi SF (after Joosu et al., 2016 – PAPER III; Kreitsmann et al., 2016). Both groups show a coherent pattern with varying REY concentrations. Tb and Tm were not measured.

5. DISCUSSION

5.1 Secondary alteration in the Upper Zaonega Formation

Carbonate rocks are typically considered capable of retaining syndepositional $\delta^{13}\text{C}_{\text{carb}}$ values under diagenetic recrystallization and low-grade metamorphism (Hood et al., 2018; Schidlowski, 2001; Swart, 2015; Valley and O'Neil, 1984). Their oxygen isotopic composition, on the other hand, is more prone to resetting (Banner and Hanson, 1990). However, in the presence of silicate minerals, metamorphic silicate-carbonate reactions can cause isotopic resetting of both carbon and oxygen isotopic composition through re-equilibration with metamorphic fluids and/or due to decarbonation reactions (Valley, 1986). Also, both the $\delta^{13}\text{C}_{\text{carb}}$ and $\delta^{18}\text{O}$ values can be significantly altered at a relatively lower temperature/pressure by meteoric diagenesis and diagenetic/hydrothermal dolomitization (Swart, 2015). Thus, the isotopic composition of carbonate phases can be altered under a variety of conditions. The preserved $\delta^{13}\text{C}_{\text{carb}}$ values are controlled by the composition of the original sediment, fluid, fluid/rock ratio during alteration, porosity, isotope fractionation factors, distribution coefficients and open-system versus closed-system behavior (Kreitsmann et al., 2019 – PAPER I; Banner and Hanson, 1990; Bishop et al., 2014; Zheng and Hoefs, 1993).

Jacobsen and Kaufman (1999) have shown that the carbon isotope composition of carbonate rock will change only at very high water/rock ratios. During the progressive alteration the oxygen and carbon isotope values follow an L-shaped declining curve (Bishop et al., 2014; Jacobsen and Kaufman, 1999). A similar L-shaped distribution of C- and O-isotope ratios in the OPH and OnZap sections (Fig. 11) warns for the complete resetting of the isotopic signal at the carbonate bed margins, which have experienced alteration at a high water/rock ratio. A simple mass-balance modelling exercise with OPH samples (Fig. 12 in Kreitsmann et al., 2019 – PAPER I) showed that the water/rock ratio had to be high ($W/R > 5$) in order to achieve $\delta^{13}\text{C}_{\text{carb}}$ values as low as those measured in calcite-rich samples.

The calcite crystallization in the Zaonega Formation (Črne et al., 2014) has been previously interpreted as being predominantly controlled by metamorphic calcite \pm talc paragenesis (Črne et al., 2014). This mineral association commonly develops in dolomitic rocks that have been subjected to metamorphic silica alteration. Dolomite replacement by calcite is accompanied by the degassing of both ^{13}C - and ^{18}O -enriched CO_2 by a few per mil, relative to the remaining carbonate material (Črne et al., 2014; Valley, 1986). The decrease in C-O isotope values combined with the intensification of dedolomitization and silicification when moving from the interior of carbonate beds outwards, to the bed margins, indicates that alteration was governed by a fluid-rock alteration along the lithological contacts. Fluid-controlled dedolomitization (Kreitsmann et al., 2019 – PAPER I) is the replacement of dolomite by calcite in the presence of a

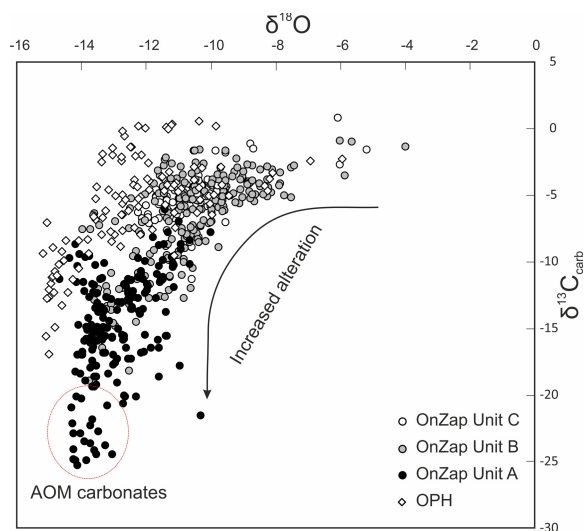


Figure 11. A cross-plot of $\delta^{13}\text{C}_{\text{carb}}$ and $\delta^{18}\text{O}$ (‰, VPDB) values from the OnZap and OPH sections. Note the L-shape field, suggesting a complete resetting of carbon and oxygen isotopic signals in some samples. Data from Kreitsmann et al. (2019 – PAPER I) and Kreitsmann et al. (submitted – PAPER IV).

water solution with elevated Ca^{2+} activity (Ayora et al., 1998). It requires the reacting fluid to have a low $\text{Mg}^{2+}/\text{Ca}^{2+}$ ratio and to be able to remove the liberated Mg^{2+} to maintain dolomite undersaturation (Ayora et al., 1998). Importantly, dedolomitization is known to occur under a wide variety of conditions, ranging from karst and shallow subsurface settings due to the interaction with meteoric waters at relatively low temperatures ($<50\text{ }^{\circ}\text{C}$) and CO_2 partial pressures (Flügel, 2010; Nader et al., 2008; Rameil, 2008; Vandeginste and John, 2012), to deep burial environments (Budai et al., 1984; Land and Prezbindowski, 1981; Schoenherr et al., 2018; Woo and Moore, 1996) and hydrothermal systems (e.g., Faust, 1949; Matsumoto et al., 1988; Stoessell et al., 1987), such as those envisaged for the Zaonega Formation. The intensification of dedolomitization at bed margins acted to reduce permeability (as documented, for example, in the Permian Zechstein carbonate rocks; Schoenherr et al., 2018), thereby shielding the middle part of carbonate beds from pervasive alteration. In addition, dedolomitization was hindered inside the carbonates beds due to their closed-system behavior with reduced supply of Ca^{2+} and/or slower removal of liberated Mg. Closed-system behavior can be also inferred from the carbon isotopic values which are fluid-buffered in the dedolomites from contact zones. However, when moving inward, the carbonate beds become rock-buffered due to limited fluid circulation (Kreitsmann et al., 2019 – PAPER I). Hence, there is a gradual increase in isotopic values and dolomite/calcite ratios from the mudstone-dolostone contacts, when moving inward towards the carbonate bed interiors (Fig. 4 and 6).

The fluid circulation responsible for dedolomitization was likely triggered by contemporaneous magmatic activity, when gabbroic bodies intruded unconsolidated wet sediments (Črne et al., 2013; Melezhik et al., 1999). Hydrothermal fluids carrying Ca, Si and CO₂ (and possibly CH₄ due to thermal cracking of organic matter; Kreitsmann et al., submitted – PAPER IV) would have been enriched in light carbon derived from the encasing organic-rich muds. Furthermore, the elevated Ca²⁺ activity would have been amply available from the underlying Tulomozero Formation. The latter is replete with quartz- and dolomite-pseudomorphed Ca-sulphate laths and nodules (Brasier et al., 2011; Melezhik et al., 2015) as well as the remarkable suite of evaporites recovered in the lower part of the OPH core (> 1 km deeper than studied dolomite horizon) that consist of halite and Mg-K-sulfate minerals, anhydrite and magnesite-mudstone (Blättler et al., 2018; Krupenik et al., 2011). The timing of fluid circulation would have been early enough for the mudstones to not yet be lithified and act as conduits for fluid migration. Thus, most of the dedolomitization is observed in the contact zones (e.g., the OPH carbonate beds and B1 interval from the OnZap section) of mudstones and carbonate beds, which would have been more lithified than mudstones. The massive dolomite horizon in Unit B from the OnZap section seems to act as a stratigraphic seal, hindering the further ascent of dedolomitizing fluids (Fig. 12; Kreitsmann et al., 2019 – PAPER I; Paiste et al., 2018 – PAPER II; Kreitsmann et al., submitted – PAPER IV).

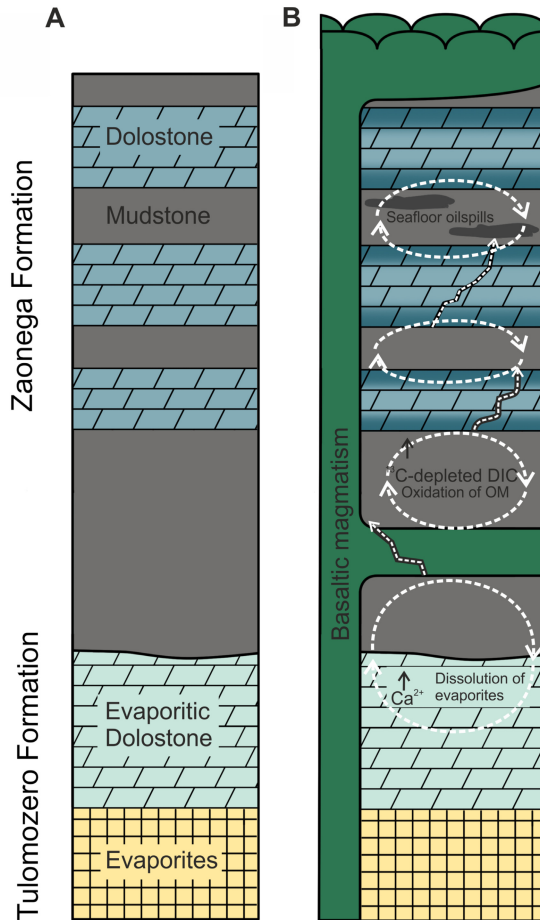


Figure 12. A conceptual dedolomitization model (Kreitsmann et al., 2019 – PAPER I). (A) describes the situation before magmatic activity initiated a hydrothermal alteration and (B) describes fluid movement during dedolomitization. The dashed white lines indicate that fluid circulation is more focused in mudstones, particularly in the contact zones between unlithified mudstone and semi-lithified carbonate beds. The dashed white lines with a black outline indicate the permeable zones in the carbonate beds that could have acted as conduits for vertical fluid movement. The source of Ca^{2+} is the dissolution of evaporites in the underlying Tulomozero Formation that moved upward due to the hydrothermal circulation initiated by the magmatic activity during the Zaonega times. Magmatic activity also triggered the migration of hydrocarbons (i.e., pyrobitumen veins and seafloor oil spills; Qu et al., 2012). The dark blue outer edges of the carbonate beds show the area of dedolomitization exhibiting lower $\delta^{18}\text{O}$ and $\delta^{13}\text{C}$ values than the better-preserved interiors of carbonate beds.

5.2. Preservation of the $\delta^{13}\text{C}_{\text{carb}}$ signal

The organic-rich mixed siliciclastic-carbonate sediments of the Zaonega Formation were deposited in a volcanically active basin (Kreitsmann et al., 2019 – PAPER I; Paiste et al., 2018 – PAPER II; Kreitsmann et al., submitted – PAPER IV; Črne et al., 2014; Melezhik et al., 2015). Given the complex postdepositional history, the carbonate rocks of the Zaonega Formation have experienced secondary overprints (e.g., dedolomitization as described above, but also diagenesis and regional metamorphism), resulting in heterogeneous mineralogy. Hence, it is of utmost importance that the extent of secondary alteration is assessed, in order to screen the better-preserved samples, which can be then used for paleoenvironmental reconstruction and comparison with previously published $\delta^{13}\text{C}_{\text{carb}}$ secular trends. In open-marine carbonates, the extent of alteration is often evaluated by using the Mn/Sr ratio. During the recrystallization caused by metamorphic and/or diagenetic fluids, Sr is preferentially removed and Mn is introduced (Brand and Veizer, 1980). Hence, a Mn/Sr ratio of >10 has been commonly used to identify altered samples among the better-preserved ones in the Precambrian successions (Kaufman and Knoll, 1995; Melezhik et al., 2015). In the OPH section (Kreitsmann et al., 2019 – PAPER I), the Mn/Sr ratio is <10 in all samples, with the higher ratios occurring in dolomite-rich samples (Mn/Sr 2 – 8) and lower ratios in calcite-rich samples (Mn/Sr <3 ; Figure 10C in Kreitsmann et al., 2019 – PAPER I). In the OnZap samples, the Mn/Sr ratio ranges between 1 and 110, with a magnitude of higher ratios being found in Unit C (Kreitsmann et al., submitted – PAPER IV). Excluding the anomalous Mn/Sr ratios in Unit C of the OnZap section, the average Mn/Sr value is 9.02 ± 7.25 and 7.53 ± 4.4 in Units A and B, respectively. This suggests that Mn/Sr ratio should be used cautiously in the Upper Zaonega Formation, because the ratio suggests that calcite-rich samples should be better preserved than dolomite-rich samples. However, petrographic, mineralogical and isotopic observations show a clear influence of secondary alteration (Kreitsmann et al., 2019 – PAPER I; Kreitsmann et al., submitted – PAPER IV). This discrepancy can be explained with additional Sr having leached from the micas in the calcite-rich samples and/or Sr inherited from the underlying Tulomozero Formation, which was incorporated into calcite during dedolomitization (Kreitsmann et al., 2019 – PAPER I). Lastly, calcite preferentially incorporates Sr, whereas dolomite takes in Mn (Veizer, 1983). Hence, in the case of mixed carbonate mineralogy the Mn/Sr ratio could erroneously point towards secondary calcites having a better-preserved signal than dolomite.

To screen the $\delta^{13}\text{C}_{\text{carb}}$ and $\delta^{18}\text{O}$ values we follow a method similar to the one previously applied by Črne et al. (2014) in correlative FAR-DEEP cores, who described that calcite is typically a secondary and dolomite a primary carbonate phase in the Upper Zaonega carbonate beds. However, we use it with the caveat that some of the calcite is most likely also primary (e.g., the carbonate intervals A2 and B2 in the OnZap section) and that there are examples of rare secondary dolomite (interval C1 in the OnZap section; Fig. 7D). Nevertheless, the general approach still maintains that most of the dolomite is preserved better than calcite.

In the OnZap section (Fig. 13), a calcite/total carbonate ratio of <0.05 was used as a cut-off value to screen the better-preserved samples (Kreitsmann et al., submitted – PAPER IV). In the OPH section, no secondary dolomite or primary calcite was identified and the calcite/total carbonate ratio of <0.1 was applied to samples with the total carbonate wt.% > 90% (Fig. 13; Kreitsmann et al., 2019 – PAPER I).

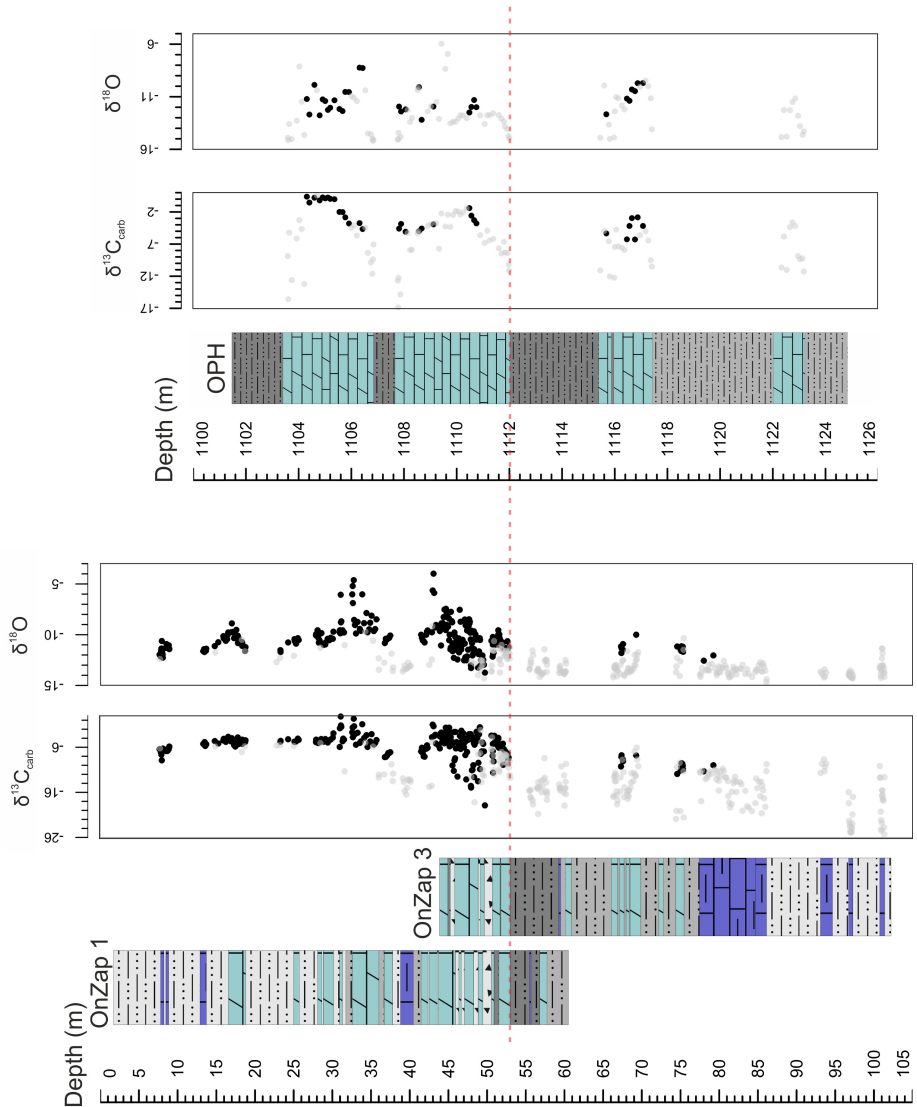


Figure 13. The screened $\delta^{13}\text{C}_{\text{carb}}$ and $\delta^{18}\text{O}$ values (‰, VPDB) are marked as black dots. The samples that did not pass the screening are marked as light grey dots. The dashed red lines mark the marker lithological boundary that is used for correlation between the OnZap and OPH drill cores. Data is from Kreitsmann et al. (2019 – PAPER I) and Kreitsmann et al. (submitted – PAPER IV).

5.3. Screening for the carbonate REY_{SN} signal

In order to use the carbonate REY_{SN} signal as a paleoenvironmental indicator, it is crucial to screen the samples for contamination that could obscure the primary environmental signal. The possible sources of contamination are clastic siliciclastic detritus, Fe-Mn oxides, sulphides, and phosphates (Bau, 1993; Kamber et al., 2014; Wang et al., 2018) that can carry considerably higher concentrations of REY than pure carbonates. The most common among the possible contaminants is the siliciclastic detritus component, which is commonly incorporated into carbonates during their deposition. It carries an order of magnitude higher REY concentration and has a distinct flat REY_{SN} pattern (Taylor and McLennan, 1985). Nothdurft et al. (2004) has shown that even 1–2% of shale contamination can obscure the REY_{SN} pattern of carbonates.

The extent of shale contamination is commonly monitored by using the concentrations of immobile trace elements (e.g., Zr and Th; Bau, 1993; Bolhar and Van Kranendonk, 2007; Frimmel, 2009; Kamber et al., 2014; Viehmann et al., 2015; Zhao and Zheng, 2017) and by observing whether these elements correlate with typical seawater features, such as a positive La_{SN} anomaly and a supra-chondritic Y/Ho ratio (Viehmann et al., 2015, Wang et al., 2018). Siderophile Ni and Cu can be monitored for contamination by oxides and chalcophile Pb and Sc for contamination by sulphides (Bolhar and Van Kranendonk, 2007). In order to assess the effect of phosphates to the carbonate REY_{SN} pattern, the bell-shaped index can be calculated as phosphates are usually enriched in MREE compared to other REE (Joosu et al., 2016 – PAPER III; Joosu et al., 2015; Tostevin et al., 2016). A Zr concentration <4 ppm as suggested by Frimmel (2009) was used as the cut-off value to screen uncontaminated carbonate samples. Due to the possible presence of diagenetic carbonates in Unit C of the OnZap section, the Σ REE was used instead of the Y/Ho ratio and La_{SN} anomaly, to assess the possible contamination. Carbonates have typically low REE concentrations and if contaminants were present, the Σ REE concentration would have been increased, meaning that a binary plot of immobile trace elements versus Σ REE concentration should show a positive correlation. The screened OnZap samples did not show such correlation, meaning that they can be considered to be uncontaminated by a siliciclastic component, oxides or sulphides (Fig. 11 in Kreitsmann et al., submitted – PAPER IV). In addition, the XRD data suggest that apatite concentration does not exceed 1.2 wt%, commonly remaining <1 wt% in the screened samples. Moreover, the sample with the highest apatite abundance has the lowest Σ REE concentration (Supplementary table 2 in Kreitsmann et al., submitted – PAPER IV).

It is generally agreed that dolomitization and recrystallization during burial diagenesis do not have a significant effect on the REY_{SN} signature (Banner et al., 1988; Bau and Alexander, 2006; Frimmel, 2009; Hood et al., 2018; Webb et al., 2009). The original REY_{SN} signal of the carbonate rock would only be influenced at very high water/rock ratios and nearly complete dissolution/recrystallization (Kamber and Webb, 2001; Nothdurft et al., 2004). However, in clay-rich

sediments REY can be mobilized from clay minerals to diagenetic carbonates (Schieber, 1988), overprinting the primary signals. In the Upper Zaonega Formation some of the carbonate bed contacts have experienced alteration at high water/rock ratios, as evidenced by the dedolomitization and resetting not only the $\delta^{18}\text{O}$ but also the $\delta^{13}\text{C}_{\text{carb}}$ signal (Kreitsmann et al., 2019 – PAPER I; Kreitsmann et al., submitted – PAPER IV). Dedolomitized samples also have an elevated Zr concentration and none of them passed the screening. Due to the relatively high abundance of siliciclastic fraction, only 9 out of 29 samples passed the screening. They include one sample from intervals A5, B3 and C2 as well as six samples from interval B1 (Fig. 11 and Supplementary table 3 in Kreitsmann et al., submitted – PAPER IV). These samples retained their original REY signal, meaning that they could be used as reliable archives for paleoenvironmental conditions.

5.4. Bed scale variation and stratigraphic $\delta^{13}\text{C}_{\text{carb}}$ trends in the Upper Zaonega carbonates

The margins of carbonate beds in the OPH and OnZap successions are typically dedolomitized and characterized by the presence of secondary calcite with ^{13}C and ^{18}O -depleted isotopic composition. However, intervals A1 and A2 in the OnZap section have a distinct reverse interior to margin $\delta^{13}\text{C}_{\text{carb}}$ pattern when compared to the other carbonate beds. Their $\delta^{13}\text{C}_{\text{carb}}$ values become increasingly heavier towards the margins of the beds, when compared to the interior parts, which have $\delta^{13}\text{C}_{\text{carb}}$ values as low as -25‰ (Fig. 8). These low $\delta^{13}\text{C}_{\text{carb}}$ values could represent methane-derived carbonates formed *via* the anaerobic oxidation of methane (AOM) in an ancient seep system, whereas the higher $\delta^{13}\text{C}_{\text{carb}}$ values on the margins represent the secondary alteration similarly to other carbonate bed margins. The AOM in hydrocarbon seeps are widely described in modern environments, but examples can also be found in Precambrian (Campbell, 2006). The ^{13}C -depleted carbon source for the precipitation of authigenic seep carbonates is supplied by microbially mediated anaerobic oxidation of hydrocarbons, such as methane and oil (Boetius et al., 2000; Joye et al., 2010), and typically within shallow subsurface sediments. At these settings the hydrocarbons rising through unconsolidated sediments are anaerobically oxidized at the lower boundary of the sulphate reduction zone by a microbial consortia of methanotrophic archaea and sulphate-reducing bacteria (Boetius et al., 2000; Orphan et al., 2002; Whiticar, 1999). The AOM increases pore-water alkalinity and consequently causes the precipitation of carbonates, with ^{13}C -depleted signatures depending on the origin of methane. Biogenic methane produced by methanogens is highly depleted in ^{13}C , its $\delta^{13}\text{C}$ values varying from -110 to -50‰ , typically being at $-60 \pm 5\text{‰}$ (Fig. 1; Sapart et al., 2012; Schoell, 1988). Thermogenic methane is typically characterized by higher $\delta^{13}\text{C}$ values of over -50‰ , reaching up to $-22 \pm 3\text{‰}$ in

pyrogenic methane (Sapart et al., 2012), which becomes heavier with the increasing maturity of organic matter (Whiticar, 1999).

These features are consistent with the environment in the Upper Zaonega Formation, where AOM-derived carbonates could form similarly to the way they form in the late Paleocene Vøring Basin (Norwegian Sea; Svensen et al., 2003) or in the modern seep systems in the Guayama Basin in the Gulf of California (Geilert et al., 2018; Simoneit et al., 1990), where magmatic activity has initiated a hydrothermal system producing seep carbonates. Usually the AOM-derived carbonates derived from microbial methane have $\delta^{13}\text{C}_{\text{carb}}$ values $< -30\text{‰}$ (Campbell, 2006), but the isotope composition of the carbonate precipitating in the system is strongly influenced by the relative share between DIC derived from AOM and seawater. Hence, seep carbonates carry a mixed $\delta^{13}\text{C}$ signal from two different DIC pools (Himmler et al., 2010). Alternatively, this variability can reflect the variation in the source of methane, i.e., a microbial vs. a thermogenic origin. The slightly higher $\delta^{13}\text{C}_{\text{carb}}$ values in the OnZap carbonate intervals A1 and A2, when compared to the average methane-derived carbonates, can be explained by its mixing with the seawater DIC pool and by thermogenic CH_4 being the dominant source. This is consistent with the isotopic and lithological indicators of hydrocarbon generation and seepage during the accumulation of middle/upper part of the Zaonega Formation (Qu et al., 2018, 2012) as well as the active sulphate reduction inferred from the sulphur isotopes from the OnZap section (Paiste et al., 2018 – PAPER II). The AOM-derived origin of these carbonate beds is also exemplified by the presence of putative barite pseudomorphs (Fig. 5B). Barite is a common precipitate at the sulphate–methane interfaces in the methane/hydrocarbon seeps, where fluids from anoxic sediments containing methane and Ba^{2+} (leached from K-bearing minerals) mix with seawater near in the AOM zone (Castellini et al., 2006; Griffith and Paytan, 2012).

The petrography of the OnZap A3 calcareous mudstone resembles that of other AOM intervals (e.g., fine-grained calcite cement). However, the $\delta^{13}\text{C}_{\text{carb}}$ values of A3 are relatively high and stable at c. $10.2 \pm 1\text{‰}$, especially when compared to other calcite-rich samples. Further upward the varying dolomite/calcite ratio and the carbon isotopic signal of the calcareous mudstone interval A4 of the OnZap section is possibly a result of two processes that have at least partially overprinted the original isotopic signal. Firstly, the A4 interval has experienced intensive dedolomitization either due to Ca-rich fluids (Kreitsmann et al., 2019 – PAPER I) or the metamorphic reaction between dolomite and a silica-rich fluid (Črne et al., 2014). Secondly, the organic-rich calcareous mudstone in A4 has also experienced recycling of organic matter (i.e., microbial oxidation of OM). Depending on the relative concentration of bicarbonate produced *via* microbial oxidation of OM relative to the total amount of carbon in the system, organic diagenesis can decrease or increase (e.g., through methanogenesis) the $\delta^{13}\text{C}_{\text{carb}}$ values of carbonate rocks (Irwin et al., 1977; Mazzullo, 2000; Swart, 2015). In organic-rich calcareous mudstones the influence of the organic diagenesis was more prominent than in the dolostone intervals in Unit B and C. Dolostones are more pure carbonates with a lower concentration of organic

matter (Paiste et al., 2018 – PAPER II). Hence, even if organic diagenesis took place, it was not enough to influence the $\delta^{13}\text{C}_{\text{carb}}$ values of the system, which remained rock-buffered.

Similar to the calcareous mudstone in A4, the dolostone intervals A5 and B1 in the OnZap section, which correlate to carbonate beds studied from the OPH section, both experienced dedolomitization at the contacts between the carbonate beds and mudstones, resulting in lower isotopic values on the margins than in the interiors (Kreitsmann et al., 2019 – PAPER I; Kreitsmann et al., submitted – PAPER IV). Intra-bed $\delta^{13}\text{C}_{\text{carb}}$ variation (more than 5‰; Fig. 13) is probably due to the varying influence of methanotrophic bicarbonate to the DIC pool of ambient seawater and/or organic diagenesis. The same transition from the highly scattering negative $\delta^{13}\text{C}_{\text{carb}}$ values in the lower part of the Upper Zaonega Formation, trending from –6 to –2‰, has been also described in FAR-DEEP cores, (Črne et al., 2014; Melezhik et al., 2015) suggesting a basin-wide nature of this trend. Nevertheless, the variable scattering of intra-bed $\delta^{13}\text{C}_{\text{carb}}$ values in the OnZap, OPH and FAR-DEEP cores (Kreitsmann et al., 2019 – PAPER I; Kreitsmann et al., submitted – PAPER IV; Črne et al., 2014) suggests wide lateral/local isotopic variability for the DIC pool in the Onega Basin during the precipitation of the Upper Zaonega Formation. This variability possibly reflects the basinal methane influence into the DIC pool. In that case, the carbonate $\delta^{13}\text{C}_{\text{carb}}$ values depend on the proximity of the area of carbonate precipitation to active methane and/or oil seeps.

In the calcareous mudstone interval B2 of the OnZap section, the $\delta^{13}\text{C}_{\text{carb}}$ values of screened samples decrease from +0.8‰ to –8.9‰. This excursion also coincides with the transition from biomass having methanotrophic contribution ($\delta^{13}\text{C}_{\text{org}}$ values of –40‰ to –35‰) to predominantly phototrophic biomass ($\delta^{13}\text{C}_{\text{org}}$ values of –25‰; Fig. 4). In addition, the overlying dolostone intervals C1, C2 and C3 differ notably from the other carbonate intervals in Mn/Sr ratio, REY_{SN} patterns, petrography and mineralogy. Dolomite is typically zoned, becoming increasingly more Fe-rich towards the top of the succession as the dolomite composition changes to ankerite with siderite aggregates (Fig. 6 in Kreitsmann et al., submitted – PAPER IV). Petrography and carbon isotopes suggest that the dolomite in Unit C is mainly of diagenetic origin, having been precipitated from Fe-rich anoxic pore-waters.

5.5. The secular $\delta^{13}\text{C}_{\text{carb}}$ curve of the Zaonega Formation

Based on the petrographical, mineralogical and chemical criteria, the screening of carbonate isotope data for the OPH (Kreitsmann et al., 2019 – PAPER I) and the OnZap sections (Kreitsmann et al., submitted – PAPER IV) show that similarly to the Upper Zaonega Formation in FAR-DEEP 13A and 12AB drill cores, the least altered carbonate samples are situated in the middle part of carbonate beds (Črne et al., 2014; Melezhik et al., 2015). Most of the samples in Unit A did not pass the calcite/total carbonate ratio screening. However, if we

also consider the calcite in the A2 interval to be primary, as suggested by its petrography, then we see a trend of upward increasing $\delta^{13}\text{C}_{\text{carb}}$ from -24.9‰ in the AOM carbonates to -7.8‰ in the best-preserved dolomites (Fig. 13). Meanwhile, the $\delta^{13}\text{C}_{\text{carb}}$ values in the correlative OPH section reach -3‰ (Fig. 13). The screened $\delta^{13}\text{C}_{\text{carb}}$ values in Unit B are highly variable, ranging from -18.9‰ to -0.9‰ . If we exclude the dolomite-rich samples that may have been influenced by secondary processes without experiencing intensive dedolomitization (i.e., samples close to the secondary veins and brecciated intervals), the $\delta^{13}\text{C}_{\text{carb}}$ values in the OnZap section increase from -8.5‰ to the normal marine value of 0‰ and from -4.5‰ to 0.5‰ in the correlative OPH section. In Unit C, $\delta^{13}\text{C}_{\text{carb}}$ values show slight intra-bed variation, decreasing upward from 0.8‰ to -8.9‰ .

Karhu and Holland (1996) and Melezhik et al. (2007) have suggested that the LJE was followed by a sharp, possibly global decrease in $\delta^{13}\text{C}_{\text{carb}}$ values. Salminen et al. (2013) have described a $\delta^{13}\text{C}_{\text{carb}}$ trend from c. -2‰ to 3‰ in the 2056 ± 0.8 Ma Kolosjoki Sedimentary Formation (Martin et al., 2013b) in the Pechenga Greenstone Belt. A similar slight negative excursion in the $\delta^{13}\text{C}_{\text{carb}}$ values has been described in other post-LJE successions (e.g., Belcher Group in subarctic Canada and in Il'mozero Sedimentary Formation from Imandra-Varzuga Greenstone Belt; Hodgskiss et al., 2019; Melezhik and Fallick, 1996, respectively). Kump et al. (2011) have compared the $\delta^{13}\text{C}_{\text{carb}}$ negative excursion in the Zaonega Formation to that in the Franceville section in Gabon. However, Weber and Gauthier-Lafaye (2013) argued that there is no real negative $\delta^{13}\text{C}_{\text{carb}}$ excursion recorded in the Franceville Basin. The termination of LJE in the Franceville Basins is still uncertain and requires further research. Meanwhile, Bekker et al. (2016) have described heavy carbonates in the 2.03 Ga Woolly dolomite in Australia, with $\delta^{13}\text{C}_{\text{carb}}$ values up to 8.4‰ 30 Ma after the nominal end of LJE.

Confirming what has been found in earlier studies (e.g., Črne et al., 2014; Melezhik et al., 2015), this study has found a negative excursion following the LJE in the Upper Zaonega Formation. However, the magnitude of this negative excursion, as recorded in the Upper Zaonega Formation, has not been identified in other post-LJE successions. It is possibly related to the carbonate precipitation influenced by the anaerobic oxidation of methane at the submarine methane seeps (Kreitsmann et al., submitted – PAPER IV). This suggests that the negative excursion in the Onega Basin results from basin-specific processes, meaning it cannot be used to infer the isotopic composition of the global seawater DIC pool. Nevertheless, the emerging picture seems to suggest that the termination of LJE was followed by several small-scale fluctuations in the global carbon cycle, before achieving relative stability in late Paleoproterozoic and Mesoproterozoic (Brasier and Lindsay, 1998).

5.6. Marine REY_{SN} signal in the Zaonega Formation and the Pilgujärvi Sedimentary Formation

Measurements of the lanthanides and yttrium from geochemical precipitates (e.g., cherts, phosphates, carbonates) are known to be a proxy for ancient seawater compositions and redox states (e.g., Alexander et al., 2008; Allwood et al., 2010; Bau and Alexander, 2006; Bellefroid et al., 2019; Kamber et al., 2014; Kamber and Webb, 2001; Shields and Stille, 2001). In modern seawater the REY_{SN} signal is largely dominated by the products of continental weathering and aeolian dust. Input by the hydrothermal activity on the ocean floor is insignificant, but it was possibly more pronounced during the Archean, as is evidenced from the widespread positive Eu_{SN} anomalies in the Archean chemical sediments (Alexander et al., 2009; Bau and Dulski, 1996; Viehmann et al., 2015).

The typical seawater REY_{SN} pattern is characterized by the depletion of LREE and the progressive enrichment of HREE (Elderfield et al., 1988), the positive La_{SN}, Gd_{SN} and possibly Lu_{SN} anomalies (Bau and Dulski, 1999; Bolhar et al., 2004; Tostevin et al., 2016), a super-chondritic Y/Ho ratio (>44; Bau et al., 1995; Nozaki et al., 1997) and a negative Ce_{SN} anomaly in modern oceans (Bau and Koschinsky, 2009). The screened OnZap carbonate samples show strong LREE depletion, expressed as the (Pr/Yb)_{SN} ratio (Bolhar et al., 2004), ranging from 0.09 to 0.60, positive La_{SN} anomalies varying from 1.16 to 1.56 and positive Gd_{SN} anomalies varying from 1.31 to 1.35 in Unit B. The Y/Ho ratios become super-chondritic in open-marine settings, whereas in restricted environments and/or those with freshwater influence the Y/Ho ratio is <44 (Bolhar and Van Kranendonk, 2007; Kamber and Webb, 2001; Nozaki et al., 1997). The Y/Ho ratios of the screened carbonate samples in Unit B range from 32.98 to 49.63, whereas they are lower in Units A and C, 30.02 and 33.07, respectively. Thus, depleted LREE concentrations compared to HREE, positive La_{SN} and Gd_{SN} anomalies, nearly super-chondritic Y/Ho ratios and uniform but variable REY_{SN} data all suggest that the carbonate samples from Unit B carry the REY_{SN} distribution of ambient seawater. This conclusion is also supported by the carbon isotopes, which carry near-normal marine $\delta^{13}\text{C}_{\text{carb}}$ values in Unit B. The lower Y/Ho ratios in Units A and C can be explained by the hydrothermal processes, which also agree with the C- and S-isotope interpretations and detailed petrographic and geochemical characterization (Kreitsmann et al., 2019 – PAPER I; Paiste et al., 2018 – PAPER II; Kreitsmann et al., submitted – PAPER IV; Črne et al., 2014).

These results agree well with the REY composition of sedimentary apatite of the Upper Zaonega Formation from the outcrop section near the Shunga village studied by Joosu et al. (2015). This c. 13 m high outcrop consists of a 5 m thick succession of organic-rich mudstones that contains two dolostone beds in the lower part as well as alternating silica veins and dolostone in the upper part. The level exposed in the Shunga outcrop can be correlated with the organic-rich mudstone interval below the prominent dolostone horizon of Unit B1 in the

OnZap section (see Fig. 4). The average Y/Ho ratios are around 40 in the diagenetic apatites in the lower mudstones and dolostone units, but drop to c. 30 in the upper mudstone unit exposed at the Shunga outcrop (Joosu et al., 2015), possibly suggesting varying intensity in hydrothermal input.

In the Pilgijärvi SF, both type D phosphatic grains and apatite cement samples carry the seawater signal, although with small differences. In type D grains, the apatite REY_{SN} pattern is relatively flat with BSI ranging from 1.1 to 1.34 and weak LREE depletion compared to HREE expressed as (Pr/Yb)_{SN} ratios ranging between 0.53 and 0.85 (Fig. 10A). Apatite cement does not show LREE depletion and it is more MREE enriched, with BSI ranging from 1.27 to 1.57 (Fig. 10B). Both type D grains and apatite cement carry a marine Y/Ho signal with the average ratios of 43.7 ± 3 . Typically, MREE enrichment in apatite is associated with late diagenesis and/or hydrothermal recrystallization (Morad and Felitsyn, 2001). However, MREE enrichment in apatite can be also a primary feature if apatite was precipitated in an environment where Fe(Mn)-oxyhydroxide redox-pumping occurred (Haley et al., 2004; Jarvis, 1994). Interestingly, with the total REE concentration increasing, typical seawater features become less pronounced (e.g., samples with the highest REE concentration have the lowest Y/Ho ratio and the highest BSI). This is in an agreement with REE systematics in modern apatite grains forming on the Namibian coast, suggesting that apatite scavenges most of the REE from pore water during diagenesis (Lumiste et al., 2019). Hence, apatite loses typical seawater features with progressing diagenesis, meaning that the pattern closest to seawater is preserved in the samples with the lowest total REE.

5.6.1 Eu_{SN} anomalies in the Zaonega and Pilgijärvi Sedimentary Formations

Europium can be decoupled from the other trivalent REE in high-temperature hydrothermal fluids (>250 °C) where Eu³⁺ is reduced to Eu²⁺. The latter has a strong affinity to Cl⁻ complexation, whereas Eu³⁺ behaves similarly to other trivalent REE (Bau, 1991; Douville et al., 1999). Positive Eu_{SN} anomaly is common in the Archean carbonates (Allwood et al., 2010; Kamber and Webb, 2001; Schier et al., 2018), indicating an important input of REY from the hydrothermal solutions of deep oceans during the Archean. However, positive Eu_{SN} anomaly is rare in Proterozoic marine carbonates (Bau and Alexander, 2006; Schier et al., 2018; Wang et al., 2018), suggesting that the influence of high-temperature hydrothermal input as a source of REE is diminishing. There is a prominent positive Eu_{SN} anomaly, both in the carbonates and sedimentary apatite from the Zaonega Formation (Kreitsmann et al., submitted – PAPER IV; Joosu et al., 2015), but also in the apatite from the Pilgijärvi SF (Joosu et al., 2016 – PAPER III). In the screened carbonate and apatite samples from the Zaonega Formation, Eu_{SN} anomalies range between 1.24 and 2.26 and 0.7 to nearly 4, respectively, while in the Pilgijärvi SF apatite ranges between 1.23 and 3.98 (Joosu et al., 2016 – PAPER III; Kreitsmann et al., submitted – PAPER IV; Joosu

et al., 2015; Kreitsmann et al., 2016). A positive Eu_{SN} anomaly can also be an analytical artefact due to the overlap of BaO and Eu peaks in the ICP-MS analyses. However, there is no correlation between the measured Eu and Ba concentrations in the studied samples, and Ba/Eu ratios are low. It is noteworthy that the negative Ce_{SN} anomalies and well-preserved C isotopes of the screened carbonate samples eliminate the possibility that the REY data from the Zaonega Formation are due to postdepositional overprinting. The occurrence of positive Eu_{SN} anomaly agrees with the geological context of the Zaonega Formation and the Pilgijärvi SF being marked by significant syn-depositional volcanic activity (e.g., Črne et al., 2014; Hanski et al., 2014). Thus, the preservation of a prominent Eu_{SN} anomaly implies that these basins had to be semi-restricted, rather than being in fully open marine settings, because the excess Eu would have been diluted rapidly in the latter case. Varying Eu_{SN} anomaly values would therefore indicate a different distance from the venting sites or a difference in magmatic activity during the apatite and carbonate precipitation.

5.6.2 Ce_{SN} anomalies in the Zaonega and Pilgijärvi Sedimentary Formations

The redox status of seawater during the formation of modern and ancient carbonates and phosphates has been widely assessed by using Ce behavior (Bellefroid et al., 2018; Liu et al., 2019; Tostevin et al., 2016; Webb and Kamber, 2000). In modern oxygenated seawater, dissolved Ce^{3+} is oxidized to a more particle reactive Ce^{4+} oxide on the surface of Fe-Mn-(hydr)oxides and it is removed from seawater by the deposition of particulated/colloidal material (Bau and Koschinsky, 2009). As a result, modern seawater has a distinct negative Ce_{SN} anomaly. However, the Ce_{SN} anomaly does not necessarily describe the redox condition of the water column at the depositional site. Negative Ce_{SN} anomalies can already develop during oxidative weathering and subsequent riverine transport (Byrne and Liu, 1998; Merschel et al., 2017), producing Ce-depleted continental run-off waters and eventually a negative Ce_{SN} anomaly in seawater (Goldstein and Jacobsen, 1988). In addition, it must be considered that the Ce_{SN} anomaly cannot be used as an unambiguous environmental proxy because of the potential influence from the anomalous behavior of La in seawater (Bau and Dulski, 1996). Only the negative Ce_{SN} anomalies without anomalous La influence, as assessed by $(\text{Pr}/\text{Pr}^*)_{\text{SN}}$ ratio (criterion >1.05), can be considered true negative anomalies (Fig. 14; Bau and Dulski, 1996; Kamber and Webb, 2001). In that regard, the screened carbonate samples from Unit B of the Zaonega Formation show negative Ce_{SN} anomalies with $(\text{Pr}/\text{Pr}^*)_{\text{SN}}$ ratios ranging between 1.06–1.36, whereas Units A and C do not record true Ce_{SN} anomalies (Fig. 14). The real negative Ce_{SN} anomaly in the OnZap carbonates is further strengthened by a persistently negative Ce_{SN} anomaly of similar amplitude in the diagenetic apatite from the organic-rich mudstone-dolostone interval in the Shunga outcrop (Fig. 14; Joosu et al., 2015). The Ce_{SN} anomalies reported in the best-preserved

diagenetic apatite (DiaAP *sensu* Joosu et al., 2015) show $(\text{Pr}/\text{Pr}^*)_{\text{SN}}$ ratios consistently ranging between 1.0–1.25 throughout the Shunga outcrop interval. This agrees with carbonate data, indicating that the sedimentary basin water column was at least partially oxygenated, allowing for Ce oxidation and its subsequent removal (Fig 14; Joosu et al., 2015).

In the Pilgijärvi SF most of the type D apatite grains show a real negative Ce_{SN} anomaly, although apatite cement does not exhibit anomalous Ce behavior (Fig. 14). This suggests varying redox conditions in the Pechenga Basin. It is also important to note that the Pilgijärvi SF was deposited in a submarine slope setting. The apatite cement in siltstones represents a deeper facies setting than the gritstones carrying type D phosphatic grains with a negative Ce_{SN} anomaly. Hence, it seems that shore waters were oxygenated, while anoxic conditions prevailed in deep waters. Similar results have been reported from the 1.88 Ga Gunflint Formation in the Animikie Basin, where negative Ce_{SN} anomalies have been described in inner shelf carbonates, whereas deep ocean remained reducing (Fralick et al., 2017).

From the wealth of geochemical data that has been generated from the Zaonega rocks as well as from other post-LJE successions (e.g., Pilgijärvi SF and Gunflint Formation), it can be argued that oxygen levels were fluctuating following the LJE, but that they were sufficiently high to allow for Ce oxidation. Anoxic conditions could have prevailed in deeper waters, while shallower waters remained oxic. Large et al. (2019) has recently suggested that the mean atmospheric oxygen concentration stayed as high as c. 7 wt.% during the Proterozoic. Signs of elevated oxygen concentrations have been also found in the 1.85 Ga Stambaugh Formation (Planavsky et al., 2018) and possibly from the ~1.4 Ga Xiamaling Formation (Diamond et al., 2018), arguing against the unidirectional sharp drop in oxygen levels after the LJE.

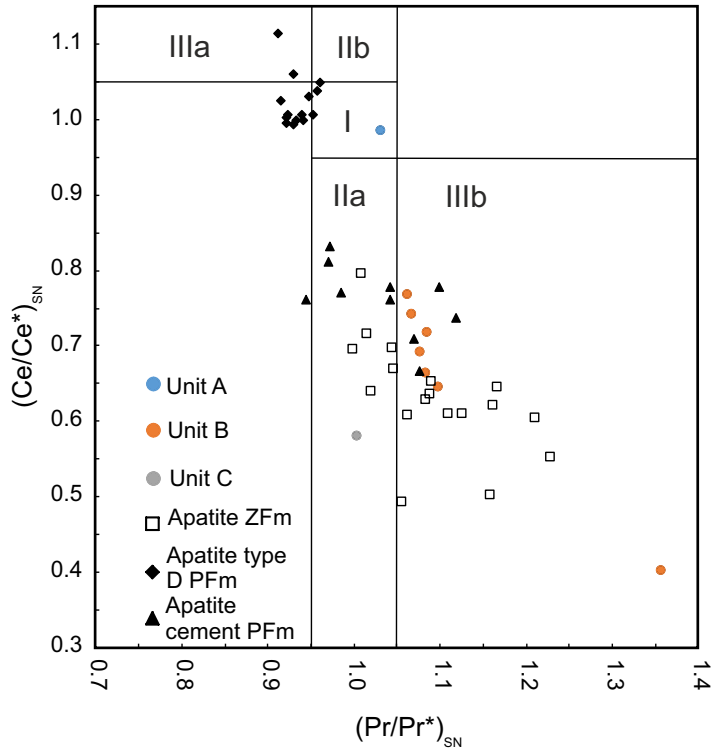


Figure 14. Plot of PAAS-normalized Ce/Ce^* [$Ce/(0.5La + 0.5Pr)_{SN}$] vs Pr/Pr^* [$Pr/(0.5Ce + 0.5Nd)_{SN}$] evaluating Ce_{SN} anomaly (after Bau and Dulski, 1996) in the screened OnZap samples (Kreitsmann et al., submitted – PAPER IV), diagenetic apatite data from Joosu et al. (2015) taken from the Shunga village outcrop that corresponds to B1 in the OnZap section and type D phosphatic grains (Joosu et al., 2015 – PAPER III) and apatite cement (Kreitsmann et al., 2016) from the Pilgujärvi SF. (I) no anomalous behavior; (IIa) positive La_{SN} anomaly, no Ce_{SN} anomaly; (IIb) negative La_{SN} anomaly, no Ce_{SN} anomaly; (IIIa) positive Ce_{SN} anomaly; (IIIb) real negative Ce_{SN} anomaly. All of the screened samples from Unit B display negative Ce_{SN} anomalies, whereas the sample from Unit A plots in a positive La_{SN} anomaly field and the sample from Unit C shows no anomalous behavior. Apatite REE data from the Shunga village displays similar but a more varying pattern. Apatite cement does not show anomalous behavior, whereas some of the type D grains have a real negative Ce_{SN} anomaly.

6. CONCLUSIONS

This thesis focused on the paleoenvironmental signatures held in two post-LJE successions in Northwestern Russia – the 1.98 Ga Zaonega Formation and the 1.92 Ga Pilgijärvi Sedimentary Formation in Onega and Pechenga Basins. The aim of this thesis was to use the carbon isotope composition and rare earth elements and yttrium (REY) characteristics, to assess the post-LJE carbon cycle, environmental settings and oxygen levels in the atmosphere-ocean system. In order to evaluate the global significance of the trends observed in the Zaonega Formation, REY analyses were also carried out in the sedimentary apatite samples from the 60 Ma younger Pilgijärvi SF. The main findings of this thesis are:

- 1) The carbonate sedimentary units in the Upper Zaonega Formation have experienced varying degrees of secondary alteration – the outer edges of carbonate beds are generally dedolomitized, whereas the dolomitic bed interiors largely preserve primary geochemical signal.
- 2) The screened samples from the two studied sections intersecting the Upper Zaonega Formation (OnZap and OPH) show an upward increasing $\delta^{13}\text{C}_{\text{carb}}$ trend from -8.5‰ to 0.8‰ .
- 3) The marine DIC pool in the Onega Basin was influenced by methanotrophic processes during the Zaonega times, as exemplified by the possibly methane-derived carbonates and variable primary $\delta^{13}\text{C}_{\text{carb}}$ values.
- 4) In the Upper Zaonega Formation, the most pristine and possibly open marine signal is preserved in the basin-scale massive dolostone horizon (Unit B in the OnZap section and the dolostone beds A and B in the OPH core), as represented by the near 0‰ $\delta^{13}\text{C}_{\text{carb}}$ values, super-chondritic Y/Ho ratios, a depleted LREE compared to HREE REY_{SN} pattern and positive La_{SN} and Gd_{SN} anomalies.
- 5) Sedimentary apatites in the Pilgijärvi Sedimentary Formation in the Pechenga Basin and carbonates (and apatites) in the Zaonega Formation in the Onega Basin have prominent positive Eu_{SN} anomalies, suggesting a strong high-temperature hydrothermal influence to respective basins.
- 6) Negative Ce_{SN} anomalies in the c. 1.98 Ga Zaonega Formation in the Onega Basin and in the 1.92 Ga Pilgijärvi Sedimentary Formation in the Pechenga Basin argue for fluctuating but elevated oxygen levels in the atmosphere-ocean system, which were enough to decouple Ce from the other rare earth elements.

The complex depositional history and occasional severe postdepositional alteration of the Zaonega Formation sediments highlight the need for thorough petrological and mineralogical screening prior to the interpretation of geochemical data. Moreover, it is important to identify possible basin-specific processes that, if left unrecognized, would result in erroneous conclusions when the observed

geochemical patterns are extended to describe the open ocean. Rare earth elements systematics from the Zaonega Formation and the Pilgijärvi Sedimentary Formation as well as the stable carbon isotope record from other post-LJE successions suggest times of instability in the global carbon cycle and fluctuating but elevated O₂ levels persisting after the LJE. Thus, models regarding the Earth system redox states which use data contained in the Zaonega Formation and the Pilgijärvi Sedimentary Formation, to infer a global collapse of oxygen levels at this time, are equivocal. Additional REY work in other post-LJE sections is necessary to better constrain the global redox evolution following the LJE.

REFERENCES

- Al-Aasm, I.S., Taylor, B.E., South, B., 1990. Stable isotope analysis of multiple carbonate samples using selective acid extraction. *Chem. Geol. Isot. Geosci. Sect.* 80, 119–125. [https://doi.org/10.1016/0168-9622\(90\)90020-D](https://doi.org/10.1016/0168-9622(90)90020-D)
- Alexander, B.W., Bau, M., Andersson, P., Dulski, P., 2008. Continentally-derived solutes in shallow Archean seawater: Rare earth element and Nd isotope evidence in iron formation from the 2.9Ga Pongola Supergroup, South Africa. *Geochim. Cosmochim. Acta* 72, 378–394. <https://doi.org/10.1016/j.gca.2007.10.028>
- Alexander, B.W., Bau, M., Andersson, P., 2009. Neodymium isotopes in Archean seawater and implications for the marine Nd cycle in Earth's early oceans. *Earth Planet. Sci. Lett.* 283, 144–155. <https://doi.org/10.1016/j.epsl.2009.04.004>
- Allwood, A.C., Kamber, B.S., Walter, M.R., Burch, I.W., Kanik, I., 2010. Trace elements record depositional history of an Early Archean stromatolitic carbonate platform. *Chem. Geol.* 270, 148–163. <https://doi.org/10.1016/j.chemgeo.2009.11.013>
- Anbar, A.D., Duan, Y., Lyons, T.W., Arnold, G.L., Kendall, B., Creaser, R.A., Kaufman, A.J., Gordon, G.W., Scott, C., Garvin, J., Buick, R., 2007. A Whiff of Oxygen Before the Great Oxidation Event? *Science* 317, 1903–1906. <https://doi.org/10.1126/science.1140325>
- Asael, D., Tissot, F.L.H., Reinhard, C.T., Rouxel, O., Dauphas, N., Lyons, T.W., Ponzevera, E., Liorzou, C., Chéron, S., 2013. Coupled molybdenum, iron and uranium stable isotopes as oceanic paleoredox proxies during the Paleoproterozoic Shunga Event. *Chem. Geol.*, 362, 193–210. <https://doi.org/10.1016/j.chemgeo.2013.08.003>
- Asael, D., Rouxel, O., Poulton, S.W., Lyons, T.W., Bekker, A., 2018. Molybdenum record from black shales indicates oscillating atmospheric oxygen levels in the early Paleoproterozoic. *Am. J. Sci.* 318, 275–299. <https://doi.org/10.2475/03.2018.01>
- Ayora, C., Taberner, C., Saaltink, M.W., Carrera, J., 1998. The genesis of dedolomites: a discussion based on reactive transport modeling. *J. Hydrol.* 209, 346–365. [https://doi.org/10.1016/S0022-1694\(98\)00095-X](https://doi.org/10.1016/S0022-1694(98)00095-X)
- Banner, J.L., Hanson, G.N., Meyers, W.J., 1988. Rare earth element and Nd isotopic variations in regionally extensive dolomites from the Burlington-Keokuk Formation (Mississippian): implications for REE mobility during carbonate diagenesis. *J. Sediment. Petrol.* 58, 415–432. <https://doi.org/10.1306/212F8DAA-2B24-11D7-8648000102C1865D>
- Banner, J.L., Hanson, G.N., 1990. Calculation of simultaneous isotopic and trace element variations during water-rock interaction with applications to carbonate diagenesis. *Geochim. Cosmochim. Acta* 54, 3123–3137. [https://doi.org/10.1016/0016-7037\(90\)90128-8](https://doi.org/10.1016/0016-7037(90)90128-8)
- Banner, J.L., 1995. Application of the trace element and isotope geochemistry of strontium to studies of carbonate diagenesis. *Sedimentology* 42, 805–824. <https://doi.org/10.1111/j.1365-3091.1995.tb00410.x>
- Bau, M., 1991. Rare-earth element mobility during hydrothermal and metamorphic fluid-rock interaction and the significance of the oxidation state of europium. *Chem. Geol.* 93, 219–230. [https://doi.org/10.1016/0009-2541\(91\)90115-8](https://doi.org/10.1016/0009-2541(91)90115-8)
- Bau, M., Möller, P., 1992. Rare earth element fractionation in metamorphogenic hydrothermal calcite, magnesite and siderite. *Mineral. Petrol.* 45, 231–246. <https://doi.org/10.1007/BF01163114>
- Bau, M., 1993. Effects of syn- and post-depositional processes on the rare-earth element distribution in Precambrian iron-formations. *Eur. J. Mineral.* 5, 257–267.

- Bau, M., Dulski, P., Moeller, P., 1995. Yttrium and holmium in South Pacific seawater: vertical distribution and possible fractionation mechanisms. *Chem. Erde – Geochem.* 55, 1–15.
- Bau, M., Dulski, P., 1996. Distribution of yttrium and rare-earth elements in the Penge and Kuruman iron-formations, Transvaal Supergroup, South Africa. *Precambrian Res.*, 79, 37–55. [https://doi.org/10.1016/0301-9268\(95\)00087-9](https://doi.org/10.1016/0301-9268(95)00087-9)
- Bau, M., Koschinsky, A., Dulski, P., Hein, J.R., 1996. Comparison of the partitioning behaviours of yttrium, rare earth elements, and titanium between hydrogenetic marine ferromanganese crusts and seawater. *Geochim. Cosmochim. Acta* 60, 1709–1725. [https://doi.org/10.1016/0016-7037\(96\)00063-4](https://doi.org/10.1016/0016-7037(96)00063-4)
- Bau, M., Dulski, P., 1999. Comparing Yttrium and rare earths in hydrothermal fluids from the Mid-Atlantic Ridge: implications for Y and REE behavior during near-vent mixing and for the Y/Ho ratio of Proterozoic seawater. *Chem. Geol.* 155, 77–90
- Bau, M., Alexander, B., 2006. Preservation of primary REE patterns without Ce anomaly during dolomitization of Mid-Paleoproterozoic limestone and the potential re-establishment of marine anoxia immediately after the “Great Oxidation Event.” *South Afr. J. Geol.* 109, 81–86. <https://doi.org/10.2113/gssajg.109.1-2.81>
- Bau, M., Koschinsky, A., 2009. Oxidative scavenging of cerium on hydrous Fe oxide: Evidence from the distribution of rare earth elements and yttrium between Fe oxides and Mn oxides in hydrogenetic ferromanganese crusts. *Geochem. J.* 43, 37–47. <https://doi.org/10.2343/geochemj.1.0005>
- Bekker, A., Holland, H.D., Wang, P.-L., Rumble, I., Stein, H.J., Hannah, J.L., Coetzee, L.L., Beukes, N.J., 2004. Dating the rise of atmospheric oxygen. *Nature* 427, 117–120. <https://doi.org/10.1038/nature02260>
- Bekker, A., Kaufman, A.J., Karhu, J.A., Eriksson, K.A., 2005. Evidence for Paleoproterozoic cap carbonates in North America. *Precambrian Res., Stable Isotopes, Life and Early Earth History* 137, 167–206. <https://doi.org/10.1016/j.precamres.2005.03.009>
- Bekker, A., Holland, H.D., 2012. Oxygen overshoot and recovery during the early Paleoproterozoic. *Earth Planet. Sci. Lett.* 317–318, 295–304. <https://doi.org/10.1016/j.epsl.2011.12.012>
- Bekker, A., Krapež, B., Müller, S.G., Karhu, J.A., 2016. A short-term, post-Lomagundi positive C isotope excursion at c. 2.03 Ga recorded by the Woolly Dolomite, Western Australia. *J. Geol. Soc.* 173, 689–700. <https://doi.org/10.1144/jgs2015-152>
- Bellefroid, E.J., Hood, A. v S., Hoffman, P.F., Thomas, M.D., Reinhard, C.T., Planavsky, N.J., 2018. Constraints on Paleoproterozoic atmospheric oxygen levels. *Proc. Natl. Acad. Sci.* 201806216. <https://doi.org/10.1073/pnas.1806216115>
- Bellefroid, E.J., Planavsky, N.J., Hood, A.V.S., Halverson, G.P., Spokas, K., 2019. Shallow water redox conditions of the mid-Proterozoic Muskwa Assemblage, British Columbia, Canada. *Am. J. Sci.* 319, 122–157. <https://doi.org/10.2475/02.2019.03>
- Bishop, J.W., Osleger, D.A., Montañez, I.P., Sumner, D.Y., 2014. Meteoric diagenesis and fluid-rock interaction in the Middle Permian Capitan backreef: Yates Formation, Slaughter Canyon, New Mexico. *AAPG Bull.* 98, 1495–1519. <https://doi.org/10.1306/05201311158>
- Blättler, C.L., Claire, M.W., Prave, A.R., Kirsimäe, K., Higgins, J.A., Medvedev, P.V., Romashkin, A.E., Rychanchik, D.V., Zerkle, A.L., Paiste, K., Kreitsmann, T., Millar, I.L., Hayles, J.A., Bao, H., Turchyn, A.V., Warke, M.R., Lepland, A., 2018. Two-billion-year-old evaporites capture Earth’s great oxidation. *Science* 360, 320–323. <https://doi.org/10.1126/science.aar2687>

- Boetius, A., Ravensschlag, K., Schubert, C.J., Rickert, D., Widdel, F., Gieseke, A., Amann, R., Jørgensen, B.B., Witte, U., Pfannkuche, O., 2000. A marine microbial consortium apparently mediating anaerobic oxidation of methane. *Nature* 407, 623–626. <https://doi.org/10.1038/35036572>
- Bolea-Fernandez, E., Balcaen, L., Resano, M., Vanhaecke, F., 2015. Tandem ICP-mass spectrometry for Sr isotopic analysis without prior Rb/Sr separation. *J. Anal. At. Spectrom.* 31, 303–310. <https://doi.org/10.1039/C5JA00157A>
- Bolhar, R., Kamber, B.S., Moorbath, S., Fedo, C.M., Whitehouse, M.J., 2004. Characterisation of early Archaean chemical sediments by trace element signatures. *Earth Planet. Sci. Lett.* 222, 43–60. <https://doi.org/10.1016/j.epsl.2004.02.016>
- Bolhar, R., Van Kranendonk, M.J., 2007. A non-marine depositional setting for the northern Fortescue Group, Pilbara Craton, inferred from trace element geochemistry of stromatolitic carbonates. *Precambrian Res.* 155, 229–250. <https://doi.org/10.1016/j.precamres.2007.02.002>
- Brand, U., Veizer, J., 1980. Chemical diagenesis of a multicomponent carbonate system – I. Trace elements. *J. Sediment. Petrol.* 50, 1219–1236. <https://doi.org/10.1306/212F7BB7-2B24-11D7-8648000102C1865D>
- Brasier, M.D., Lindsay, J.F., 1998. A billion years of environmental stability and the emergence of eukaryotes: New data from northern Australia. *Geology* 26, 555–558. [https://doi.org/10.1130/0091-7613\(1998\)026<0555:ABYOES>2.3.CO;2](https://doi.org/10.1130/0091-7613(1998)026<0555:ABYOES>2.3.CO;2)
- Brasier, A.T., Fallick, A.E., Prave, A.R., Melezhik, V.A., Lepland, A., 2011. Coastal sabkha dolomites and calcitised sulphates preserving the Lomagundi-Jatuli carbon isotope signal. *Precambrian Res.* 189, 193–211. <https://doi.org/10.1016/j.precamres.2011.05.011>
- Budai, J.M., Lohmann, K.C., Owen, R.M., 1984. Burial dedolomite in the Mississippian Madison Limestone, Wyoming and Utah thrust belt. *J. Sediment. Res.* 54, 276–288. <https://doi.org/10.1306/212F83FF-2B24-11D7-8648000102C1865D>
- Budai, J.M., Martini, A.M., Walter, L.M., Ku, T.C.W., 2002. Fracture-fill calcite as a record of microbial methanogenesis and fluid migration: a case study from the Devonian Antrim Shale, Michigan Basin. *Geofluids* 2, 163–183. <https://doi.org/10.1046/j.1468-8123.2002.00036.x>
- Byrne, R.H., Liu, X., 1998. A Coupled Riverine-Marine Fractionation Model for Dissolved Rare Earths and Yttrium. *Aquat. Geochem.* 4, 103–121. <https://doi.org/10.1023/A:1009651919911>
- Campbell, K.A., 2006. Hydrocarbon seep and hydrothermal vent paleoenvironments and paleontology: Past developments and future research directions. *Palaeogeogr. Palaeoclimatol. Palaeoecol.* 232, 362–407. <https://doi.org/10.1016/j.palaeo.2005.06.018>
- Canfield, D.E., Ngombi-Pemba, L., Hammarlund, E.U., Bengtson, S., Chaussidon, M., Gauthier-Lafaye, F., Meunier, A., Riboulleau, A., Rollion-Bard, C., Rouxel, O., Asael, D., Pierson-Wickmann, A.-C., Albani, A.E., 2013. Oxygen dynamics in the aftermath of the Great Oxidation of Earth's atmosphere. *Proc. Natl. Acad. Sci.* 110, 16736–16741. <https://doi.org/10.1073/pnas.1315570110>
- Castellini, D.G., Dickens, G.R., Snyder, G.T., Ruppel, C.D., 2006. Barium cycling in shallow sediment above active mud volcanoes in the Gulf of Mexico. *Chem. Geol.* 226, 1–30. <https://doi.org/10.1016/j.chemgeo.2005.08.008>

- Cheng, P., Koyanagi, G.K., Bohme, D.K., 2008. On the chemical resolution of the 87Rb^+ (s_0)/ 87Sr^+ (s_1) isobaric interference: A kinetic search for an optimum reagent. *Anal. Chim. Acta, Mass Spectrometry* 627, 148–153.
<https://doi.org/10.1016/j.aca.2008.03.057>
- Črne, A.E., Melezhik, V.A., Prave, A.R., Lepland, A., Romashkin, A.E., Rychanchik, D.V., Hanski, E.J., Luo, Z., 2013. Zaonega formation: FAR-DEEP hole 13A. In: Melezhik, V.A., Prave, A.R., Fallick, A.E., Hanski, E.J., Lepland, A., Kump, L.R., Strauss, H. (Eds), *Reading the Archive of Earth's Oxygenation: Volume 2: The Core Archive of the Fennoscandian Arctic Russia – Drilling Early Earth Project*. Springer, pp. 1008-1046. https://doi.org/10.1007/978-3-642-29659-8_4
- Črne, A.E., Melezhik, V.A., Lepland, A., Fallick, A.E., Prave, A.R., Brasier, A.T., 2014. Petrography and geochemistry of carbonate rocks of the Paleoproterozoic Zaonega Formation, Russia: Documentation of ^{13}C -depleted non-primary calcite. *Precambrian Res.* 240, 79–93. <https://doi.org/10.1016/j.precamres.2013.10.005>
- De Baar, H.J.W., Bacon, M.P., Brewer, P.G., Bruland, K.W., 1985. Rare earth elements in the Pacific and Atlantic Oceans. *Geochim. Cosmochim. Acta* 49, 1943–1959. [https://doi.org/10.1016/0016-7037\(85\)90089-4](https://doi.org/10.1016/0016-7037(85)90089-4)
- De Baar, H.J.W., German, C.R., Elderfield, H., van Gaans, P., 1988. Rare earth element distributions in anoxic waters of the Cariaco Trench. *Geochim. Cosmochim. Acta* 52, 1203–1219. [https://doi.org/10.1016/0016-7037\(88\)90275-X](https://doi.org/10.1016/0016-7037(88)90275-X)
- Diamond, C.W., Planavsky, N.J., Wang, C., Lyons, T.W., 2018. What the 1.4 Ga Xiamaling Formation can and cannot tell us about the mid-Proterozoic ocean. *Geobiology* 16, 219–236. <https://doi.org/10.1111/gbi.12282>
- Douville, E., Bienvendu, P., Charlou, J.L., Donval, J.P., Fouquet, Y., Appriou, P., Gamo, T., 1999. Yttrium and rare earth elements in fluids from various deep-sea hydrothermal systems. *Geochim. Cosmochim. Acta* 63, 627–643.
[https://doi.org/10.1016/S0016-7037\(99\)00024-1](https://doi.org/10.1016/S0016-7037(99)00024-1)
- Elderfield H., Whitfield M., Burton J. D., Bacon M. P., Simon L. P., Charnock H, Lovelock J. E., 1988. The oceanic chemistry of the rare-earth elements. *Philos. Trans. R. Soc. Lond. Ser. Math. Phys. Sci.* 325, 105–126.
<https://doi.org/10.1098/rsta.1988.0046>
- Evans, D.A., Beukes, N.J., Kirschvink, J.L., 1997. Low-latitude glaciation in the Palaeoproterozoic era. *Nature* 386, 262. <https://doi.org/10.1038/386262a0>
- Farquhar, J., Bao, H., Thiemens, M., 2000. Atmospheric Influence on Earth's Earliest Sulfur Cycle. *Science* 289, 756–758. <https://doi.org/10.1126/science.289.5480.756>
- Faust, G.T., 1949. Dedolomitization, and its relation to a possible derivation of a magnesium-rich hydrothermal solution. *Am. Mineral.* 34, 789–823.
- Flügel, E., 2010. *Microfacies of Carbonate Rocks: Analysis, Interpretation and Application*, 2nd ed. Springer-Verlag, Berlin Heidelberg.
- Fralick, P., Planavsky, N., Burton, J., Jarvis, I., Addison, W.D., Barrett, T.J., Brumpton, G.R., 2017. Geochemistry of Paleoproterozoic Gunflint Formation carbonate: Implications for hydrosphere-atmosphere evolution. *Precambrian Res.* 290, 126–146. <https://doi.org/10.1016/j.precamres.2016.12.014>
- Freeman, K.H., Hayes, J.M., Trendel, J.-M., Albrecht, P., 1990. Evidence from carbon isotope measurements for diverse origins of sedimentary hydrocarbons. *Nature* 343, 254. <https://doi.org/10.1038/343254a0>
- Frimmel, H.E., 2009. Trace element distribution in Neoproterozoic carbonates as palaeoenvironmental indicator. *Chem. Geol.* 258, 338–353.
<https://doi.org/10.1016/j.chemgeo.2008.10.033>

- Geilert, S., Hensen, C., Schmidt, M., Liebetrau, V., Scholz, F., Doll, M., Deng, L., Fiskal, A., Lever, M.A., Su, C.-C., Schloemer, S., Sarkar, S., Thiel, V., Berndt, C., 2018. On the formation of hydrothermal vents and cold seeps in the Guaymas Basin, Gulf of California. *Biogeosciences* 15, 5715–5731. <https://doi.org/10.5194/bg-15-5715-2018>
- Goldstein, S.J., Jacobsen, S.B., 1988. Rare earth elements in river waters. *Earth Planet. Sci. Lett.* 89, 35–47. [https://doi.org/10.1016/0012-821X\(88\)90031-3](https://doi.org/10.1016/0012-821X(88)90031-3)
- Griffith, E.M., Paytan, A., 2012. Barite in the ocean – occurrence, geochemistry and palaeoceanographic applications. *Sedimentology* 59, 1817–1835. <https://doi.org/10.1111/j.1365-3091.2012.01327.x>
- Gromet, L.P., Haskin, L.A., Korotev, R.L., Dymek, R.F., 1984. The “North American shale composite”: Its compilation, major and trace element characteristics. *Geochim. Cosmochim. Acta* 48, 2469–2482. [https://doi.org/10.1016/0016-7037\(84\)90298-9](https://doi.org/10.1016/0016-7037(84)90298-9)
- Guo, Q., Strauss, H., Kaufman, A.J., Schröder, S., Gutzmer, J., Wing, B., Baker, M.A., Bekker, A., Jin, Q., Kim, S.-T., Farquhar, J., 2009. Reconstructing Earth’s surface oxidation across the Archean-Proterozoic transition. *Geology* 37, 399–402. <https://doi.org/10.1130/G25423A.1>
- Haley, B.A., Klinkhammer, G.P., McManus, J., 2004. Rare earth elements in pore waters of marine sediments. *Geochim. Cosmochim. Acta* 68, 1265–1279. <https://doi.org/10.1016/j.gca.2003.09.012>
- Hanski, E.J., Huhma, H., Melezhik, V.A., 2014. New isotopic and geochemical data from the Palaeoproterozoic Pechenga Greenstone Belt, NW Russia: Implication for basin development and duration of the volcanism. *Precambrian Res.* 245, 51–65. <https://doi.org/10.1016/j.precamres.2014.01.008>
- Himmler, T., Bach, W., Bohrmann, G., Peckmann, J., 2010. Rare earth elements in authigenic methane-seep carbonates as tracers for fluid composition during early diagenesis. *Chem. Geol.* 277, 126–136. <https://doi.org/10.1016/j.chemgeo.2010.07.015>
- Hodgskiss, M.S.W., Dagnaud, O.M.J., Frost, J.L., Halverson, G.P., Schmitz, M.D., Swanson-Hysell, N.L., Sperling, E.A., 2019. New insights on the Orosirian carbon cycle, early Cyanobacteria, and the assembly of Laurentia from the Paleoproterozoic Belcher Group. *Earth Planet. Sci. Lett.* 520, 141–152. <https://doi.org/10.1016/j.epsl.2019.05.023>
- Hoefs, J., 2008. *Stable Isotope Geochemistry*. Springer Science & Business Media.
- Hogmalm, K.J., Zack, T., Karlsson, A.K.-O., Sjöqvist, A.S.L., Garbe-Schönberg, D., 2017. In situ Rb–Sr and K–Ca dating by LA-ICP-MS/MS: an evaluation of N₂O and SF₆ as reaction gases. *J. Anal. At. Spectrom.* 32, 305–313. <https://doi.org/10.1039/C6JA00362A>
- Holland, H.D., 2002. Volcanic gases, black smokers, and the great oxidation event. *Geochim. Cosmochim. Acta* 66, 3811–3826. [https://doi.org/10.1016/S0016-7037\(02\)00950-X](https://doi.org/10.1016/S0016-7037(02)00950-X)
- Holland, H.D., 2006. The oxygenation of the atmosphere and oceans. *Philos. Trans. R. Soc. B Biol. Sci.* 361, 903–915. <https://doi.org/10.1098/rstb.2006.1838>
- Hood, A. v. S., Planavsky, N.J., Wallace, M.W., Wang, X., 2018. The effects of diagenesis on geochemical paleoredox proxies in sedimentary carbonates. *Geochim. Cosmochim. Acta* 232, 265–287. <https://doi.org/10.1016/j.gca.2018.04.022>
- Irwin, H., Curtis, C., Coleman, M., 1977. Isotopic evidence for source of diagenetic carbonates formed during burial of organic-rich sediments. *Nature* 269, 209. <https://doi.org/10.1038/269209a0>

- Jacobsen, S.B., Kaufman, A.J., 1999. The Sr, C and O isotopic evolution of Neoproterozoic seawater. *Chem. Geol.* 161, 37–57. [https://doi.org/10.1016/S0009-2541\(99\)00080-7](https://doi.org/10.1016/S0009-2541(99)00080-7)
- Jarvis, I., 1994. Phosphorite geochemistry: state-of-the-art and environmental concerns. *Eclogae Geol. Helvetiae* 87, 643–700.
- Johannesson, K.H., Hawkins, D.L., Cortés, A., 2006. Do Archean chemical sediments record ancient seawater rare earth element patterns? *Geochim. Cosmochim. Acta* 70, 871–890. <https://doi.org/10.1016/j.gca.2005.10.013>
- Joosu, L., Lepland, A., Kirsimäe, K., Romashkin, A.E., Roberts, N.M.W., Martin, A.P., Črne, A.E., 2015. The REE-composition and petrography of apatite in 2Ga Zaonega Formation, Russia: The environmental setting for phosphogenesis. *Chem. Geol.* 395, 88–107. <https://doi.org/10.1016/j.chemgeo.2014.11.013>
- Joosu, L., Lepland, A., Kreitsmann, T., Üpraus, K., Roberts, N.M.W., Paiste, P., Martin, A.P.; Kirsimäe, K. (2016). Petrography and the REE-composition of apatite in the Paleoproterozoic Pilgijärvi Sedimentary Formation, Pechenga Greenstone Belt, Russia. *Geochim. Cosmochim. Acta*, 186, 135–153. [10.1016/j.gca.2016.04.043](https://doi.org/10.1016/j.gca.2016.04.043).
- Joye, S.B., Bowles, M.W., Samarkin, V.A., Hunter, K.S., Niemann, H., 2010. Biogeochemical signatures and microbial activity of different cold-seep habitats along the Gulf of Mexico deep slope. *Deep Sea Res. Part II Top. Stud. Oceanogr., Gulf of Mexico Cold Seeps* 57, 1990–2001. <https://doi.org/10.1016/j.dsr2.2010.06.001>
- Kamber, B.S., Webb, G.E., 2001. The geochemistry of late Archaean microbial carbonate: implications for ocean chemistry and continental erosion history. *Geochim. Cosmochim. Acta* 65, 2509–2525. [https://doi.org/10.1016/S0016-7037\(01\)00613-5](https://doi.org/10.1016/S0016-7037(01)00613-5)
- Kamber, B.S., Webb, G.E., Gallagher, M., 2014. The rare earth element signal in Archaean microbial carbonate: information on ocean redox and biogenicity. *J. Geol. Soc.* 171, 745–763. <https://doi.org/10.1144/jgs2013-110>
- Karhu, J.A., 1993. Paleoproterozoic evolution of the carbon isotope ratios of sedimentary carbonates in the Fennoscandian Shield. *Geologian tutkimuskeskus*.
- Karhu, J.A., Holland, H.D., 1996. Carbon isotopes and the rise of atmospheric oxygen. *Geology* 24, 867–870. [https://doi.org/10.1130/0091-7613\(1996\)024<0867:CIATRO>2.3.CO;2](https://doi.org/10.1130/0091-7613(1996)024<0867:CIATRO>2.3.CO;2)
- Kasting, J.F., 2001. The Rise of Atmospheric Oxygen. *Science* 293, 819–820. <https://doi.org/10.1126/science.1063811>
- Kato, Y., Kano, T., Kunugiza, K., 2002. Negative Ce Anomaly in the Indian Banded Iron Formations: Evidence for the Emergence of Oxygenated Deep-Sea at 2.9-2.7 Ga. *Resour. Geol.* 52, 101–110. <https://doi.org/10.1111/j.1751-3928.2002.tb00123.x>
- Kaufman, A.J., Knoll, A.H., 1995. Neoproterozoic variations in the C-isotopic composition of seawater: stratigraphic and biogeochemical implications. *Precambrian Res.*, 73, 27–49. [https://doi.org/10.1016/0301-9268\(94\)00070-8](https://doi.org/10.1016/0301-9268(94)00070-8)
- Kipp, M.A., Stüeken, E.E., Bekker, A., Buick, R., 2017. Selenium isotopes record extensive marine suboxia during the Great Oxidation Event. *Proc. Natl. Acad. Sci.* 114, 875–880. <https://doi.org/10.1073/pnas.1615867114>
- Kreitsmann, T., Joosu L., Lepland A., Krupenik V.A., Üpraus K., Paiste P., Kirsimäe K., (2016) Environmental Settings of Apatite Precipitation in the Paleoproterozoic Pilgijärvi Sedimentary Formation. *Goldschmidt Abstracts*, 2016 1609
- Kreitsmann, T., Külaviir, M., Lepland, A., Paiste, K., Paiste, P., Prave, A.R., Sepp, H., Romashkin, A.E., Rychanchik, D.V., Kirsimäe, K., 2019. Hydrothermal dedolomitisation of carbonate rocks of the Paleoproterozoic Zaonega Formation, NW

- Russia – Implications for the preservation of primary C isotope signals. *Chem. Geol.* 512, 43–57. <https://doi.org/10.1016/j.chemgeo.2019.03.002>
- Kreitsmann, T.; Lepland, A.; Bau, M.; Prave, A.R.; Paiste, K.; Mänd, K.; Sepp, H.; Martma, T.; Romashkin, A.E.; Kirsimäe, K. Oxygenated conditions in the aftermath of the Lomagundi-Jatuli Event: carbon isotope and rare earth element signatures of the Paleoproterozoic Zaonega Formation, Russia. Manuscript submitted to *Precambrian Res.*
- Koistinen, T., Stephens, M.B., Bogatchev, V., Nordgulen, Ø., Wenneström, M., Korhonen, J., 2001. Geological Map of the Fennoscandian Shield. In: Scale 1:2,000,000. Norway and Sweden and the North-West Department of Natural Resources of Russia, Geological Surveys of Finland
- Krupenik, V.A., Akhmedov, A.M., Sveshnikova, K., 2011. Isotopic composition of carbon, oxygen and sulfur in the Ludicovian and Jatulian rocks. In: Glushanin, L.V., Sharov, N.V., Shchiptsov, V.V. (Eds.), *The Onega Paleoproterozoic Structure (Geology, Tectonics, Deep Structure, Minerageny)*. Institute of Geology, Karelian Research Centre RAS, Petrozavodsk, pp. 250–255 (in Russian).
- Kučera, J., Cempírek, J., Dolníček, Z., Muchez, P., Prochaska, W., 2009. Rare earth elements and yttrium geochemistry of dolomite from post-Variscan vein-type mineralization of the Nížký Jeseník and Upper Silesian Basins, Czech Republic. *J. Geochem. Explor.* 103, 69–79. <https://doi.org/10.1016/j.gexplo.2009.08.001>
- Kump, L.R., Junium, C., Arthur, M.A., Brasier, A., Fallick, A., Melezhik, V., Lepland, A., Črne, A.E., Luo, G., 2011. Isotopic Evidence for Massive Oxidation of Organic Matter Following the Great Oxidation Event. *Science* 334, 1694–1696. <https://doi.org/10.1126/science.1213999>
- Land, L.S., Prezbindowski, D.R., 1981. The origin and evolution of saline formation water, Lower Cretaceous carbonates, south-central Texas, U.S.A. *J. Hydrol., Symposium on Geochemistry of Groundwater* 54, 51–74. [https://doi.org/10.1016/0022-1694\(81\)90152-9](https://doi.org/10.1016/0022-1694(81)90152-9)
- Large, R.R., Mukherjee, I., Gregory, D., Steadman, J., Corkrey, R., Glushanin, L.V., 2019. Atmosphere oxygen cycling through the proterozoic and phanerozoic. *Miner. Deposita* 54, 485–506. <https://doi.org/10.1007/s00126-019-00873-9>
- Lawrence, M.G., Greig, A., Collerson, K.D., Kamber, B.S., 2006. Rare Earth Element and Yttrium Variability in South East Queensland Waterways. *Aquat. Geochem.* 12, 39–72. <https://doi.org/10.1007/s10498-005-4471-8>
- Lepland, A., Joosu, L., Kirsimäe, K., Prave, A.R., Romashkin, A.E., Črne, A.E., Martin, A.P., Fallick, A.E., Somelar, P., Üpraus, K., Mänd, K., Roberts, N.M.W., Van, Z., Wirth, R., Schreiber, A., 2014. Potential influence of sulphur bacteria on Palaeoproterozoic phosphogenesis. *Nat. Geosci.* 7, 20–24. <https://doi.org/10.1038/ngeo2005>
- Li, F., Webb, G.E., Algeo, T.J., Kershaw, S., Lu, C., Oehlert, A.M., Gong, Q., Pourmand, A., Tan, X., 2019. Modern carbonate ooids preserve ambient aqueous REE signatures. *Chem. Geol.* 509, 163–177. <https://doi.org/10.1016/j.chemgeo.2019.01.015>
- Liu, X.-M., Hardisty, D.S., Lyons, T.W., Swart, P.K., 2019. Evaluating the fidelity of the cerium paleoredox tracer during variable carbonate diagenesis on the Great Bahamas Bank. *Geochim. Cosmochim. Acta* 248, 25–42. <https://doi.org/10.1016/j.gca.2018.12.028>
- Lumiste, K., Mänd, K., Bailey, J., Paiste, P., Lang, L., Lepland, A., Kirsimäe, K., 2019. REE+Y uptake and diagenesis in Recent sedimentary apatites. *Chem. Geol.* 525, 268–281. <https://doi.org/10.1016/j.chemgeo.2019.07.034>

- Luo, G., Ono, S., Beukes, N.J., Wang, D.T., Xie, S., Summons, R.E., 2016. Rapid oxygenation of Earth's atmosphere 2.33 billion years ago. *Sci. Adv.* 2, e1600134. <https://doi.org/10.1126/sciadv.1600134>
- Lyons, T.W., Reinhard, C.T., Planavsky, N.J., 2014. The rise of oxygen in Earth's early ocean and atmosphere. *Nature* 506, 307. <https://doi.org/10.1038/nature13068>
- Mackensen, A., Schmiedl, G., 2019. Stable carbon isotopes in paleoceanography: Atmosphere, oceans, and sediments. *Earth-Sci. Rev.* 102893. <https://doi.org/10.1016/j.earscirev.2019.102893>
- Martin, Adam P., Condon, D.J., Prave, A.R., Lepland, A., 2013a. A review of temporal constraints for the Palaeoproterozoic large, positive carbonate carbon isotope excursion (the Lomagundi–Jatuli Event). *Earth-Sci. Rev.* 127, 242–261. <https://doi.org/10.1016/j.earscirev.2013.10.006>
- Martin, A. P., Condon, D.J., Prave, A.R., Melezhik, V.A., Lepland, A., Fallick, A.E., 2013b. Dating the termination of the Palaeoproterozoic Lomagundi–Jatuli carbon isotopic event in the North Transfennoscandian Greenstone Belt. *Precambrian Res.* 224, 160–168. <https://doi.org/10.1016/j.precamres.2012.09.010>
- Martin, A.P., Prave, A.R., Condon, D.J., Lepland, A., Fallick, A.E., Romashkin, A.E., Medvedev, P.V., Rychanchik, D.V., 2015. Multiple Palaeoproterozoic carbon burial episodes and excursions. *Earth Planet. Sci. Lett.* 424, 226–236. <https://doi.org/10.1016/j.epsl.2015.05.023>
- Matsumoto, R., Iijima, A., Katayama, T., 1988. Mixed-water and hydrothermal dolomitization of the Pliocene Shirahama Limestone, Izu Peninsula, central Japan. *Sedimentology* 35, 979–998. <https://doi.org/10.1111/j.1365-3091.1988.tb01741.x>
- Mazzullo, S.J., 2000. Organogenic Dolomitization in Peritidal to Deep-Sea Sediments. *J. Sediment. Res.* 70, 10–23. <https://doi.org/10.1306/2DC408F9-0E47-11D7-8643000102C1865D>
- McLennan, S.M., 1989. Rare earth elements in sedimentary rocks; influence of provenance and sedimentary processes. *Rev. Mineral. Geochem.* 21, 169–200.
- Melezhik, V.A., Fallick, A.E., 1996. A widespread positive $\delta^{13}\text{C}_{\text{carb}}$ anomaly at around 2.33–2.06 Ga on the Fennoscandian Shield: a paradox? *Terra Nova* 8, 141–157. <https://doi.org/10.1111/j.1365-3121.1996.tb00738.x>
- Melezhik, V.A., Fallick, A.E., Filippov, M.M., Larsen, O., 1999. Karelian shungite—an indication of 2.0-Ga-old metamorphosed oil-shale and generation of petroleum: geology, lithology and geochemistry. *Earth-Sci. Rev.* 47, 1–40. [https://doi.org/10.1016/S0012-8252\(99\)00027-6](https://doi.org/10.1016/S0012-8252(99)00027-6)
- Melezhik, V.A., Fallick, A.E., Rychanchik, D.V., Kuznetsov, A.B., 2005. Palaeoproterozoic evaporites in Fennoscandia: Implications for seawater sulphate, the rise of atmospheric oxygen and local amplification of the $\delta^{13}\text{C}$ excursion. *Terra Nova* 17, 141–148. <https://doi.org/10.1111/j.1365-3121.2005.00600.x>
- Melezhik, V.A., Huhma, H., Condon, D.J., Fallick, A.E., Whitehouse, M.J., 2007. Temporal constraints on the Paleoproterozoic Lomagundi–Jatuli carbon isotopic event. *Geology* 35, 655–658. <https://doi.org/10.1130/G23764A.1>
- Melezhik, V.A., Medvedev, P.V., Svetov, S.A., 2013. 4.3 The Onega Basin, in: Melezhik, Victor A., Prave, A.R., Fallick, A.E., Kump, L.R., Strauss, H., Lepland, A., Hanski, E.J. (Eds.), *Reading the Archive of Earth's Oxygenation: Volume 1: The Palaeoproterozoic of Fennoscandia as Context for the Fennoscandian Arctic Russia – Drilling Early Earth Project*. Springer, 387–490. https://doi.org/10.1007/978-3-642-29682-6_9

- Melezhik, V.A., Hanski, E.J., 2013. The pechenga greenstone belt, in: Melezhik, V.A., Prave, A.R., Fallick, A.E., Kump, L.R., Strauss, H., Lepland, A., Hanski, E.J. (Eds.), *Reading the Archive of Earth's Oxygenation: Volume 1: The Palaeoproterozoic of Fennoscandia as Context for the Fennoscandian Arctic Russia – Drilling Early Earth Project*. Springer, 289–385. https://doi.org/10.1007/978-3-642-29682-6_8
- Melezhik, V.A., Fallick, A.E., Brasier, A.T., Lepland, A., 2015. Carbonate deposition in the Palaeoproterozoic Onega basin from Fennoscandia: a spotlight on the transition from the Lomagundi-Jatuli to Shunga events. *Earth-Sci. Rev.* 147, 65–98. <https://doi.org/10.1016/j.earscirev.2015.05.005>
- Merschel, G., Bau, M., Schmidt, K., Münker, C., Dantas, E.L., 2017. Hafnium and neodymium isotopes and REY distribution in the truly dissolved, nanoparticulate/colloidal and suspended loads of rivers in the Amazon Basin, Brazil. *Geochim. Cosmochim. Acta* 213, 383–399. <https://doi.org/10.1016/j.gca.2017.07.006>
- Morad, S., Felitsyn, S., 2001. Identification of primary Ce-anomaly signatures in fossil biogenic apatite: implication for the Cambrian oceanic anoxia and phosphogenesis. *Sediment. Geol.* 143, 259–264. [https://doi.org/10.1016/S0037-0738\(01\)00093-8](https://doi.org/10.1016/S0037-0738(01)00093-8)
- Mänd, K., Robbins, L. J., Thoby, M., Paiste, K., Kreitsmann, T., Lalonde, S. V., Kirsimäe, K., Lepland, A., Konhäuser, K. O. Extreme trace metal enrichments in the Zaonega Formation indicate a post-Lomagundi O₂ overshoot. Manuscript submitted to *Nature Geoscience*.
- Nader, F.H., Swennen, R., Keppens, E., 2008. Calcitization/dedolomitization of Jurassic dolostones (Lebanon): results from petrographic and sequential geochemical analyses. *Sedimentology* 55, 1467–1485. <https://doi.org/10.1111/j.1365-3091.2008.00953.x>
- Nothdurft, L.D., Webb, G.E., Kamber, B.S., 2004. Rare earth element geochemistry of Late Devonian reefal carbonates, Canning Basin, Western Australia: confirmation of a seawater REE proxy in ancient limestones. *Geochim. Cosmochim. Acta* 68, 263–283. [https://doi.org/10.1016/S0016-7037\(03\)00422-8](https://doi.org/10.1016/S0016-7037(03)00422-8)
- Nozaki, Y., Zhang, J., Amakawa, H., 1997. The fractionation between Y and Ho in the marine environment. *Earth Planet. Sci. Lett.* 148, 329–340. [https://doi.org/10.1016/S0012-821X\(97\)00034-4](https://doi.org/10.1016/S0012-821X(97)00034-4)
- Och, L.M., Shields-Zhou, G.A., 2012. The Neoproterozoic oxygenation event: Environmental perturbations and biogeochemical cycling. *Earth-Sci. Rev.* 110, 26–57. <https://doi.org/10.1016/j.earscirev.2011.09.004>
- Orphan, V.J., House, C.H., Hinrichs, K.-U., McKeegan, K.D., DeLong, E.F., 2002. Multiple archaeal groups mediate methane oxidation in anoxic cold seep sediments. *Proc. Natl. Acad. Sci. U. S. A.* 99, 7663–7668. <https://doi.org/10.1073/pnas.072210299>
- Ossa Ossa, F., Eickmann, B., Hofmann, A., Planavsky, N.J., Asael, D., Pambo, F., Bekker, A., 2018. Two-step deoxygenation at the end of the Paleoproterozoic Lomagundi Event. *Earth Planet. Sci. Lett.* 486, 70–83. <https://doi.org/10.1016/j.epsl.2018.01.009>
- Paiste, K., Lepland, A., Zerkle, A.L., Kirsimäe, K., Izon, G., Patel, N.K., McLean, F., Kreitsmann, T., Mänd, K., Bui, T.H., Romashkin, A.E., Rychanchik, D.V., Prave, A.R., 2018. Multiple sulphur isotope records tracking basinal and global processes in the 1.98 Ga Zaonega Formation, NW Russia. *Chem. Geol.* 499, 151–164. <https://doi.org/10.1016/j.chemgeo.2018.09.025>

- Papineau, D., 2010. Global biogeochemical changes at both ends of the Proterozoic: Insights from phosphorites. *Astrobiology* 10, 165–181. <https://doi.org/10.1089/ast.2009.0360>
- Partin, C.A., Bekker, A., Planavsky, N.J., Scott, C.T., Gill, B.C., Li, C., Podkovyrov, V., Maslov, A., Konhauser, K.O., Lalonde, S.V., Love, G.D., Poulton, S.W., Lyons, T.W., 2013. Large-scale fluctuations in Precambrian atmospheric and oceanic oxygen levels from the record of U in shales. *Earth Planet. Sci. Lett.* 369–370, 284–293. <https://doi.org/10.1016/j.epsl.2013.03.031>
- Pavlov, A.A., Kasting, J.F., 2002. Mass-independent fractionation of sulfur isotopes in Archean sediments: strong evidence for an anoxic Archean atmosphere. *Astrobiology* 2, 27–41. <https://doi.org/10.1089/153110702753621321>
- Planavsky, N.J., Bekker, A., Hofmann, A., Owens, J.D., Lyons, T.W., 2012. Sulfur record of rising and falling marine oxygen and sulfate levels during the Lomagundi event. *Proc. Natl. Acad. Sci.* 109, 18300–18305. <https://doi.org/10.1073/pnas.1120387109>
- Planavsky, N.J., Reinhard, C.T., Wang, X., Thomson, D., McGoldrick, P., Rainbird, R.H., Johnson, T., Fischer, W.W., Lyons, T.W., 2014. Earth history. Low mid-Proterozoic atmospheric oxygen levels and the delayed rise of animals. *Science* 346, 635–638. <https://doi.org/10.1126/science.1258410>
- Planavsky, N.J., Slack, J.F., Cannon, W.F., O’Connell, B., Isson, T.T., Asael, D., Jackson, J.C., Hardisty, D.S., Lyons, T.W., Bekker, A., 2018. Evidence for episodic oxygenation in a weakly redox-buffered deep mid-Proterozoic ocean. *Chem. Geol.* 483, 581–594. <https://doi.org/10.1016/j.chemgeo.2018.03.028>
- Préat, A., Bouton, P., Thiéblemont, D., Prian, J.-P., Ndounze, S.S., Delpomdor, F., 2011. Paleoproterozoic high $\delta^{13}\text{C}$ dolomites from the Lastoursville and Franceville basins (SE Gabon): Stratigraphic and syndimentary subsidence implications. *Precambrian Res.* 189, 212–228. <https://doi.org/10.1016/j.precamres.2011.05.013>
- Priyatkina, N., Khudoley, A.K., Ustinov, V.N., Kullerud, K., 2014. 1.92Ga kimberlitic rocks from Kimozero, NW Russia: Their geochemistry, tectonic setting and unusual field occurrence. *Precambrian Res.* 249, 162–179. <https://doi.org/10.1016/j.precamres.2014.05.009>
- Puchtel, I.S., Brüggemann, G.E., Hofmann, A.W., 1999. Precise Re–Os mineral isochron and Pb–Nd–Os isotope systematics of a mafic–ultramafic sill in the 2.0 Ga Onega plateau (Baltic Shield). *Earth Planet. Sci. Lett.* 170, 447–461. [https://doi.org/10.1016/S0012-821X\(99\)00118-1](https://doi.org/10.1016/S0012-821X(99)00118-1)
- Qu, Y., Črne, A.E., Lepland, A., van Zuilen, M.A., 2012. Methanotrophy in a Paleoproterozoic oil field ecosystem, Zaonega Formation, Karelia, Russia. *Geobiology* 10, 467–478. <https://doi.org/10.1111/gbi.12007>
- Qu, Y., Lepland, A., van Zuilen, M.A., Whitehouse, M., Črne, A.E., Fallick, A.E., 2018. Sample-scale carbon isotopic variability and diverse biomass in the Paleoproterozoic Zaonega Formation, Russia. *Precambrian Res.* 315, 222–231. <https://doi.org/10.1016/j.precamres.2018.07.008>
- Rameil, N., 2008. Early diagenetic dolomitization and dedolomitization of Late Jurassic and earliest Cretaceous platform carbonates: A case study from the Jura Mountains (NW Switzerland, E France). *Sediment. Geol.* 212, 70–85. <https://doi.org/10.1016/j.sedgeo.2008.10.004>
- Rasmussen, B., Buick, R., 1999. Redox state of the Archean atmosphere: Evidence from detrital heavy minerals in ca. 3250–2750 Ma sandstones from the Pilbara Craton, Australia. *Geology* 27, 115–118. [https://doi.org/10.1130/0091-7613\(1999\)027<0115:RSOTAA>2.3.CO;2](https://doi.org/10.1130/0091-7613(1999)027<0115:RSOTAA>2.3.CO;2)

- Romanek, C.S., Grossman, E.L., Morse, J.W., 1992. Carbon isotopic fractionation in synthetic aragonite and calcite: Effects of temperature and precipitation rate. *Geochim. Cosmochim. Acta* 56, 419–430.
[https://doi.org/10.1016/0016-7037\(92\)90142-6](https://doi.org/10.1016/0016-7037(92)90142-6)
- Rosenbaum, J., Sheppard, S.M.F., 1986. An isotopic study of siderites, dolomites and ankerites at high temperatures. *Geochim. Cosmochim. Acta* 50, 1147–1150.
[https://doi.org/10.1016/0016-7037\(86\)90396-0](https://doi.org/10.1016/0016-7037(86)90396-0)
- Rye, R., Holland, H.D., 1998. Paleosols and the evolution of atmospheric oxygen; a critical review. *Am. J. Sci.* 298, 621–672. <https://doi.org/10.2475/ajs.298.8.621>
- Salminen, P.E., Karhu, J.A., Melezhik, V.A., 2013. Kolosjoki Sedimentary Formation: A record in the aftermath of the Paleoproterozoic global positive $\delta^{13}\text{C}$ excursion in sedimentary carbonates. *Chem. Geol.*, 362, 165–180.
<https://doi.org/10.1016/j.chemgeo.2013.10.018>
- Sapart, C.J., Monteil, G., Prokopiou, M., van de Wal, R.S.W., Kaplan, J.O., Sperlich, P., Krumhardt, K.M., van der Veen, C., Houweling, S., Krol, M.C., Blunier, T., Sowers, T., Martinerie, P., Witrant, E., Dahl-Jensen, D., Röckmann, T., 2012. Natural and anthropogenic variations in methane sources during the past two millennia. *Nature* 490, 85–88. <https://doi.org/10.1038/nature11461>
- Schidlowski, M., Eichmann, R., Junge, C.E., 1976. Carbon isotope geochemistry of the Precambrian Lomagundi carbonate province, Rhodesia. *Geochim. Cosmochim. Acta* 40, 449–455. [https://doi.org/10.1016/0016-7037\(76\)90010-7](https://doi.org/10.1016/0016-7037(76)90010-7)
- Schidlowski, M., Hayes, J.H., Kaplan, I.D., 1983. Isotopic inferences of ancient biochemistries – Carbon, sulfur, hydrogen, and nitrogen. In Schopf, J.W. (Ed), *Earth's Earliest Biosphere, its origin and evolution*, pp. 149–186. Princeton University Press, New Jersey
- Schidlowski, M., 2001. Carbon isotopes as biogeochemical recorders of life over 3.8 Ga of Earth history: evolution of a concept. *Precambrian Res.* 106, 117–134.
[https://doi.org/10.1016/S0301-9268\(00\)00128-5](https://doi.org/10.1016/S0301-9268(00)00128-5)
- Schieber, J., 1988. Redistribution of rare-earth elements during diagenesis of carbonate rocks from the Mid-Proterozoic Newland Formation, Montana, U.S.A. *Chem. Geol.* 69, 111–126. [https://doi.org/10.1016/0009-2541\(88\)90163-5](https://doi.org/10.1016/0009-2541(88)90163-5)
- Schier, K., Bau, M., Münker, C., Beukes, N., Viehmann, S., 2018. Trace element and Nd isotope composition of shallow seawater prior to the Great Oxidation Event: Evidence from stromatolitic bioherms in the Paleoproterozoic Rooinekke and Nelani Formations, South Africa. *Precambrian Res.* 315, 92–102.
<https://doi.org/10.1016/j.precamres.2018.07.014>
- Schoell, M., 1988. Multiple origins of methane in the Earth. *Chem. Geol., Origins of Methane in the Earth* 71, 1–10. [https://doi.org/10.1016/0009-2541\(88\)90101-5](https://doi.org/10.1016/0009-2541(88)90101-5)
- Schoenherr, J., Reuning, L., Hallenberger, M., Lüders, V., Lemmens, L., Biehl, B.C., Lewin, A., Leupold, M., Wimmers, K., Strohmenger, C.J., 2018. Dedolomitization: review and case study of uncommon mesogenetic formation conditions. *Earth-Sci. Rev.* 185, 780–805. <https://doi.org/10.1016/j.earscirev.2018.07.005>
- Scott, C., Wing, B.A., Bekker, A., Planavsky, N.J., Medvedev, P., Bates, S.M., Yun, M., Lyons, T.W., 2014. Pyrite multiple-sulfur isotope evidence for rapid expansion and contraction of the early Paleoproterozoic seawater sulfate reservoir. *Earth Planet. Sci. Lett.* 389, 95–104. <https://doi.org/10.1016/j.epsl.2013.12.010>
- Sharp, Z., 2007. *Principles of stable isotope geochemistry*, 2nd ed. Pearson/Prentice Hall.
- Sheen, A.I., Kendall, B., Reinhard, C.T., Creaser, R.A., Lyons, T.W., Bekker, A., Poulton, S.W., Anbar, A.D., 2018. A model for the oceanic mass balance of rhenium

- and implications for the extent of Proterozoic ocean anoxia. *Geochim. Cosmochim. Acta* 227, 75–95. <https://doi.org/10.1016/j.gca.2018.01.036>
- Shields, G., Stille, P., 2001. Diagenetic constraints on the use of cerium anomalies as palaeoseawater redox proxies: an isotopic and REE study of Cambrian phosphorites. *Chem. Geol., Response of the Oceanic / Atmospheric Systems to Past Global Changes* 175, 29–48. [https://doi.org/10.1016/S0009-2541\(00\)00362-4](https://doi.org/10.1016/S0009-2541(00)00362-4)
- Sholkovitz, E.R., Landing, W.M., Lewis, B.L., 1994. Ocean particle chemistry: The fractionation of rare earth elements between suspended particles and seawater. *Geochim. Cosmochim. Acta* 58, 1567–1579. [https://doi.org/10.1016/0016-7037\(94\)90559-2](https://doi.org/10.1016/0016-7037(94)90559-2)
- Simoneit, B.R.T., Lonsdale, P.F., Edmond, J.M., Shanks, W.C., 1990. Deep-water hydrocarbon seeps in Guaymas Basin, Gulf of California. *Appl. Geochem., Organic Matter in Hydrothermal Systems—Maturation, Migration and Biogeochemistry* 5, 41–49. [https://doi.org/10.1016/0883-2927\(90\)90034-3](https://doi.org/10.1016/0883-2927(90)90034-3)
- Soares, G.G., Van Kranendonk, M.J., Belousova, E., Thomson, S., 2019. Phosphogenesis in the immediate aftermath of the Great Oxidation Event: Evidence from the Turee Creek Group, Western Australia. *Precambrian Res.* 320, 193–212. <https://doi.org/10.1016/j.precamres.2018.10.017>
- Stepanova, A.V., Samsonov, A.V., Larionov, A.N., 2014. The final episode of middle Proterozoic magmatism in the Onega structure: data on trans-Onega dolerites. *Proc. Karelian Res. Cent. Russ. Acad. Sci.* 3–16, (in Russian).
- Stoessell, R.K., Klimentidis, R.E., Prezbindowski, D.R., 1987. Dedolomitization in Na Ca Cl brines from 100° to 200°C at 300 bars. *Geochim. Cosmochim. Acta* 51, 847–855. [https://doi.org/10.1016/0016-7037\(87\)90098-6](https://doi.org/10.1016/0016-7037(87)90098-6)
- Strauss, H., Melezhik, V.A., Lepland, A., Fallick, A.E., Hanski, E.J., Filippov, M.M., Deines, Y.E., Illing, C.J., Črne, A.E., Brasier, A.T., 2013. 7.6 Enhanced Accumulation of Organic Matter: The Shunga Event, in: Melezhik, V.A., Prave, A.R., Hanski, E.J., Fallick, A.E., Lepland, A., Kump, L.R., Strauss, H. (Eds.), *Reading the Archive of Earth's Oxygenation: Volume 3: Global Events and the Fennoscandian Arctic Russia – Drilling Early Earth Project*. Springer, 1195–1273. https://doi.org/10.1007/978-3-642-29670-3_6
- Svensen, H., Planke, S., Jamtveit, B., Pedersen, T., 2003. Seep carbonate formation controlled by hydrothermal vent complexes: a case study from the Vøring Basin, the Norwegian Sea. *Geo-Mar. Lett.* 23, 351–358. <https://doi.org/10.1007/s00367-003-0141-2>
- Swart, P.K., 2015. The geochemistry of carbonate diagenesis: The past, present and future. *Sedimentology* 62, 1233–1304. <https://doi.org/10.1111/sed.12205>
- Taylor, S.R., McLennan, S.M., 1985. *The Continental Crust, Its Composition and Evolution*. Blackwell Scientific Publications, Oxford, UK.
- Tostevin, R., Shields, G.A., Tarbuck, G.M., He, T., Clarkson, M.O., Wood, R.A., 2016. Effective use of cerium anomalies as a redox proxy in carbonate-dominated marine settings. *Chem. Geol.* 438, 146–162. <https://doi.org/10.1016/j.chemgeo.2016.06.027>
- Valley, J.W., O'Neil, J.R., 1984. Fluid heterogeneity during granulite facies metamorphism in the Adirondacks: stable isotope evidence. *Contrib. Mineral. Petrol.* 85, 158–173. <https://doi.org/10.1007/BF00371706>
- Valley, J.W., 1986. Stable isotope geochemistry of metamorphic rocks. *Rev. Mineral. Geochem.* 16, 445–489.

- Vandeginste, V., John, C.M., 2012. Influence of climate and dolomite composition on dedolomitization: insights from a multi-proxy study in the central Oman Mountains. *J. Sediment. Res.* 82, 177–195. <https://doi.org/10.2110/jsr.2012.19>
- Veizer, J., 1983. Trace elements and isotopes in sedimentary carbonates. *Rev. Mineral. Geochem.* 11, 265–299.
- Viehmann, S., Bau, M., Smith, A.J.B., Beukes, N.J., Dantas, E.L., Bühn, B., 2015. The reliability of ~2.9 Ga old Witwatersrand banded iron formations (South Africa) as archives for Mesoarchean seawater: Evidence from REE and Nd isotope systematics. *J. Afr. Earth Sci.* 111, 322–334. <https://doi.org/10.1016/j.jafrearsci.2015.08.013>
- Villa, I.M., De Bièvre, P., Holden, N.E., Renne, P.R., 2015. IUPAC-IUGS recommendation on the half life of ⁸⁷Rb. *Geochim. Cosmochim. Acta* 164, 382–385. <https://doi.org/10.1016/j.gca.2015.05.025>
- Wang, W., Bolhar, R., Zhou, M.-F., Zhao, X.-F., 2018. Enhanced terrestrial input into Paleoproterozoic to Mesoproterozoic carbonates in the southwestern South China Block during the fragmentation of the Columbia supercontinent. *Precambrian Res.* 313, 1–17. <https://doi.org/10.1016/j.precamres.2018.05.001>
- Webb, G.E., Kamber, B.S., 2000. Rare earth elements in Holocene reefal microbialites: a new shallow seawater proxy. *Geochim. Cosmochim. Acta* 64, 1557–1565. [https://doi.org/10.1016/S0016-7037\(99\)00400-7](https://doi.org/10.1016/S0016-7037(99)00400-7)
- Webb, G.E., Nothdurft, L.D., Kamber, B.S., Klopogge, J.T., Zhao, J.-X., 2009. Rare earth element geochemistry of scleractinian coral skeleton during meteoric diagenesis: a sequence through neomorphism of aragonite to calcite. *Sedimentology* 56, 1433–1463. <https://doi.org/10.1111/j.1365-3091.2008.01041.x>
- Weber, F., Gauthier-Lafaye, F., 2013. No proof from carbon isotopes in the Francevillian (Gabon) and Omega (Fennoscandian shield) basins of a global oxidation event at 1980–2090 Ma following the Great Oxidation Event (GOE). *Comptes Rendus Geosci.* 345, 28–35. <https://doi.org/10.1016/j.crte.2012.12.003>
- Whiticar, M.J., 1999. Carbon and hydrogen isotope systematics of bacterial formation and oxidation of methane. *Chem. Geol.* 161, 291–314. [https://doi.org/10.1016/S0009-2541\(99\)00092-3](https://doi.org/10.1016/S0009-2541(99)00092-3)
- Woo, K.S., Moore, C.H., 1996. Burial dolomitization and dedolomitization of the late Cambrian Wagok Formation, Yeongweol, Korea. *Carbonates Evaporites* 11, 104–112.
- Zhao, M.-Y., Zheng, Y.-F., 2017. A geochemical framework for retrieving the linked depositional and diagenetic histories of marine carbonates. *Earth Planet. Sci. Lett.* 460, 213–221. <https://doi.org/10.1016/j.epsl.2016.11.033>
- Zheng, Y.-F., Hoefs, J., 1993. Carbon and oxygen isotopic covariations in hydrothermal calcites. *Miner. Deposita* 28, 79–89. <https://doi.org/10.1007/BF00196332>
- Zhong, S., Mucci, A., 1995. Partitioning of rare earth elements (REEs) between calcite and seawater solutions at 25°C and 1 atm, and high dissolved REE concentrations. *Geochim. Cosmochim. Acta* 59, 443–453. [https://doi.org/10.1016/0016-7037\(94\)00381-U](https://doi.org/10.1016/0016-7037(94)00381-U)

SUMMARY IN ESTONIAN

Süsiniku isotoopkoostis ja haruldaste muldmetallide kasutatavus paleokeskonna indikaatoritena Paleoproterosoikumi setetes pärast Lomagundi-Jatuli Isotoopsündmust

Vaba hapnik ilmus Maa atmosfääri esmakordselt Paleoproterosoikumis, ligikaudu 2,4 miljardit aastat tagasi. Seda sündmust on nimetatud Suureks Hapniku Sündmuseks (Great Oxygenation Event - GOE) ja see tõi endaga kaasa põhimõttelised ümberkorraldused Maa (bio-)geokeemilistes aineringetes. Hapnikurikka atmosfääri tõttu algas mandritel intensiivse oksüdatiivne murenemine. Selle tulemusena kasvas oluliselt erinevate toitainete sissekanne meredesse ja ookeanidesse, mis omakorda tõi kaasa hüppelise primaarproduktiooni kasvu. GOE järel (osaliselt ajaliselt kattuvana) toimus teadaoleva Maa ajaloo suurima amplituudiga süsinikuringe häiring, mis väljendub mereliste karbonaatide stabiilsete süsinikuisotoopide anomaalses koostises ning mida tuntakse Lomagundi-Jatuli Isotoopsündmusena (Lomagundi-Jatuli Event – LJE). Ajavahemikku 2,22 kuni 2,06 Ga dateeritud LJE ajal moodustusid ebaharilikult raske süsiniku isotoopkoostisega karbonaatsed setted, mille $\delta^{13}\text{C}$ väärtused olid keskmiselt 10-15‰ raskemad, võrreldes kvaasistabiilse globaalse süsinikuringe korral moodustuvate mereliste setetega, mille $\delta^{13}\text{C}$ koostis on püsivalt ligikaudu 0‰. Lähtudes süsinikuringe üldisest mass-tasakaalust, põhjustab merelistes karbonaatides raske isotoopkoostise tekkimist samaaegne ulatuslik orgaanilise aine moodustumine ja mattumine, mis viib süsinikuringest välja isotoopselt ^{13}C suhtes vaesustunud orgaanilise ainese. Vastukaaluks tähendab orgaanilise ainese mattumine (st eemaldamine süsinikuringest) omakorda vaba hapniku jäämist atmosfääri, ning seetõttu arvatakse, et GOE ja LJE on omavahel tihedalt ja põhjuslikult seotud. Üldiselt aktsepteeritud arvamuse kohaselt ulatus GOE ajal hapniku sisaldus kuni 50%-ni tänapäevase tasemest ning kukkus pärast LJE lõppu üsna kiiresti ainult 0.1%-ni tänapäevase atmosfääri hapnikutasemest. Paradoksaalselt ei ole siiani leitud LJE-vanuselistest settekivimitest laiaulatuslikke orgaanilise ainesega rikastunud setendeid, mis viitaks LJE-ga samaaegsele suurenenud süsiniku mattumisele. Küll aga järgneb LJE-le nn. Šunga Sündmus, mille jooksul tekkisid erinevates maailma settebasseinides esmakordselt Maa ajaloos väga kõrge orgaanilise ainese sisaldusega settekivimid. Šunga Sündmuse tüüpnäiteks võib pidada Zaonega kihistut Onega basseinins Loode-Venemaal, kus mudakivimite keskmine orgaanilise ainese sisaldus on u. 25%.

Zaonega kihistu on peale kõrge orgaanilise ainese sisalduse märkimisväärne ka selle poolest, et selles esinevates karbonaatkivimites on jälgitav tüüpilise LJE signaali kadumine ja karbonaatsete settekivimite üleminek orgaanikarikasteks mudakivideks, mis iseloomustavad Šunga Sündmust. Sellest tulenevalt on Zaonega kihistu kivimite geokeemilised uuringud olnud kesksel kohal nii LJE kui sellele järgnenud ajaperioodide keskkonnatingimuste tõlgendamisel. Paraku on Zaonega kihistu kivimite geokeemilised uuringute tõlgendused üksteisele vasturääkivad.

Osad neist väidavad, et pärast LJE-st toimus atmosfääris hapnikutaseme kollaps, teised aga viitavad kõrgeenenud hapnikutaseme säilimisele. Käesolev doktoritöö keskendub Zaonega kihistu karbonaatidele, püüdes välja selgitada, kuidas muutus mereline paleokeskkond LJE-le vahetult järgnenud ajaperioodil. Uuring kasutab selleks karbonaatsete setete süsiniku isotoopkoostise ning haruldaste muldmetallide (rare earth elements and yttrium – REY) käitumismustreid. Globaalsed karbonaatse süsiniku isotoopkoostise ekskursioonid kannavad teavet üldises süsinikuringes sisalduva mattunud orgaanilise ainese hulga, mis omakorda on otseselt seotud vabanenud vaba hapniku hulga. Haruldasi muldmetalle on võimalik kasutada erinevate settekeskkondade identifitseerimiseks. Kui enamik haruldastest muldmetallidest on kolmevalentsed, siis Ce ja Eu on muutuva valentsiga, käitudes seetõttu redutseerivates ja oksüdeerivates keskkondades erinevalt. Ce sisaldus mereveest moodustunud mineraalides (nt. dolomiit ja apatiit) ning selle võrdlus teiste REY-dega võimaldavad hinnata redokstingimusi atmosfäär-ookean süsteemis. Hindamaks, kas Zaonega kihistus kirjeldatavad geokeemilised mustrid on tüüpilised ainult Onega basseini või esindavad need laiemat seaduspära, uuriti antud töös ka Pilgijärvi settekihitud Petšenga basseinis. Zaonega kihistust ligikaudu 60 miljonit aastat noorem Pilgijärvi settekihistu on litoloogiliselt sarnane Zaonega kihistule ning annab hea võimaluse hinnata, kas ja kui palju erinesid atmosfääri-okeani LJE-järgsed redokstingimused LJE-eelsetest.

Doktoritöö tulemused näitasid, kui oluline on eristada sekundaarselt mõjutatud intervalle, et setteläbilõigete algset keskkonnasignaali usaldusväärselt tuvastada. Zaonega kihistu karbonaate iseloomustab dolomiidikihtide äärealade dedolomiti-seerumine, mis on valdavalt kustutanud karbonaatkivimite primaarsed geokeemilised tunnused. Dolomiidikihtide siseosad on aga säilitanud info kunagiste settetingimuste kohta. Zaonega kihistu ülemise osa kõige paremini säilinud karbonaatides tuvastati stratigraafiliselt kasvav $\delta^{13}\text{C}$ väärtuste trend $-8,5\%$ kuni $+0,8\%$. Lisaks näidati, et kerge süsiniku isotoopkoostisega metaani oksüdeerimisel tekkinud lahustunud anorgaanilise süsiniku reservuaar mõjutas Zaonega kihistu autigeensete karbonaatide moodustumist. Zaonega kihistu ülemist osa avavates OnZapi puursüdamikes tuvastati anaeroobselt oksüdeeritud metaani (AOM) arvelt tekkinud autigeense karbonaadi kihid, mille $\delta^{13}\text{C}$ väärtused on -25% ja -20% vahel. Haruldaste muldmetallide käitumine Zaonega kihistu setendites kinnitab merelist signaali OnZapi läbilõike keskmises osas (Unit B). Seda iseloomustab mereveele omane kerge REE-de (LREE) vaesestumine võrreldes raskete REE-ga (HREE), positiivsed La_{SN} ja Gd_{SN} anomaaliad ning superkondriitne Y/Ho suhe. Zaonega kihistule on lisaks iseloomulik positiivne Eu_{SN} anomaalia, mis viitab hüdrotërmaalset päritolu REY-de suurele osatähtsusele REY-de allikana. See viitab omakorda aga sellele, et Onega basseini ühendus avaookeaniga pidi olema piiratud, kuna vastasel juhul ei säiliks lausaline positiivne Eu_{SN} anomaalia.

Onega basseini Zaonega kihistu parima säilivusega karbonaatseid setteid iseloomustab negatiivne Ce_{SN} anomaalia, mis viitab, et atmosfäär-ookeani süsteemis pidi olema piisavalt vaba hapnikku, et Ce saaks oksüdeeruda ja teistest REY

elementidest geokeemiliselt eralduda. Samasugune Ce_{SN} anomaalia esineb Petšenga basseini Pilgujärvi settekihistu apatiidis, mis samuti viitab hapnikulisele settekeskonnale. Samas tuvastati, et negatiivne Ce_{SN} anomaalia esineb küll Pilgujärvi jämedateralises liivakivi ümbersettinud apatiidi terades, aga puudub mudakivimeid tsementeerivast apatiidis. Tõenäoliselt moodustusid mudakivimid basseini sügavama osa taandavas keskkonnas. Ümbersettinud apatiidi terad pärinevad aga hoopis basseini madalaveelisest osast, kus esines hapnikurikkam keskkond. Samas võis hapnikulise murenemise tingimustes Ce teistest REY-st eralduda juba jõgede sissevoolus.

Käesoleva doktoritöö tulemuste põhjal saab järeldada, et Zaonega kihistu on oluliselt mõjutatud lokaalsetest, Onega basseini iseloomulikest geokeemilistest-geoloogilistest protsessidest, millega tuleb arvestada, kui kasutada Zaonega kihistu geokeemilisi signaale globaalsete sündmuste kirjeldamisel. Kuigi mitmetes teistes LJE-aegsetes ja järgnevates läbilõigetes on kirjeldatud negatiivseid karbonaatse süsiniku ekskursionsioone, siis ükski neist pole nii suure amplituudiga kui Zaonega kihistus. Zaonega kihistu negatiivne süsiniku isotoopide ekskursionsioon on ennekõike seotud lokaalse metanotroofse süsiniku mõjuga Onega basseinis ning seda ei saa otseselt seostada globaalsete keskkonnatingimustega. Samas oli basseini perioodiline ühendus avaookeaniga piisav tüüpilise tasakaalulise avamere karbonaatide iseloomuliku $\delta^{13}C$ isotoopkoostise kujunemiseks, mida kinnitab ka dolomiitide iseloomulik merevee REY_{SN} muster. Onega basseini Zaonega kihistu karbonaatides ning Petšenga basseini Pilgujärvi settekihistu apatiidis esinev negatiivne Ce_{SN} anomaalia viitab püsivalt kõrgendatud, aga samas ka muutlikule hapnikutasemele pärast LJE-e hääbumist. Ekskursionsioonid karbonaatse süsiniku isotoopkoostises ning negatiivne, aga varieeruv Ce_{SN} anomaalia amplituud uuritud basseini setendites viitab süsinikuringe ebastabiilsusele ja muutlikele hapnikutasemetele LJE-le järgnenud perioodil. Toetudes teadaolevatele tõenditele, on ennatlik järeldada, et LJE lõpule järgnes kohe järsk ühesuunaline vaba hapnikutaseme langus atmosfäär-ookean süsteemis.

ACKNOWLEDGEMENTS

I am grateful to my supervisors Kalle Kirsimäe and Aivo Lepland whose help and guidance throughout my PhD studies are greatly appreciated. I would like to thank my co-authors for all their contribution as well as all my colleagues from the Department of Geology at the University of Tartu and Mari Aigro for language correction. Financial support from the Estonian Research Council (PUT696 and PRG447), the Doctoral School of Earth Science and Ecology as well as the Archimedes Foundation are highly appreciated. Last but not least I would like to thank my friends and family for keeping me motivated throughout my PhD studies.

PUBLICATIONS

CURRICULUM VITAE

Name: Timmu Kreitsmann
Date of birth: 25.08.1989
Address: Department of Geology, University of Tartu,
Ravila 14A, 50411 Tartu, Estonia
Contact: Tel. +372 55587681
E-mail: timmu.kreitsmann@ut.ee

Education

2013–... University of Tartu, Department of Geology, PhD student in geology
2011–2013 University of Tartu, MSc in geology (*cum laude*)
2008–2011 University of Tartu, BSc in geology
2005–2008 Kuressaare Gümnaasium

Professional employment

2018–... Specialist in Geology, University of Tartu, Department of Geology
2015 Laboratory Assistant, University of Tartu, Department of Geology
2014–2015 Specialist in Geology, University of Tartu, Department of Geology

Field of research:

Petrology, mineralogy, geochemistry, carbonate geochemistry

Publications

1. Joosu, L.; Lepland, A.; **Kreitsmann, T.**; Üpraus, K.; Roberts, N.M.W.; Paiste, P.; Martin, A.P.; Kirsimäe, K. (2016). Petrography and the REE-composition of apatite in the Paleoproterozoic Pilgijärvi Sedimentary Formation, Pechenga Greenstone Belt, Russia. *Geochimica et Cosmochimica Acta*, 186, 135–153.
2. Plado, J.; Hietala, S.; **Kreitsmann, T.**; Lerssi, J.; Nenonen, J.; Pesonen, L.J. (2018). Summanen, a new meteorite impact structure in Central Finland. *Meteoritics and Planetary Science*, 53 (11), 2413–2426.
3. Blättler, C.L.; Claire, M.W.; Prave, A.R.; Kirsimäe, K.; Higgins, J.A.; Medvedev, P.V.; Romashkin, A.E.; Rychanchik, D.V.; Zerkle, A.L.; Paiste, K., **Kreitsmann, T.**; Millar, I.L.; Hayles, J.A.; Bao, H.; Turchyn, A.V.; Warke, M.R.; Lepland, A. (2018). Two-billion-year-old evaporites capture Earth's great oxidation. *Science*, 360 (6386), 320–323.
4. Paiste, K.; Lepland, A.; Zerkle, A.L.; Kirsimäe, K.; Izon, G.; Patel, N.K.; McLean, F.; **Kreitsmann, T.**; Mänd, K.; Bui, T.H.; Romashkin, A.E.; Rychanchik, D.V.; Prave, A.R.; (2018). Multiple sulphur isotope records tracking basinal and global processes in the 1.98 Ga Zaonega Formation, NW Russia. *Chemical Geology*, 499, 151–164.

5. Prave, A.R.; Meng, F.; Lepland, A.; Kirsmäe, K.; **Kreitsmann, T.**; Jiang, C.Z. (2018). A refined late-Cryogenian – Ediacaran earth history of South China: Phosphorous-rich marbles of the Dabie and Sulu orogens. *Precambrian Research*, 305, 166–176.
6. **Kreitsmann, T.**; Külaviir, M.; Lepland, A.; Paiste, K.; Paiste, P.; Prave, A.R.; Sepp, H.; Romashkin, A.E.; Rychanchik, D.V.; Kirsimäe, K. (2019). Hydrothermal dedolomitisation of carbonate rocks of the Paleoproterozoic Zaonega Formation, NW Russia – Implications for the preservation of primary C isotope signals. *Chemical Geology*, 512, 43–57.
7. **Kreitsmann, T.**; Lepland, A.; Bau, M.; Prave, A.R.; Paiste, K.; Mänd, K.; Sepp, H.; Martma, T.; Romashkin, A.E.; Kirsimäe, K. Oxygenated conditions in the aftermath of the Lomagundi-Jatuli Event: carbon isotope and rare earth element signatures of the Paleoproterozoic Zaonega Formation, Russia. Manuscript submitted to *Precambrian Research*.
8. Mänd, K., Robbins, L. J., Thoby, M., Paiste, K., **Kreitsmann, T.**, Lalonde, S. V., Kirsimäe, K., Lepland, A., Konhauser, K. O. Extreme trace metal enrichments in the Zaonega Formation indicate a post-Lomagundi O₂ overshoot. Manuscript submitted to *Nature Geoscience*.

ELULOOKIRJELDUS

Nimi: Timmu Kreitsmann
Sünniaeg: 25.08.1989
Address: Geoloogia osakond, Tartu Ülikool,
Ravila 14A, 50411 Tartu, Eesti
Kontakt: Tel. +372 55587681
E-post: timmu.kreitsmann@ut.ee

Haridus

2013–... Tartu Ülikool, Geoloogia osakond, doktorant geoloogia erialal
2011–2013 Tartu Ülikool, Geoloogia osakond, MSc geoloogias (*cum laude*)
2008–2011 Tartu Ülikool, Geoloogia osakond, BSc geoloogias
2005–2008 Kuressaare Gümnaasium

Teenistuskäik

2018–... Tartu Ülikool, Geoloogia osakond, geoloogia spetsialist
2015 Tartu Ülikool, Geoloogia osakond, laborant
2014–2015 Tartu Ülikool, Geoloogia osakond, geoloogia spetsialist

Teadustöö põhisuund:

Petroloogia, mineraloogia, geokeemia, karbonaatide geokeemia

Publikatsioonid

1. Joosu, L.; Lepland, A.; **Kreitsmann, T.**; Üpraus, K.; Roberts, N.M.W.; Paiste, P.; Martin, A.P.; Kirsimäe, K. (2016). Petrography and the REE-composition of apatite in the Paleoproterozoic Pilgijärvi Sedimentary Formation, Pechenga Greenstone Belt, Russia. *Geochimica et Cosmochimica Acta*, 186, 135–153.
2. Plado, J.; Hietala, S.; **Kreitsmann, T.**; Lerssi, J.; Nenonen, J.; Pesonen, L.J. (2018). Summanen, a new meteorite impact structure in Central Finland. *Meteoritics and Planetary Science*, 53 (11), 2413–2426.
3. Blättler, C.L.; Claire, M.W.; Prave, A.R.; Kirsimäe, K.; Higgins, J.A.; Medvedev, P.V.; Romashkin, A.E.; Rychanchik, D.V.; Zerkle, A.L.; Paiste, K., **Kreitsmann, T.**; Millar, I.L.; Hayles, J.A.; Bao, H.; Turchyn, A.V.; Warke, M.R.; Lepland, A. (2018). Two-billion-year-old evaporites capture Earth's great oxidation. *Science*, 360 (6386), 320–323.
4. Paiste, K.; Lepland, A.; Zerkle, A.L.; Kirsimäe, K.; Izon, G.; Patel, N.K.; McLean, F.; **Kreitsmann, T.**; Mänd, K.; Bui, T.H.; Romashkin, A.E.; Rychanchik, D.V.; Prave, A.R.; (2018). Multiple sulphur isotope records tracking basinal and global processes in the 1.98 Ga Zaonega Formation, NW Russia. *Chemical Geology*, 499, 151–164.
5. Prave, A.R.; Meng, F.; Lepland, A.; Kirsimäe, K.; **Kreitsmann, T.**; Jiang, C.Z. (2018). A refined late-Cryogenian – Ediacaran earth history of South China:

Phosphorous-rich marbles of the Dabie and Sulu orogens. *Precambrian Research*, 305, 166–176.

6. **Kreitsmann, T**; Külaviir, M; Lepland, A; Paiste, K; Paiste, P; Prave, A.R; Sepp, H; Romashkin, A.E; Rychanchik, D.V; Kirsimäe, K (2019). Hydrothermal dedolomitisation of carbonate rocks of the Paleoproterozoic Zaonega Formation, NW Russia – Implications for the preservation of primary C isotope signals. *Chemical Geology*, 512, 43–57.
7. **Kreitsmann, T**; Lepland, A; Bau, M.; Prave, A.R; Paiste, K; Mänd, K.; Sepp, H; Martma, T.; Romashkin, A.E; Kirsimäe, K. Oxygenated conditions in the aftermath of the Lomagundi-Jatuli Event: carbon isotope and rare earth element signatures of the Paleoproterozoic Zaonega Formation, Russia. Manuscript submitted to *Precambrian Research*.
8. Mänd, K., Robbins, L. J., Thoby, M., Paiste, K., **Kreitsmann, T**, Lalonde, S. V., Kirsimäe, K., Lepland, A., Konhauser, K. O. Extreme trace metal enrichments in the Zaonega Formation indicate a post-Lomagundi O₂ overshoot. Manuscript submitted to *Nature Geoscience*.

DISSERTATIONES GEOLOGICAE UNIVERSITATIS TARTUENSIS

1. **Пэп Мянник.** Конодонты в верхнеордовикских и нижнесилурийских отложениях Эстонии. Тарту, 1992, 355 с.
2. **Elvi Tavast.** Fennoskandia kilbi lõunanõlva ja sellega piirnevate alade alusrõhja reljeef. Tartu, 1992, 357 lk.
3. **Kaarel Orviku.** Characterisation and evolution of Estonian seashores. Tartu, 1992, 19 p.
4. **Анатолий Молодьков.** ЭПР-анализ скелетного вещества моллюсков в хроностратиграфических исследованиях позднего кайнозоя. Тарту, 1992, 33 с.
5. **Jaani Lutt.** Late- and postglacial deposits on the Estonian shelf. Tartu, 1993, 31 p.
6. **Reet Karukäpp.** Gotiglatsiaalne morfogenees Skandinaavia mandriliustiku kagusektoris. Tartu, 1997, 181 p.
7. **Argo Jõelet.** Geothermal studies of the Precambrian basement and Phanerozoic sedimentary cover in Estonia and Finland. Tartu, 1998, 125 p.
8. **Jüri Nemliher.** Mineralogy of Phanerozoic skeletal and sedimentary apatites: an XRD study. Tartu, 1999, 134 p.
9. **Kalle Kirsimäe.** Clay mineral diagenesis on the Lower Cambrian “Blue Clay” in the northern part of the Baltic Paleobasin. Tartu, 1999, 113 p.
10. **Jüri Plado.** Gravity and magnetic signatures of meteorite impact structures. Tartu, 2000, 87 p.
11. **Olev Vinn.** Morphogenesis and phylogenetic relationships of Clitambonitidines, Ordovician Brachiopods. Tartu, 2001, 127 p.
12. **Leho Ainsaar.** The middle Caradoc facies and faunal turnover in the late Ordovician Baltoscandian palaeobasin: sedimentological and carbon isotope aspects. Tartu, 2001, 109 p.
13. **Oive Tinn.** Early Ostracode evolution and Palaeoenvironmental application in the Ordovician of Baltoscandia. Tartu, 2002, 145 p.
14. **Maris Rattas.** Subglacial environments in the formation of drumlins — The case of the Saadjärve Drumlin Field, Estonia. Tartu, 2004, 117 p.
15. **Ene Kadastik.** Upper-Pleistocene stratigraphy and deglaciation history in northwestern Estonia. Tartu, 2004, 129 p.
16. **Helje Pärnaste.** Early Ordovician trilobites of suborder Cheirurina in Estonia and NW Russia: systematics, evolution and distribution. Tartu, 2004, 138 p.
17. **Mari-Ann Mõtus.** Silurian (Llandovery-Wenlock) tabulate corals of Baltoscandia: taxonomy, palaeoecology, distribution. Tartu, 2005, 167 p.
18. **Alar Rosentau.** Development of proglacial lakes in Estonia. Tartu, 2006, 114 p.
19. **Evelin Verš.** Development of impact-induced hydrothermal system at Kärddla impact structure. Tartu, 2006, 96 p.

20. **Sigitas Radzevičius.** The genus *Pristiograptus* in wienlock of East Baltic and the Holy Cross Mountains. Tartu, 2007, 133 p.
21. **Andres Marandi.** Natural chemical composition of groundwater as a basis for groundwater management in the Cambrian-Vendian aquifer system in Estonia. Tartu, 2007, 116 p.
22. **Eve Niinemets.** Vegetation and land-use history of the Haanja Heights (SE-Estonia) during the holocene. Tartu, 2008, 146 p.
23. **Kalle-Mart Suuroja.** Geology and lithology of the early palaeozoic marine impact structures Kärddla and Neugrund (Estonia). Tartu, 2008, 234 p.
24. **Rutt Hints.** Early diagenesis of Ordovician and Silurian Bentonites in the Northern Baltic Palaeobasin. Tartu, 2009, 90 p.
25. **Peeter Somelar.** Illitization of K-bentonites in the Baltic Basin. Tartu, 2009, 118 p.
26. **Ulla Preeden.** Remagnetizations in sedimentary rocks of Estonia and shear and fault zone rocks of southern Finland. Tartu, 2009, 121 p.
27. **Kati Tänavsuu-Milkeviciene.** Transgressive to regressive turnaround in the Middle Devonian Baltic Basin. Tartu, 2009, 106 p.
28. **Valle Raidla.** Chemical and isotope evolution of groundwater in the Cambrian-Vendian aquifer system in Estonia. Tartu, 2010, 134 p.
29. **Kadri Sohar.** Quaternary ostracods from Estonia and their application in palaeoenvironmental reconstruction. Tartu, 2010, 140 p.
30. **Kristjan Urtson.** Stepwise melt transport and accumulation: analogue and numerical modelling approach. Tartu, 2011, 83 p.
31. **Marko Kohv.** Landslides in clayey soils of western Estonia. Tartu, 2011, 116 p.
32. **Nele Muttik.** Post-impact alteration of impactites: Ries crater, Germany. Tartu, 2011, 78 p.
33. **Annette Sedman.** Strength and self-cementing properties of oil shale retorting wastes. Tartu, 2013, 82 p.
34. **Arkady Tsyrunnikov.** Complex seismo-acoustic and lithological study of the Lateglacial and postglacial sediments northern Gulf of Riga, eastern branch of the central Baltic Sea. Tartu, 2013, 102 p.
35. **Marge Uppin.** Geological sources and hydrochemistry of fluoride and boron in Silurian-Ordovician aquifer system. Tartu, 2013, 86 p.
36. **Peeter Talviste.** Temporal changes in weak natural and artificial soils – influence on geotechnical characteristics. Tartu, 2014, 204 p.
37. **Katrin Lasberg.** Chronology of the Weichselian Glaciation in the south-eastern sector of the Scandinavian Ice Sheet. Tartu, 2014, 100 p.
38. **Sirle Liivamägi.** Neoproterozoic Baltic paleosol: geology and paleoenvironmental interpretation. Tartu, 2015, 94 p.
39. **Lauri Joosu.** Petrography and the rare earth element composition of apatite in 2 Ga Onega and Pechenga basins, Russia: the environmental settings for phosphogenesis. Tartu, 2015, 139 p.
40. **Liisa Lang.** Baculate shell structure in Early Palaeozoic linguliform brachiopods. Tartu, 2015, 114 p.

41. **Päärn Paiste**. Geopolymeric potential of the Estonian oil shale processing waste. Tartu, 2017, 125 p.
42. **Mikk Gaškov**. Stable isotope and fluid inclusion evidence of multistage fluidal activity in Baltic paleobasin: Silurian carbonate sequence in Kalana, Estonia. Tartu, 2017, 104 p.
43. **Viirika Mastik**. Silurian noncalcified macroscopic algal fossils from the Kalana *Lagerstätte*, Estonia. Tartu, 2018, 91 p.
44. **Kairi Põldsaar**. Soft-sediment deformation and gravity flow structures in the Lower Palaeozoic successions of the Baltic Basin. Tartu, 2019, 105 p.